CASSINI UVIS USER'S GUIDE

Laboratory for Atmospheric and Space Physics (LASP)
University of Colorado
1234 Innovation Drive
Boulder, CO 80301
303-492-6412

Revised December 18, 2017
Revised July 6, 2018

TABLE OF CONTENTS

Introduction
Larry Esposito

The Cassini Ultraviolet Imaging Spectrograph (UVIS) is a multi-faceted experiment on the Cassini orbiter. The instrument is described by Esposito et al. (2004). Instrument updates, news and publications may be found on the public web-site, http://lasp.colorado.edu/cassini/.

This guide provides information and examples for using UVIS data that is available in the Planetary Data System, with individual chapters written by members of the UVIS Science Team. Each of the chapters describes a different data type. Examples are shown. Because a number of different approaches have been successfully used by UVIS Team members, a number of alternate instructions are given in the different chapters. For example, the simplest approach to calibration is given in Chapter 3, and alternate approaches are given in Chapters 4, 9 and 10. Questions should be addressed to a member of the science team or to David Judd (303-492-8582, david.judd@lasp.colorado.edu). This guide was supported by a grant from NASA Headquarters.

We look forward to the larger scientific community's productive use of the UVIS data.

Larry W. Esposito
Cassini UVIS Principal Investigator

1. Cassini UVIS data on the PDS system

Feng Tian

On October 15, 1997, the Cassini-Huygens spacecraft was launched by NASA's Jet Propulsion Laboratory (JPL) from Kennedy Space Center in Florida. After a seven-year journey, it entered Saturn's orbit on July 1, 2004 Coordinated Universal Time (UTC), or June 30 at 8:36 p.m. MDT. The mission includes the Cassini orbiter and the Huygens probe, which was released from the Cassini orbiter and landed on the Titan moon to explore its surface and atmosphere. The instruments onboard have provided scientists with new and exciting data to help understand the mysterious Saturnian system. Besides the Huygens probe, Cassini's instrumentation consists of 12 instruments.
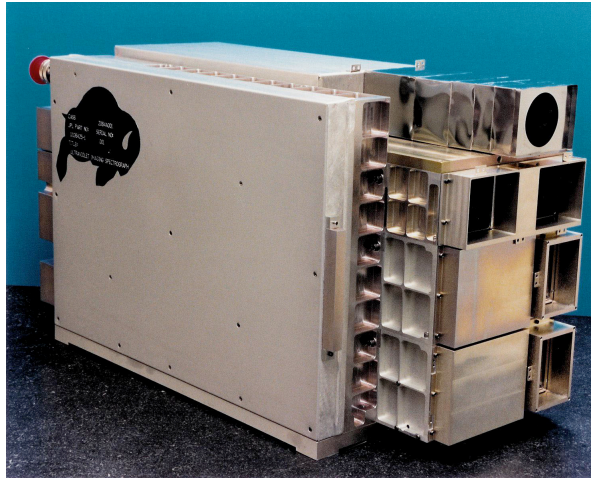
The Ultraviolet Imaging Spectrograph (UVIS) is one of the 12 instruments installed on board Cassini. It was built by the Laboratory for Atmospheric and Space Physics (LASP) located in the Research Park of the University of Colorado in Boulder. The UVIS is a set of telescopes used to measure ultraviolet light from the Saturn system's atmospheres, rings, and surfaces. The UVIS also observes the fluctuations of starlight and sunlight as the sun and stars move behind the rings and the atmospheres of Titan and Saturn. These observations are helpful to better understand the atmospheric composition and photochemistry of Saturn and Titan, determine the atmospheric concentrations of hydrogen and deuterium in these atmospheres, and provide information on the nature and history of Saturn's rings. UVIS data have also helped to understand the physical properties of the water plumes and the salty ocean inside Enceladus. A detailed description of UVIS can be found in the UVIS Science Team's paper published in Space Science Reviews (Esposito et al. 2004). The following is a brief description of the components of the UVIS.

The UVIS has two spectrographic channels: the extreme ultraviolet channel (EUV 56 to 118 nm) and the far ultraviolet channel (FUV 110 to 190 nm). The ultraviolet channels are built into weight-relieved aluminum cases, and each contains a reflecting telescope, a concave grating spectrometer, and an imaging, pulse-counting detector. Three slits are available: a high resolution slit (75 and 100 μm slit width for the FUV and EUV channel, respectively), a low resolution slit (150 and 200 μm slit width for the FUV and EUV respectively), and an occultation slit of 800 μm width, identical for both channels. In both the EUV and the FUV channels the detector is a CODACON (CODed Anode array CONverter), consisting of 1024 pixels in the spectral direction and 64 pixels in the spatial direction. The UVIS also includes a high-speed photometer channel (HSP), a hydrogen-deuterium absorption cell channel (HDAC), and an electronic and control subassembly.

The extreme ultraviolet channel (EUV) is used primarily for imaging spectroscopy and spectroscopic measurements of the structure and composition of the atmospheres of Titan and Saturn. The EUV channel consists of a telescope with a three-position slit changer, a baffle system, and a spectrograph with a CODACON microchannel plate detector and associated electronics. The telescope consists of an off-axis section of a parabolic mirror with a focal length of 100 mm, and a 20 x 20 mm aperture. A precision mechanism positions one of the three entrance slits at the focal plane of the telescope, each translating to a different spectral resolution. The spectrograph uses a toroidal grating that focuses the spectrum onto an imaging microchannel plate detector to achieve both high sensitivity and spatial resolution along the entrance slit. The microchannel plate detector electronics consist of a low-voltage power supply, a programmable high-voltage power supply, charge-sensitive amplifiers, and associated logic. The EUV channel also contains a solar occultation port to allow solar flux to enter the telescope through a small aperture when the sun is 20 degrees off-axis from the primary telescope.

The far ultraviolet channel (FUV) is used primarily for imaging spectroscopy and spectroscopic measurements of the structure and composition of the atmospheres of Titan and Saturn and of the rings and icy satellites. The FUV is similar to the EUV channel except for the grating ruling density, optical coatings, and detector details. The FUV electronics are similar to those for the EUV except for the addition of a high-voltage power supply for the ion pump.

The high-speed photometer channel (HSP), using a solar blind CsI photocathode, performs high signal-to-noise-ratio stellar occultation measurements of the structure and density of material in the rings, as well as the atmospheres. The HSP resides in its own module and measures light that is focused by its own parabolic mirror with a photomultiplier tube detector. The electronics consist of a pulse-amplifier-discriminator and a fixed-level high- voltage power supply.

The hydrogen-deuterium absorption cell channel (HDAC) is used to measure the relative abundance of D/H in the Saturn system from their Lyman-alpha emission by using a hydrogen cell, a deuterium cell, and a channel electron multiplier (CEM) detector to record photons not absorbed in the cells. The hydrogen and deuterium cells are resonance absorption cells filled with pure molecular hydrogen and deuterium, respectively. They are located between an objective lens and a detector. Both cells are made of stainless steel coated with teflon and are sealed at each end with MgF_2 windows. The electronics consist of a pulse-amplifier-discriminator, a fixed-level high-voltage power supply, and two filament current controllers.

The UVIS microprocessor electronics and control subassembly consists of input-output elements, power conditioning, science data and housekeeping data collection electronics, and microprocessor control elements.

The microprocessor on the UVIS operates the instrument, executes various operating modes for data handling and compression, and buffers the instrument's observation data for pickup by the Cassini Orbiter's Command and Data Subsystem (CDS). The Cassini spacecraft points the UVIS telescopes to the desired target (including stars, the Sun, atmospheric features, and the limbs of Saturn and its moons). The spacecraft attitude control allows for slews, steps, or drifts across the target. Generally, these spacecraft motions are executed by commands issued from the spacecraft CDS. Synchronization of the instrument activities with the spacecraft motion is achieved by having the CDS send trigger commands to the UVIS at the correct time. These trigger commands instruct the UVIS to execute actions that have been pre-loaded in the UVIS memory. The data from the observation are buffered for pickup by the CDS. Two pickup rates are allowed: 32 kbps (for occultations) and 5 kbps (for spectral imaging). UVIS team members generate command sequences for each observation, which are loaded in the UVIS memory using a set of tools known as the Uplink Product Generation System (UPGS). The sequence of internal commands is then submitted to the sequencing team at JPL via the UVIS SOPC (Science Operations and Planning Computer). Using the SOPC and the UVIS GSE (Ground Support Equipment), the UVIS team can also monitor the health of the instrument in near real-time. In addition, the SOPC is used to access the data played back by the spacecraft and stored in the JPL Telemetry Data Server (TDS).

Like all observations, the UVIS data contain noises from different sources and anomalies. The Cassini spacecraft is powered by 3 radioisotope thermoelectric generators (RTGs), which use heat from the natural decay of plutonium-238 to generate direct current electricity via thermocouples. The RTGs produce a constant background noise that needs to be subtracted from the UVIS observation. There are other backgrounds that may or may not contribute to the total raw counts; however the RTG background is internal to the spacecraft and must always be dealt with. More descriptions on the handling of RTG background can be found in Chapters 3, 4, 7, and 8. A small light leak allowed undispersed interplanetary H Lyman-α to reach the EUV detector for pixels <720, corresponding to wavelengths shorter than 920 Å. For observations prior to 2007, this creates a background referred to as the "mesa" by the UVIS team. Users of this pre-2007 data should be careful to remove the affected pixels. In 2007 the source of the light leak was identified and it was eliminated from subsequent observations by opening the solar occultation door. For wavelengths >~1150 Å (EUV pixel 971), another wavelength dependent background arises from internal instrument scattering of H Lyman-α. This contribution to the EUV signal is small below 1170 Å, and is estimated to be less than 7% of the total signal, based on comparisons with a modeled H_2 spectrum (Ajello et al., 2005). When all the noise sources are subtracted from the signal, the raw observation is ready for the flatfield calibration and the conversion from the raw counts to physical units. Users can find more information regarding backgrounds, the flatfield correction, and calibration in Chapters 3 and 11.

A population of anomalous pixels exist in the FUV detector (~15% of all detector elements), which are characterized by relatively low and possibly nonlinear responses. These pixels are often referred to as "evil". Although these anomalous pixels are distributed across the entire FUV detector, they often appear in groups along individual columns. Because of the poorly characterized response of these evil pixels, the UVIS team has decided to eliminate them from analysis. This is implemented by assigning an invalid sensitivity to the calibration matrix for these elements. Users can find how the "evil" pixels are identified and handled in Chapters 3 and 4. An alternate approach is to average over large enough areas of the detector to minimize the effects. This is described in 9.3.

The Cassini UVIS data are stored in the NASA PDS system. The detailed structure and components of the UVIS data in the PDS are described in Chapter 2. In the current chapter we provide step-by-step instructions on how to find and obtain the UVIS data from the PDS with the following 3 examples: 1) a 2005 observation of Saturn's aurora; 2) a 2004 observation of the reflected FUV spectrum from Phoebe; and 3) a 2005 Enceladus occultation observation.

Example 1: An observation of Saturn's aurora was carried out around 03:35 on day 172 of year 2005.

1) Go to the Cassini UVIS data website: http://pds-rings.seti.org/cassini/uvis/access.html

2) Find COUVIS_0011 in the table called "Temporal coverage of each volume", which contains the observations taken on day 172. And the available data are listed by the date the observations were carried out.

3) Open COUVIS_0011/DATA/D2005_172/ (the full URL address is http://pds-rings.seti.org/vol/COUVIS_0011/DATA/D2005_172/) and search for data with observation time close to 03:35. Save the following data files and LBL files to your computer:
```
EUV2005_172_03_35.DAT
EUV2005_172_03_35.LBL
FUV2005_172_03_35.DAT
FUV2005_172_03_35.LBL
```

Note that the LBL files contain the description of this data set. Also note that EUV, FUV, HDAC, and HSP data are presented in the same directory.

4) Open the LBL files to determine the dimensionality, binning, and windowing of the data:
```
AXIS_NAME       = (BAND, LINE, SAMPLE)
CORE_ITEMS      = (1024, 64, 163)
UL_CORNER_LINE  = 2
UL_CORNER_BAND  = 0
LR_CORNER_LINE  = 61
LR_CORNER_BAND  = 1023
BAND_BIN        = 1
LINE_BIN        = 1
```

This information states that the data consist of 1024 spectral elements, called "bands" (spectral bins) from bin number 0 to 1023 with no spectral binning performed (spec_bin=BAND_BIN=1), in 60 lines (spatial bins) from line number 2 to 61 with no spatial binning performed (space_bin=LINE_BIN=1), and 163 samples (or records).

5) The user can select for use any programming language to read and analyze the data. The following example uses IDL to read the data:
```
data = read_binary( filename, data_dims=[ BAND, LINE, SAMPLE],
data_type=12, endian='big' )
```

Here the filename can be either FUV2005_172_03_35.DAT or EUV2005_172_03_35.DAT. The

data matrix's dimensions are (1024, 64, 163). Note that endian keyword is set to 'big' because the machine used to create the binary file follows big-endian byte ordering. Also note that in IDL, type code 12 refers to a 16-bit unsigned integer ranging from 0 to 65535.

6) Some supporting IDL codes and calibration files can be found on the PDS system associated with the data. For example, the users can go to the following URL:
http://pds-rings.seti.org/volumes/COUVIS_0011/SOFTWARE/CALIB/VERSION_3/
to download F_Flight_Wavelength.pro, which can provide the wavelength scale of the data.

7) Figure 1.1 can be generated by summing all the sample data from lines 2 and 61.
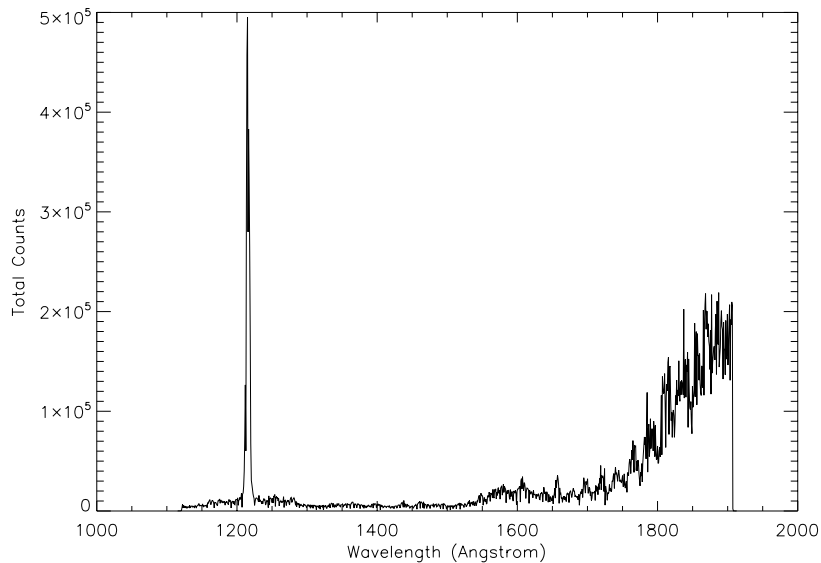
Figure 1.1 Cassini UVIS observation of Saturn's aurora on day 172 of year 2005.

Example 2: Phoebe observations were made during the flyby around 19:22 on day 163 of year 2004.

1) Go to the Cassini UVIS data website http://pds-rings.seti.org/cassini/uvis/access.html

2) Because the data was taken on day 163 of year 2004, find COUVIS_0007 in the table called "Temporal coverage of each volume"

3) Open http://pds-rings.seti.org/vol/COUVIS_0007/DATA/D2004_163/ and save the following data and LBL files:
FUV2004_163_19_22.LBL
FUV2004_163_19_22.DAT

4) Open the LBL files to determine the dimensionality, binning, and windowing of the data:

```
INTEGRATION_DURATION = 30.000 <SECOND>
AXIS_NAME            = (BAND, LINE, SAMPLE)
CORE_ITEMS           = (1024, 64, 132)
UL_CORNER_LINE       = 0
UL_CORNER_BAND       = 0
LR_CORNER_LINE       = 63
LR_CORNER_BAND       = 1023
BAND_BIN             = 1
LINE_BIN             = 1
```

This information states that the data consist of 1024 (spectral bins) from bin number 0 to 1023 with no spectral binning performed (spec_bin=BAND_BIN=1), 64 lines (spatial bins) from line number 0 to 63 with no spatial binning performed (space_bin=LINE_BIN=1), and 132 samples (or records). Also note that the integration duration is 30 seconds. This will be useful to convert raw counts into the count rate.

5) The user can select for use any programming language to read and analyze the data. The following example uses IDL to read the data:
```
data = read_binary( filename, data_dims=[ BAND, LINE, SAMPLE],
data_type=12, endian='big' )
```

6) Figure 1.2 can be generated by using the data at sample number 15. Note that to convert the raw counts to the count rate, the users will need to sum all lines, assuming that all lines observed the reflection from Phoebe, and divide the sum by 64x30. The value 30 comes from the 30 second integration duration and the value 64 is the total number of lines used in the observation. See Chapter 8 for more detailed information on the difference between the reflected spectra from Phoebe's dayside and nightside.
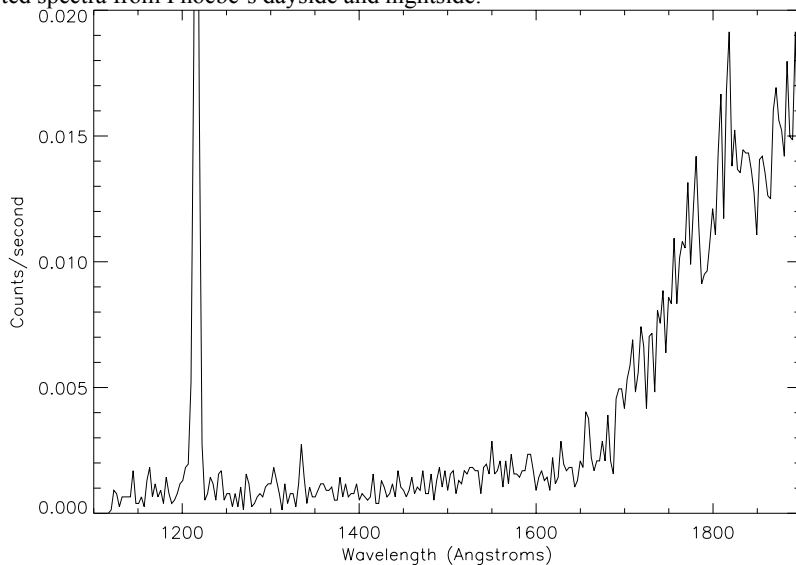
Figure 1.2: 2004 UVIS observation of Phoebe's dayside.

Example 3: An Enceladus occultation observation was carried out around UTC 19:54:56 on July 14th, 2005, which was day 195.

1)   Select COUVIS_0012 which contains the observation data. Then select DATA. This brings   us   to   the   following   webpage: http://pds-rings.seti.org/volumes/COUVIS_0012/DATA/D2005_195/. Download   the   data   set containing the closest starting time:

```
FUV2005_195_19_52.DAT
FUV2005_195_19_52.LBL
```

2) Open the LBL files to determine the dimensionality, binning, and windowing of the data:

```
AXIS_NAME                    = (BAND, LINE, SAMPLE)
CORE_ITEMS                   = (1024, 64, 71)
UL_CORNER_LINE               = 19
UL_CORNER_BAND               = 0
LR_CORNER_LINE               = 43
LR_CORNER_BAND               = 1023
BAND_BIN                     = 2
LINE_BIN                     = 1
```

Now we have all the files needed for the 2005 Enceladus occultation observation. Note that the Enceladus observation data is stored in a 3-dimensional array [1024, 64, 71]. As described in the data label, only lines between 19 and 43 contain valid data. And only the first 512 wavelength (band) bins contain valid data because in this particular observation a spectral binning by 2 is carried out.

3) The user can select to use any programming language to read and analyze the data. The following example uses IDL to read the data:

```
data = read_binary( filename, data_dims=[ BAND, LINE, SAMPLE],
data_type=12, endian='big' )
```

4) Figure 1.3 can be generated by using the Enceladus data. Note that the users will need to sum all spatial elements (lines) of the corresponding samples in order to obtain the total raw counts as shown in Figure 1.3.
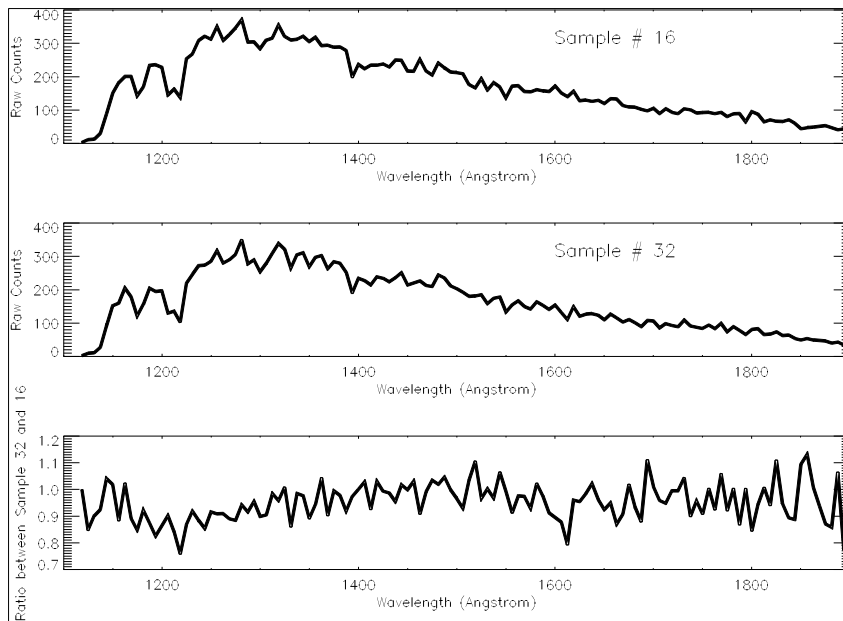
Figure 1.3: Cassini UVIS observation during the 2005 Enceladus occultation event. The upper panel is the FUV spectrum of the target star at sample record number 16, which is before the occultation. The middle panel corresponds to sample record number 32, during the occultation. The lower panel shows the division between sample 32 and 16, which can be matched with the absorption features of water vapor (see Hansen et al. 2006).

In the above, we provide some examples on how different data types can be retrieved from the PDS. The PDS archive contains instructions for reading the data that provide an alternative to the instructions given here. Generally, each COUVIS directory consists of six separate directories: CALIB, CATALOG, DATA, DOCUMENT, INDEX, and SOFTWARE. These directories contain all the necessary information that is required to read and handle the data. The subdirectory SOFTWARE/READERS contains the file READERS_README.TXT that describes how the data can read into IDL. Basically the file describes an automated procedure that is used to generate a subroutine that reads both the data and calibration files from the appropriate DATA and CALIB subdirectories. It is important to note that if the reader wants to obtain both the data and the calibration matrix simultaneously with the methods described in the PDS, it will be necessary to download all of the subdirectories and files in the given COUVIS directory.

2. PDS Data Structure

David Judd

During the Cassini spacecraft's tour of the solar system, the Ultraviolet Imaging Spectrograph has observed Venus, Earth, the Jovian and Saturn systems. The UVIS science team has delivered data to the Planetary Data System for storage in an historical archive. PDS clients are able to search, retrieve and analyze this data. This chapter supports those users by providing a description of UVIS data and its organization within the PDS.

In PDS, an "observation" is the fundamental organizational unit of UVIS data. It is a set of integers representing detector counts obtained while the instrument had a particular configuration and was obtained for a particular purpose. A document entitled UVISREF.CAT is located in all UVIS data volumes at the PDS and describes the instrument in detail. In summary, it describes the four subsystems of the UVIS instrument: the Far Ultraviolet channel (FUV), the Extreme Ultraviolet channel (EUV), the High Speed Photometer (HSP) and the Hydrogen/Deuterium Absorption Cell (HDAC) and how they acquire data.

The four subsystems produce two PDS data types: 1) cubes; and 2) time series. The EUV and FUV channels use detectors with a 1024x64 array of pixels, which integrate over time to generate a three dimensional matrix. The axes of this matrix, using PDS terminology, are line, band, and sample. The line dimension is the detector's 64 pixel spatial dimension, the band is the 1024 pixel spectral dimension, and the sample dimension corresponds to time where each integration of the detector is arrayed in this dimension. A three dimensional matrix with these axes is referred to as a PDS cube. The HSP and HDAC are photometers which produce a time ordered sequence of photon counts, corresponding to a PDS time series.

Regardless of its PDS data structure, there are four UVIS data products: 1) spatial-spectral image cubes; 2) images; 3) spectra; 4) brightness time series. In each sample, a cube contains both spatial and spectral information about a target, the image contains only spatial information, and a spectrum contains only spectral information. The time series is a sequence of samples (photon counts). An image is generated from a cube by summing the detector counts across the entire wavelength dimension; a spectrum is generated from a cube by summing across the entire spatial dimension. The brightness time series is produced by the HSP or HDAC channels. These data products are illustrated in the following figures:

Figure 2.1A: A spatial-spectral image cube

64

$t_0+(2\ sec)$

$t_0+(1\ sec)$

t_0

1 ⟵ sum all pixels across the spectral dimension
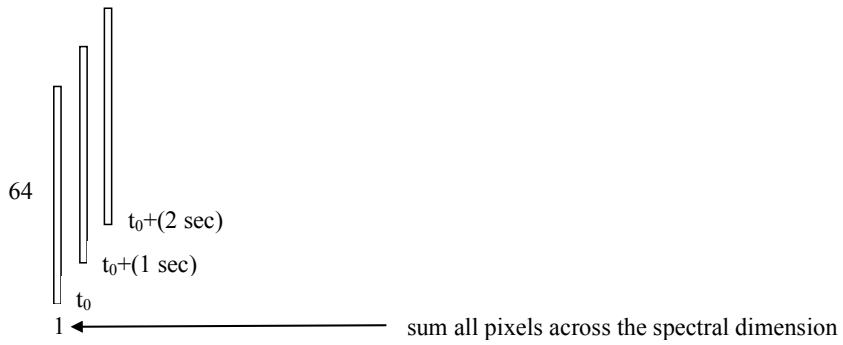
Figure 2.1B: An image at one wavelength

sum
all
spatial
pixels

t_2

t_1

1024

t_0
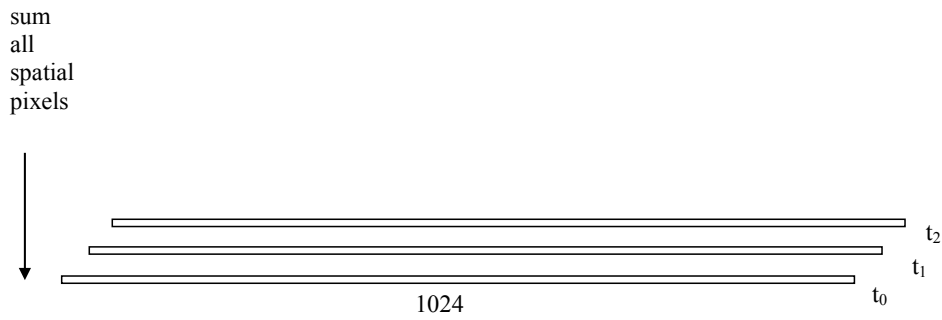
Figure 2.1C: A series of spectra.

A brightness series from the HSP or HDAC is a time series: $\{c_{t0},\ c_{t1},\ \ldots\}$.

The following surface plot Figure 2.2 is the first sample of a UVIS EUV spatial-spectral image cube from an observation of Jupiter:
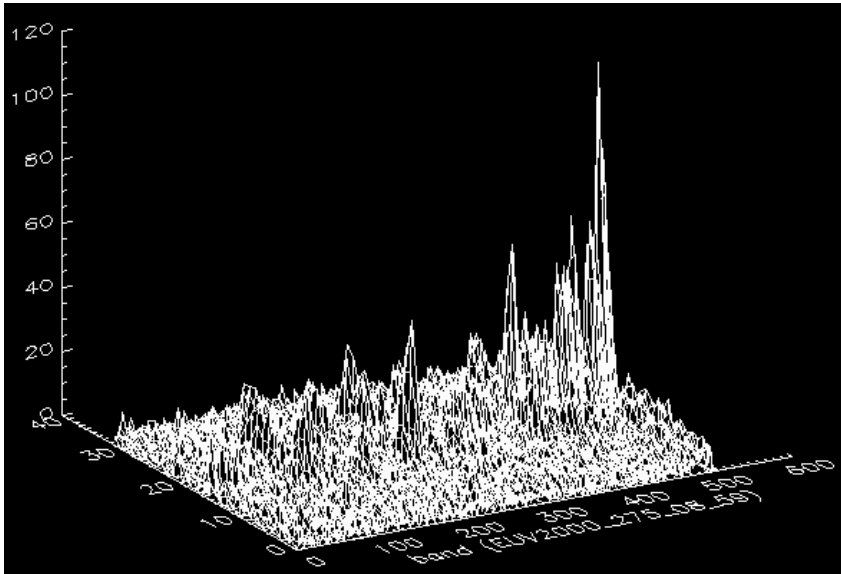
Figure 2.2: The first sample of a UVIS EUV spatial-spectral image cube observation of Jupiter. The elevated line at y=~20 is Jupiter. The elevated regions at Y=~15 and Y=~25 are emissions from the Io torus. There are 32 lines and 512 bands of data because the binning in this observation is 2 spatially and 2 spectrally.

The EUV and FUV channels can be configured to take data from sub-regions of the 1024x64 detector called windows. For example, if a target is expected to be visible in the central region of the detector then a window centered around the middle of the detector with an upper left corner at (0, 24) and a lower right corner at (1023, 39) with dimensions 1024x16 would capture the target and minimize irrelevant data. If a reduced level of resolution is possible, then the detector could be binned to further reduce the data size. Binning is the summation of adjacent pixels, for example, binning by 2 causes adjacent pairs of pixels to be added together. For example this [(0,24), (1023,39)] window could be binned by two in the band (spectral) dimension resulting in a 512x16 array of pixels. We take as an example two additional windows defined by window1 = ([0,10],[1023, 14], SpaBin=5, SpecBin=1) and window3 = ([0,50],[1023, 54], SpaBin=5, SpecBin=1). When windowing or binning is defined on the detector, counts are arranged within the matrix in sub-matrices corresponding to the

windows of the detector. Figure 2.3 illustrates this windowing and binning:

64
(0,10) window1

spatial bin is 5
(1023, 14)

(0,24) window2

Spectral bin is 2

(0,50) window3
(1023, 39)

spatial bin is 5
(1023, 54)
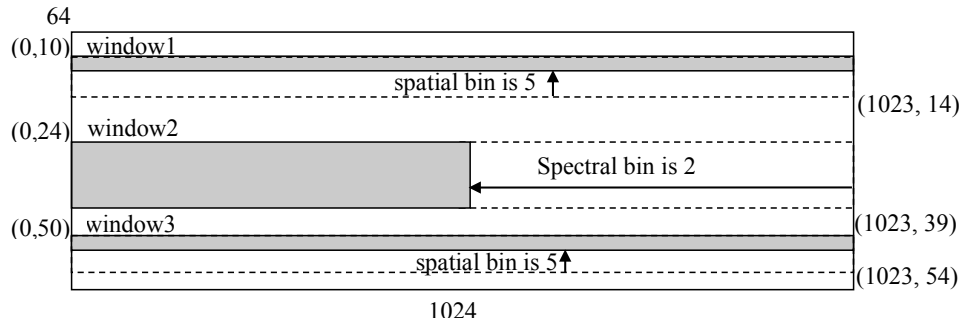
1024

Figure 2.3: an example of windows in the UVIS detector

The image, spectrum and cube data products are represented in the PDS as cubes. Images are 1 x 64 x n cubes, spectra are 1024 x 1 x n cubes and spatial-spectral image cubes are 1024 x 64 x n cubes. The following Figure 2.4 provides an example UVIS cube corresponding to the windowed and binned detector configuration in Figure 2.3:

64
(0,10)
(1023, 11)

(0,24)

(511, 39)

(0,50)

(1023, 51)
t_0

1024
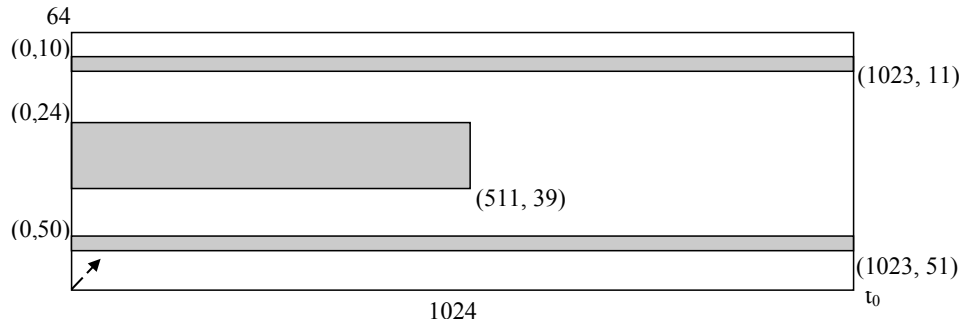
Figure 2.4: an example of PDS data corresponding to the example offered in diagram 2.3.

Matrix elements outside the windows contain null values (-1). Data counts are ordered in line-major ordering. This structural analogy between detector windows and cubes holds for spectra and images as well. The solar-stellar brightness series are represented as PDS Time Series objects that are, simply, a series of detector counts, each with an associated timestamp.

To this point we have seen several configurable aspects of the UVIS instrument, namely, integration time and the detector windowing and binning. Windows are defined by the upper left and lower right corners of the window and an associated spatial bin and spectral bin. These values are specified in the PDS using name/value pairs. In PDS format, the previous example had INTEGRATION_DURATION = 1 <SECOND>, and three windows defined using their upper left corner, lower right corner and binning:

```
UL_CORNER_SPECTRAL  = (0,0,0)
UL_CORNER_SPATIAL   = (10, 24, 50)
LR_SPECTRAL         = (1023, 1023, 1023)
```

```
LR_SPATIAL            = (14, 39, 54)
SPATIAL_BIN           = (5, 1, 5)
SPECTRAL_BIN          = (1, 2, 1)
```

The structure of a UVIS Cube is specified using the AXIS_NAME, CORE_ITEMS, CORE_ITEM_BYTES and CORE_ITEM_TYPE values. A 1024x64x10 UVIS Cube object is specified by:

```
AXIS_NAME                     = (BAND, LINE, SAMPLE)
CORE_ITEMS                    = (1024, 64, 10)
CORE_ITEM_BYTES               = 2
CORE_ITEM_TYPE                = MSB_UNSIGNED_INTEGER
```

A 1024x1x10 series of spectra is specified by:

```
AXIS_NAME                     = (BAND, LINE, SAMPLE)
CORE_ITEMS                    = (1024, 1, 10)
CORE_ITEM_BYTES               = 2
CORE_ITEM_TYPE                = MSB_UNSIGNED_INTEGER
```

Time series are specified using ROWS, COLUMNS, ROW_BYTES, and DATA_TYPE.
The following defines a 14912 element time series of 2 byte integers:

```
ROWS                      = 14912
COLUMNS                   = 1
SAMPLING_PARAMETER_NAME   = TIME
SAMPLING_PARAMETER_UNIT   = MILLISECOND
SAMPLING_PARAMETER_INTERVAL= 125
...
OBJECT                    = COLUMN
  NAME                    = PHOTOMETER_COUNTS
  DATA_TYPE               = MSB_UNSIGNED_INTEGER
  BYTES                   = 2
```

All UVIS data objects are composed of 2 byte unsigned integers, though all values are significantly less than 2^{16}.

The FUV and EUV channel data are converted into geophysical units by multiplying the matrix of raw data by a corresponding matrix of calibration coefficients. This calibration is continually updated by the UVIS Team, so the user may use the latest calibration data, or if preferred, use the calibration data matrix to convert model results to expected UVIS counts for comparison. This calibration matrix is a 2-dimensional array with the same BAND and LINE dimensions as its corresponding data object. The calibration matrix contains floating point values. The product of the data cube and the calibration cube is data whose geophysical units are kilorayleighs per angstrom. The mapping between detector columns and wavelengths is specified in the PDS BAND_BIN_CENTER value where each value in the list is a wavelength associated with the corresponding detector column. The process used to generate calibration coefficients is described in Chapter 3 of this user's guide. Because the calibration is continually updated, the calibration matrix may change with time. By providing the latest calibration coefficients, we allow the user to calibrate the raw data to geophysical units (alternately, users may use their own model of the target and the instrument response to compare to the raw data). See Chapter 9 for

this approach. HSP and HDAC data in raw form have units of counts (per integration period) and are proportional to photon flux. There is no additional calibration defined for these data.

PDS data objects have two components, a data component and a label component. The label contains a set of name/value pairs, including those listed above. The data file contains data values formatted into a PDS object. These components are stored as files whose names contain the extensions DAT and LBL respectively. UVIS data object file names have the form <channel><start_time>.LBL or <channel><start_time>.DAT. The LBL files contain instrument configuration, spacecraft geometry, and taxonomic information describing UVIS data within the PDS. Using the information within a LBL, a reader can understand the organization of data within the DAT file and extract that data into an analysis tool. For example, in the IDL programming language, the read_binary function can read a data Cube such as the one defined above:

```
r = read_binary('FUV2001_001_01_02.DAT', data_type = 2,
data_dims=[1024, 64, 10])
```

which returns a 1024x64x10 array of 2 byte integers. Similarly, read_binary can be used to read an HSP or HDAC data file since each is organized as a one dimensional array. Other configuration fields within a UVIS Cube label further describe the state of the instrument. For example:

```
SPACECRAFT_CLOCK_START_COUNT   = "1/1633050431.160"
SPACECRAFT_CLOCK_STOP_COUNT    = "UNK"
START_TIME                     = 2009-274T00:24:32.004
STOP_TIME                      = 2009-274T00:36:32.004
TARGET_NAME                    = "SOLAR WIND"
OBSERVATION_ID                 = 112818
INTEGRATION_DURATION           = 12.500 <SECOND>
COMPRESSION_TYPE               = "SQRT_9"
HI_VOLTAGE_POWER_SUPPLY_STATE  = ON
OCCULTATION_PORT_STATE         = OPEN
SLIT_STATE                     = OCCULTATION
TEST_PULSE_STATE               = OFF
ODC_ID                         = 103
DESCRIPTION                    = ". . ."
```

where the clock start is the Cassini clock time at the <u>end</u> of the first sample, the start time is a text string corresponding to the spacecraft clock start time, the stop time is a derived value produced by multiplying the INTEGRATION_DURATION by the number of samples, the target name is a value defined during operations planning, the OBSERVATION_ID is a unique numerical value associated with the observation, the INTEGRATION_DURATION is the time period used to generate each sample, the COMPRESSION_TYPE is the algorithm used by the UVIS flight software to encode data on-board and during transmission to earth, the HI_VOLTAGE_POWER_SUPPLY_STATE is the voltage level applied to the detector, the OCCULTATION_PORT_STATE is a flag indicating whether the occultation port is open or closed (i.e. whether the light source is being observed through the port), the SLIT_STATE describes the width of the spectrometer entrance, the TEST_PULSE_STATE indicates whether the data is internally-generated, and the ODC_ID is a numeric value identifying the configuration commands generated by the operations team for this observation. There are two DESCRIPTION

fields in a label. The first contains a reference to additional material for understanding the instrument state. The second contains a one line description of the purpose of the observation which has the form "The purpose of this observation is to…". The fields relevant to understanding data are spacecraft clock, target, integration, slit state and description. The other fields are less important and are included in the label because they are part of UVIS telemetry: high voltage state is always ON, test pulse is always OFF, ODC_ID is used exclusively in operations management, the compression algorithm, although lossy, has no significant effect on data quality, and observation ID is useful only as a reference point.

The HDAC replaces INTEGRATION_DURATION with DWELL_TIME and the H_LEVEL and D_LEVEL parameters. The time series generated by the HDAC channel may have additional complexity. If all the filament voltage levels are 0 then the HDAC is in photometer mode and its output is a time series of detector counts. If there is a non-zero filament voltage level the detector is in modulation mode and the time series can be mapped into a table of 32 columns, each column corresponding to an HDAC filament voltage level in the order: d1...d16, h1..h16 where d1..d16 correspond to the 16 voltage levels of the d cell and h1..h16 the same for the h cell. The time series can be converted to the table by mapping contiguous subsequences into the successive columns of the table. The length of the subsequence is equal to the dwell time parameter of the instrument configuration. A data product consists of a set of data taken during a single instrument configuration.

Label files contain spacecraft pointing geometry computed for the time at the end of the first integration at the center of the field of view of the instrument. The keywords specifying this geometry are:

```
RIGHT_ASCENSION, DECLINATION, SUB_SOLAR_LATITUDE,
SUB_SOLAR_LONGITUDE, SUB_SPACECRAFT_LATITUDE,
SUB_SPACECRAFT_LONGITUDE, PHASE_ANGLE, EMISSION_ANGLE,
INCIDENCE_ANGLE, CENTRAL_BODY_DISTANCE, PLANET_POSITION_VECTOR,
SC_PLANET_VELOCITY_VECTOR, SC_SUN_POSITION_VECTOR,
SC_SUN_VELOCITY_VECTOR, SC_TARGET_POSITION_VECTOR,
SC_TARGET_VELOCITY_VECTOR, PLANET_CENTER_POSITION_VECTOR,
PLANET_CENTER_VELOCITY_VECTOR
```

Their values are in units of degrees for angles, kilometers for distances, and kilometers/second for velocities and are given in the J2000 reference frame. Geometry values are generated using the NAIF SPICE toolkit. When a geometry value cannot be computed due to a dispersed target (such as observation of the interplanetary medium), or insufficient ephemeris data (such as when the target is off-center) a value of UNK is recorded as the parameter value. Since the number of interplanetary hydrogen survey observations with a target of SOLAR_WIND is relatively high, the number of UNK values is also high.

Data objects are stored in files within a data volume. A data volume is a directory tree whose content and structure is defined by PDS. The UVIS data volume has a name of the form COUVIS_nnnn where CO is an acronym for Cassini Orbiter, UVIS is the instrument name, and nnnn is a number in a sequence of indices. During the Cassini mission, UVIS produced data volumes from COUVIS_0001 through COUVIS_0060. The top level directory contains several directories and files:
- DATA contains data objects
- CALIB contains calibration objects

- DOCUMENT contains documentation
- CATALOG contains catalogs of data products on the volume
- SOFTWARE contains software (used for documentation only)
- AAREADME.TXT describes the data volume
- ERRATA.TXT describes know errors.

The UVIS data object files are organized by date under the DATA directory. The CALIB directory contains files that correspond, by name, to FUV and EUV data object files. These calibration files contain Cube data objects, used to convert raw counts into geophysical values. The calibration LBL files contain a description of the calibration process. The SOFTWARE directory contains algorithms used to generate these coefficients and are included for reference. The INDEX directory contains a relational database table whose columns are the fields of the LBL files and which contain the label values as records in the table. The purpose of the INDEX.TAB file is to provide a database search capability.

Underneath the DATA directory is a sequence of directories of the form D<yyyy>_<ddd> where yyyy is a year and ddd is a day of year. The contents of these directories are the observations that began on the specified day, for example,

COUVIS_0002/DATA/D2001_001/FUV2001_001_01_12.LBL. Underneath the CALIB directory is a subdirectory of the form VERSION_n and under that is the same directory tree as is under DATA, for example:

COUVIS_0002/CALIB/VERSION_2/D2001_001/FUV2001_001_01_12_CAL_2.LBL.
Note that as a rule the calibration file and its corresponding data object file have corresponding names. Examples of data and calibration labels are given in the appendices. A description of the calibration version is located in the SOFTWARE/CALIB directory of each PDS data volume.

Underneath the INDEX directory are two files, INDEX.LBL and INDEX.TAB. The INDEX.LBL file contains a schema definition for a relational database table. The TAB file contains a set of records corresponding to observations, one record per observation. One column contains the data file name and the rest correspond to the keywords in the observation label, e.g. START_TIME, TARGET_NAME, INTEGRATION_TIME, etc. The index table is used to search for observations matching some user-specified criteria.

Underneath the DOCUMENT directory is the UVIS.TXT file that is a more substantial version of this chapter. The CATALOG directory contains the files UVISINST.CAT and UVISREF.CAT that describe the instrument in detail. Also included there are a description of the mission, the spacecraft and the four UVIS data products. The SOFTWARE directory contains algorithms encoded in the IDL programming language that are used to generate calibration coefficients and geometry. They are included primarily for reference. An IDL data reader, UVIS_PDS_READ_DATA and associated documentation are also provided.

UVIS data are available from the Atmospheres and Rings nodes of the PDS. From PDS, users obtain observations formatted as PDS data objects. By reading the object's label a user can ascertain the structure of the data and load it into an analysis tool. The label contains all UVIS state information necessary to interpret the data. The steps detailed in this document will make it possible for UVIS data to be a valuable scientific resource into the foreseeable future.

3. UVIS Calibration

Greg Holsclaw

3.1 Introduction

This chapter provides an overview of the UVIS EUV and FUV channel calibration and demonstrates how to produce calibrated data products from a PDS dataset.

3.2 Instrument overview

The optical design of UVIS is described by McClintock et al. (1993) and the science investigation by Esposito et al. (2004). A description of the instrument is also provided in the file /CATALOG/UVISINST.txt found within any UVIS data volume in the PDS. A brief overview of the instrument relevant to the current discussion of calibration will be presented here. The Cassini Ultraviolet Imaging Spectrograph (UVIS) contains four separate remote sensing subsystems integrated in a single mechanical assembly. These subsystems are referred to as the Far Ultraviolet Spectrograph (FUV), the Extreme Ultraviolet Spectrograph (EUV), the High Speed Photometer (HSP) and the Hydrogen-Deuterium Absorption Cell (HDAC). Table 1 contains the design parameters for each subsystem. Because the interpretations of data from the EUV and FUV channels require a well-understood calibration, the rest of this chapter will be limited to these two subsystems only.

Table 3.1 Summary of the UltraViolet Imaging Spectrograph design specifications.

	FUV	**EUV**	**HSP**	**HDAC**
TELESCOPE				
Focal length (mm)	100	100	200	150 mm
Entrance pupil size (mm)	20 x 20	20 x 20	133 x 38	25 mm Dia
Reflecting surface (Material)	$Al + MgF_2$	Boron Carbide	$Al + MgF_2$	MgF_2
TOROIDAL GRATINGS				
Grating radii (mm)	300, 296.1	300, 296.8		
Grating surface	$Al + MgF_2$	Boron Carbide		
Grooves/mm	1066	1371		
Input angle a (degrees)	9.22	8.03		
Out angles b (degrees)	±2.45	-3.63, +1.27		
Dispersion (Å/mm)	31.18	24.20		
Dispersion (Å/pixel)	0.7794	0.6049		
3-POSITION SLITS				
Slit widths (microns)	75, 150, 800	100, 200,800		
Dl (Å) atmosphere	2.75, 4.8, 24.9	2.75, 4.8, 19.4		

Field of View (mrad)	(0.75, 1.5, 8)x60	(1, 2, 8)x59	6.0 (az) x 6.4 (el)	58 Dia (FWHM)
DETECTORS				
Photocathode	CsI	KBr	CsI	KBr
Detector window	MgF$_2$	none	MgF$_2$	MgF$_2$
Detector size (mm)	25.6 x 6.4	25.6 x 6.4	8 mm Dia	13 mm Dia
Pixel format (l x q)	1024 x 64	1024 x 64		
Pixel size (m)	25 x 100	25 x 100		

3.3 Terminology

As presented in Chapter 2, the NASA Planetary Data System (PDS) favors the terminology of 'line' and 'band' to describe the perpendicular dimensions of a two-dimensional array detector. However, the terms 'column' and 'row' are more often encountered. In this chapter, a column will refer to all the detector elements at a given wavelength center, each of which exists at a unique spatial location. Likewise, a row refers to all detector elements at a given spatial location, each of which exists at a unique wavelength center. Thus, 'columns' are equivalent to 'bands' while 'rows' are equivalent to 'lines'.

3.4 Radiometric equation

The number of counts recorded for a pixel at column i and row j can be expressed as:

$$C_{ij} = L_{ij} \cdot \frac{A_t \cdot A_s}{f^2} \cdot \frac{1}{K} \cdot FF_{ij} \cdot T_i \cdot QE_i \cdot \delta\lambda_i \cdot t + B_{ij} + S_{ij} \qquad (3.1)$$

where L_{ij} is the radiance at that pixel, A_t is the area of the telescope entrance pupil (20 × 20 mm), A_s is the area of the entrance slit (three slits per channel, see Table 1), f is telescope focal length (100 mm), K is the number of rows illuminated by the image of a filled slit (60 for FUV, 59 for EUV), FF_{ij} is the pixel-to-pixel sensitivity variation (also known as the "flat field", see Section 3.5), T_i is the system transmission (i.e. mirror reflectance, grating efficiency, and window transmission), QE is the quantum efficiency (detected counts per incident photon), $\delta\lambda_i$ is the spectral width of a pixel (average of 0.07794 nm for FUV, 0.0609 nm for EUV), t is the integration time (seconds), B_{ij} is any background signal present, and S_{ij} is scattered light.

The sensitivity of the instrument was measured during laboratory calibration prior to launch. Using this instrument sensitivity, the recorded counts can be converted to geophysical units:

$$L_{ij} = (C_{ij} - B_{ij} - S_{ij}) \cdot M_{ij} \qquad (3.2)$$

where M_{ij} is the inverse of the sensitivity and has units of kilorayleigh count[-1] angstrom[-1]:

$$M_{ij} = \frac{f^2}{A_t \cdot A_s} \cdot K \cdot \frac{1}{FF_{ij} \cdot T_i \cdot QE_i \cdot \delta\lambda_i \cdot t} \qquad (3.3)$$

Note that the calibration matrix provided at the PDS includes the integration time, and so the user does not need to derive count rate (as would be more typical) before applying the calibration. Calibrated values, resulting from the multiplication of the data and the calibration matrix, will carry units of kilorayleigh per angstrom. The derived radiance value in Eqn. 3.2 has

significance only if the entrance slit width and pixel height (spatial dimension) is filled by the target. The dark current of the UVIS CODACON detectors is expected to be negligible.

A persistent source of background B is thought to be caused by the radioisotope thermoelectric generators (RTGs) that power the Cassini spacecraft. Figure 3.1 shows a measure of the FUV detector background over time, calculated by finding the mean value of all pixels in the detector area defined by columns 950 to 1015 and rows 2 to 60 extracted from routine observations of interplanetary hydrogen. Values derived from observations using the high-resolution and low-resolution entrance slit are shown separately. The background from the low-resolution data is slightly, but systematically larger than the background determined from the high-resolution data. This difference indicates a small contribution of scattered Lyman-alpha, as the low-resolution entrance slit is twice the width of the high-resolution slit. After filtering out extreme values (those outside +/-30% of the median), an exponential function was fit to the low-resolution data and is shown as the solid line in the Figure 3.1. Values above the primary trend indicate contamination by stars or planetary bodies that have entered the field of view, or due to ring-crossing events that have been found to significantly increase the UVIS detector background. Values below the primary trend indicate partial data loss during downlink. The decrease in UVIS detector background is qualitatively consistent with the expected decay of ^{238}Pu within the RTGs.

Another source of background is the relatively bright signal due to solar emission at the Lyman-α wavelength (121.6 nm) scattered by interplanetary hydrogen (IPH). Due to scattering within the spectrograph (see section 3.5), this IPH signal is detectable across much of the FUV detector as well as the long-wavelength end of the EUV detector. It is recommended that background estimates be determined for each observation independently.
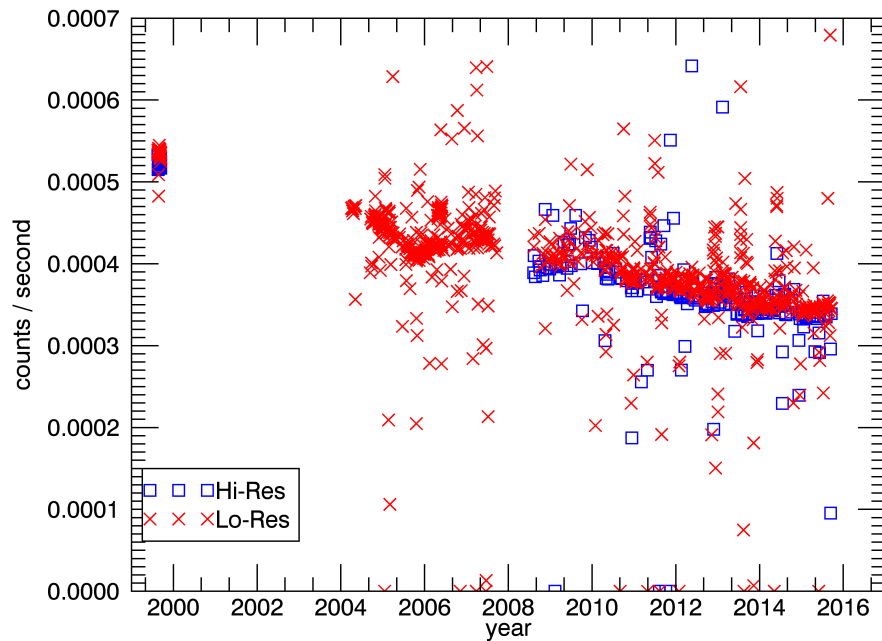
Figure 3.1 – Background count rate in the FUV detector as a function of time.

3.5 Spectrometer scattered light

The scattering properties of a spectrometer will redistribute signal at any wavelength to other positions across the detector in a predictable manner. Ideally, a monochromatic point source would be used to characterize this point-spread function (PSF). While there is no such source available in-flight, sunlight scattered by interplanetary hydrogen can provide an essentially monochromatic, though spatially extended, source.

In 1999, a campaign consisting of many long-exposure observations was conducted to measure the instrument response to illumination by the IPH. Figure 3.2 shows an average FUV spectrum from these observations using the low-resolution entrance slit. An analytic model defined by a Gaussian function (to characterize the central, high signal portion of the PSF) plus a Lorentzian function (to characterize the broad, low-signal wings) is given in Equation 3.2. Because the signal originates from an extended source, the function must be convolved with a rectangular function representing the geometric image of the low-resolution entrance aperture. The model given in Eqn 3.2 was fit to the data, and is shown as a dashed line in Figure 3.2. The model coefficients from this fit are listed in Table 3.2.
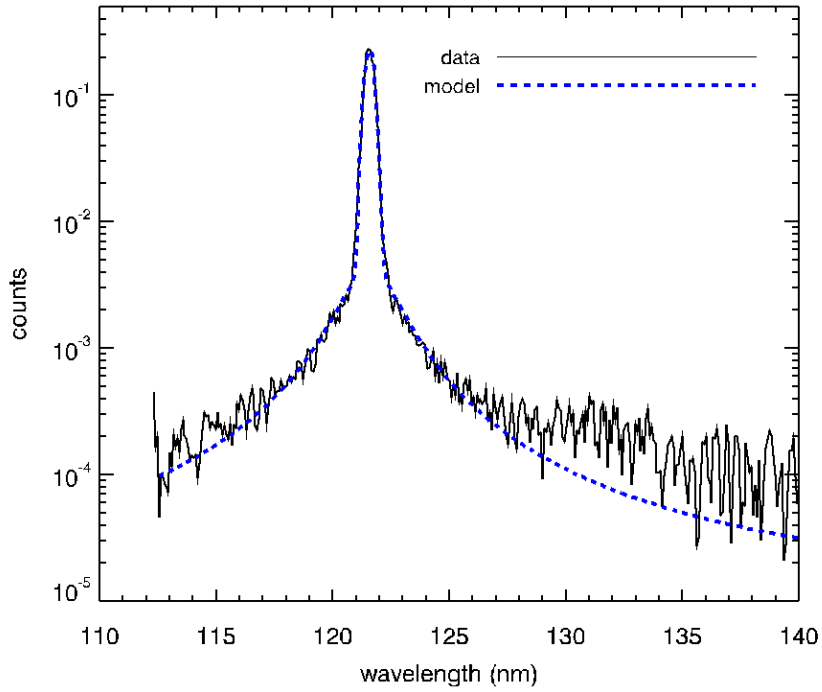
Figure 3.2 – Average FUV spectrum of interplanetary hydrogen along with a fit to an analytic function.

$$f = \left[a_0 + a_1 \cdot \exp\left(\frac{-0.5(x - a_2)^2}{a_3^2} \right) + \frac{a_4}{1 + \dfrac{1}{a_5}(x - a_2)^2} \right] \otimes rect\left(\frac{x - a_2}{w} \right) \tag{3.2}$$

Table 3.2 – Coefficients of the model given in Eqn. 3.2 after fitting to the data shown in Figure 3.2.

a_0	0
a_1	0.318
a_2	121.569
a_3	0.149
a_4	0.00373
a_5	1.507

3.6 In-flight updates to the calibration

The calibration of the instrument has been monitored during flight by acquiring periodic observations of the star α Virginis (Spica). Initial analysis of measurements obtained after launch indicated that the stellar spectrum was consistent with results from previous investigators. However, later observations revealed that the sensitivity of the long-wavelength end of the FUV detector was actually *increasing* with time. The nature of this change is still not completely understood. In any case, a time-varying sensitivity was formulated and has been applied to all data obtained since launch.

Other changes to the instrument sensitivity have been noted over time. Around June 6, 2002 a long observation of the star Spica was executed to characterize the scattering properties of the Imaging Science Subsystem (ISS) cameras onboard Cassini. Although the UVIS instrument did not acquire any data at this time, the relatively high photon flux resulted in a decrease in the sensitivity in the central few rows (~30-33) of both the EUV and FUV detector. This event is referred to as the "starburn" and is discussed in more detail by Steffl (2005). The loss in sensitivity is proportional to the photon flux at any wavelength, and so the effect appears as an inverted spectrum of Spica.

The flat-field response (pixel-to-pixel sensitivity variation) of the instrument detectors was not characterized prior to launch. A series of observations of Spica were obtained which slewed the stellar image across the spectrograph entrance slit in a pattern such that a relative pixel-to-pixel response could be derived. This procedure is documented in Appendix A of Steffl (2005). A flat-field corrector matrix was derived for both the time before and the time after the starburn event. The post-burn matrix attempts to correct for the loss in sensitivity in rows 30-33 due to the starburn. The FUV flat-field correction matrix can be found in any UVIS PDS volume under /SOFTWARE/CALIB/VERSION_n/ where n is an integer indicating the calibration version number. As of March 2014, version 3 is the most current.

It has been noted that the sensitivity in the starburn region continues to decrease over time, likely due to the repeated use of bright stars like Spica as a source for occultation measurements. The sensitivity loss appears to be proportional to the integrated photon flux over time. There are other examples of regional sensitivity loss from this effect, especially in the FUV detector. The FUV occultation slit was often left in position following routine measurements of IPH. This allowed a significant flux of Lyman- α photons to fall on the detector in the clear regions above and below the occultation lens holder. The effect is a loss in sensitivity in a region where the image of the occultation slit would appear at a wavelength of 121.6 nm within rows 2-12, 51-61. The planet Saturn, its moons, and the rings enter the field-of-view while the FUV occultation slit is in position, though the instrument may not be acquiring data. Because these objects scatter incident sunlight, a significant flux of photons is incident on the detector at long wavelengths (where the solar irradiance is large). The effect, again, is the decrease in sensitivity in the region above and below the occultation slit lens holder (rows 2-12, 51-61) at the long-wavelength end of the FUV detector.

In order to mitigate these regional losses in sensitivity, a procedure was developed to derive correction values. This was accomplished by first identifying detector rows that are within the region obscured by the FUV occultation lens holder (rows 18-23, 41-46). Next, the relative response of each column to the average value from these "reference" rows is calculated for a stellar calibration where a star is slewed along the slit, creating an effective extended object. The inverse of these values, referred to as a "flat-field modifier", is derived for every successful stellar calibration. A correction matrix is linearly interpolated with time for any observation that occurs between calibrations.

All corrections and adjustments to the UVIS sensitivity that have been discussed here are included with the UVIS calibration matrix delivered to the PDS.

3.7 Anomalous pixels

A population of anomalous pixels has been identified on the FUV detector. These pixels are characterized by a relatively low response and they also may exhibit a nonlinear response. These pixels are often referred to as "evil" and they comprise ~15% of all detector elements. Although these anomalous pixels are distributed across the entire FUV detector, they often appear in groups along individual columns. Because of the poorly characterized response of these evil pixels, the UVIS team has decided to eliminate them from analysis. This is implemented by assigning an invalid sensitivity to the calibration matrix for these elements. Evil pixels are flagged as invalid by assigning them the CORE_NULL value indicated in any calibration label file, and this value is -1 for the current (version 3) calibration.

The approach described above creates an irregular grid of data. There are several methods for dealing with such datasets, and one suggested approach is to linearly interpolate across any flagged pixel. An IDL routine is provided by the UVIS team to perform this interpolation (interpolate_nans2.pro), and its use will be described in an example later in this chapter.

The presence of such flagged pixels creates a unique problem for binned data. Since binning occurs within the instrument's flight software, there is no way to recover the value of a "good" pixel that has been combined with an "evil" pixel. The flagging of evil pixels in the calibration matrix forces any binned element to also retain this value. The effect of this approach is that for larger bin sizes, a larger fraction of invalid (flagged) pixels will be present in the data. For moderate levels of binning, the interpolation approach may still be a useful option. However, for some datasets the binning is so large that the calibration matrix contains invalid (flagged) pixels exclusively. Such datasets may yet yield useful information, but special consideration is required on a case-by-case basis. Any user interested in analyzing such a dataset is encouraged to contact a UVIS team member.

One approach to estimate the response of anomalous pixels in heavily binned data is provided in Chapter 4.

3.8 Example calibration of a PDS dataset

The UVIS Data Product Software Interface Specification (SIS) document provides a detailed description of the UVIS data format, structure and content delivered to the PDS. The SIS document can be found within any UVIS data volume (/DOCUMENT/UVIS.TXT). The user is also referred to Chapter 2.

The PDS does not provide calibrated UVIS data. Instead, the raw, observed counts from the instrument are stored in one data file and a calibration matrix is stored in a separate file. These files are located within different directories of a UVIS data volume (/DATA/ and /CALIB/, respectively).

The following is a step-by-step example, written in the interpretative language of IDL (http://www.exelisvis.com/), of the data reduction involved for one UVIS observation. After this example, a simpler approach will be shown that uses a provided data reader (UVIS_PDS_READ_DATA), written in IDL, to import the data for analysis. Consider an atmospheric limb measurement of Titan where the UVIS boresight was held at a constant altitude

throughout the observation and consists of 15 scans (individual detector readouts) each with an integration time of 240 seconds. The EUV and FUV data files and associated calibration matrices are contained in the following files:

```
/COUVIS_0027/DATA/D2009_173/EUV2009_173_15_16.DAT
/COUVIS_0027/CALIB/VERSION_3/D2009_173/EUV2009_173_15_16_CAL_3.D
     AT
/COUVIS_0027/DATA/D2009_173/FUV2009_173_15_16.DAT
/COUVIS_0027/CALIB/VERSION_3/D2009_173/FUV2009_173_15_16_CAL_3.D
     AT
```

These files can be located at the UVIS PDS repository at http://pds-rings.seti.org/cassini/uvis/access.html. Metadata contained in the EUV label file:

```
/COUVIS_0027/DATA/D2009_173/EUV2009_173_15_16.LBL
```

indicates the dimensionality, data type, and any scaling required by the following entries (identical for the FUV data):

```
AXIS_NAME                   = (BAND, LINE, SAMPLE)
CORE_ITEMS                  = (1024, 64, 15)
CORE_ITEM_BYTES             = 2
CORE_ITEM_TYPE              = MSB_UNSIGNED_INTEGER
CORE_BASE                   = 0.0
CORE_MULTIPLIER             = 1.0
```

Using this information, the following IDL command can be used to read in the data:

```
data_euv = read_binary( 'EUV2009_173_15_16.DAT',
     data_dims=[1024,64,15], data_type=12, endian='big' )
data_fuv = read_binary( 'FUV2009_173_15_16.DAT',
     data_dims=[1024,64,15], data_type=12, endian='big' )
```

Note that endian keyword is set to 'big' because the machine used to create the binary file follows big-endian byte ordering. Also note that in IDL, type code 12 refers to a 16-bit unsigned integer ranging from 0 to 65535. The CORE_BASE is zero, which indicates no offsets are required, and CORE_MULTIPLIER is unity, which indicates there is no scaling of the data required. In a similar way, the calibration matrix can be read in by the following commands:

```
cal_euv = read_binary( 'EUV2009_173_15_16_CAL_3.DAT',
     data_dims=[1024,64,1], data_type=4, endian='big' )
cal_fuv = read_binary( 'FUV2009_173_15_16_CAL_3.DAT',
     data_dims=[1024,64,1], data_type=4, endian='big' )
```

Note that IDL type code 4 refers to 32 bit floating-point values. All UVIS PDS data, regardless of windowing and binning, is contained within a 1024x64 matrix (see Chapter 2). The binning

and windowing of the data is described in the following label entries (identical for the data and calibration files):

```
UL_CORNER_LINE              = 2
UL_CORNER_BAND              = 0
LR_CORNER_LINE              = 61
LR_CORNER_BAND              = 1023
BAND_BIN                    = 1
LINE_BIN                    = 1
```

The valid region of the arrays then needs to be extracted based on the above information:

```
x1 = UL_CORNER_BAND
x2 = UL_CORNER_BAND + (LR_CORNER_BAND-UL_CORNER_BAND+1) /
     BAND_BIN - 1
y1 = UL_CORNER_LINE
y2 = UL_CORNER_LINE + (LR_CORNER_LINE-UL_CORNER_LINE+1) /
     LINE_BIN - 1

dataw_euv = float(data_euv[x1:x2,y1:y2,*])
calw_euv  = cal_euv[x1:x2,y1:y2]
dataw_fuv = float(data_fuv[x1:x2,y1:y2,*])
calw_fuv  = cal_fuv[x1:x2,y1:y2]
```

The instructions above are given explicitly in order to assist a user in the production of a data reader in IDL or another language. An IDL routine with this functionality is provided at the UVIS PDS Atmospheres node website (http://atmos.nmsu.edu/data_and_services/atmospheres_data/Cassini/uvis.html). This routine requires that both the data file (.DAT) and label (.LBL) are present and located in the same path. The following example shows how the steps above can be accomplished using these routines:

```
UVIS_PDS_READ_DATA, 'EUV2009_173_15_16.DAT', dataw_euv
UVIS_PDS_READ_DATA, 'FUV2009_173_15_16.DAT', dataw_fuv
UVIS_PDS_READ_DATA, 'EUV2009_173_15_16_CAL_3.DAT', calw_euv
UVIS_PDS_READ_DATA, 'FUV2009_173_15_16_CAL_3.DAT', calw_fuv
```

Because all scans (time samples) were acquired at a fixed altitude above the Titan limb, we will average them together:

```
dataw_avg_euv = total(dataw_euv,3) / 15.
dataw_avg_fuv = total(dataw_fuv,3) / 15.
```

It is always recommended that the data be inspected prior to applying the calibration matrix to look for unexpected anomalies and to estimate the background signal that needs to be subtracted. Figure 3.1 shows the average detector counts as an image (smoothed with a 5x3 rectangular kernel and scaled from 0 to 0.6 counts) and a spectrum derived by then averaging the signal in the spatial dimension (across rows). The EUV image (top left panel) shows that there

appears to be little or no detectable signal below ~85 nm; however, there is a small amount of anomalous signal that appears in the upper left corner of the detector, and shows up in the average spectrum (bottom left panel) at ~60 nm. This is likely a residual signal from the "mesa" – a known contamination occurring in this region of the detector due to undispersed light entering through the solar occultation port (see Chapters 4 and 11).
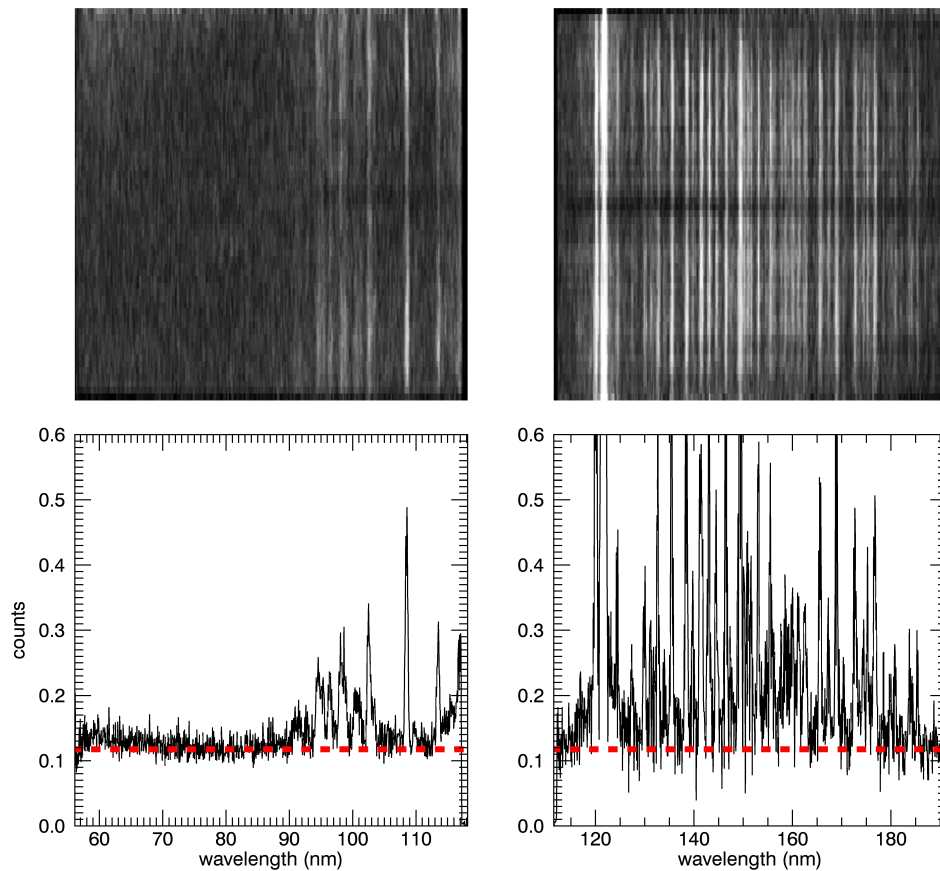

Figure 3.3 - Top panels: image of the average EUV (left) and FUV (right) array. Bottom panels: spatially averaged EUV (left) and FUV (right) spectrum. Images have been scaled from 0 to 0.6 counts.

We can estimate the EUV background by finding the mean pixel value in a region with no apparent photon-generated signal:

```
background_euv = mean( dataw_avg_euv[300:500,0:30] )
```

This background (0.118 counts) is shown as a dashed line in the EUV spectrum in the lower-left panel of Figure 3.3. Given the integration time of 240 seconds, this equates to a background rate is 4.9e-4 counts per second – slightly larger than the predicted RTG signal from Figure 3.3. The EUV background value also appears to be a good estimate of the FUV channel (dashed line in the lower right panel of Figure 3.3), as it is consistent with the signal at the short- and long-wavelength ends of the FUV spectrum.

Before calibrating the data, any anomalous or "evil" pixels need to be flagged. While the measured counts from these pixels are recorded in the data file, the associated elements of the calibration matrix are assigned the CORE_NULL value (-1) indicated in the PDS label file. To facilitate the interpolation across these invalid pixels, they will be replaced with a special value within the IDL environment (Not-a-Number or NaN):

```
core_null = -1
ndx_null = where( calw_euv eq core_null, count_null )
if count_null gt 0 then calw_euv[ndx_null] = !values.f_nan
ndx_null = where( calw_fuv eq core_null, count_null )
if count_null gt 0 then calw_fuv[ndx_null] = !values.f_nan
```

Next, the background is subtracted from the data and the result multiplied by the calibration matrix:

```
arrcal_euv = (dataw_avg_euv-background_euv)*calw_euv
arrcal_fuv = (dataw_avg_fuv-background_fuv)*calw_fuv
```

Recall that we have assigned the FUV background value to be equal to that for the EUV.

The final step is to interpolate across invalid pixels. A simple row-by-row IDL interpolation routine (interpolate_nans2.pro) is provided by the UVIS team on the PDS website under any UVIS volume at /SOFTWARE/CALIB/VERSION_n/ where n is an integer indicating the calibration version number (n=3 as of March 2012). The following commands illustrate the usage of this routine:

```
interpolate_nans2,arrcal_euv,arrcali_euv
interpolate_nans2,arrcal_fuv,arrcali_fuv
```

Figure 3.4 shows images of the calibrated EUV and FUV arrays along with the average spectrum for each channel. Here we have converted the units from kilorayleigh per angstrom to rayleigh per angstrom, and scaled the results from 0 to 2. An analysis of this dataset is reported in Ajello et al (2012).

Greg Holsclaw 2/24/2014 3:03 PM
Comment [1]: revise

Aeronomers are typically familiar with the rayleigh unit, but researchers in other disciplines, who are also users of UVIS data, may not be. The rayleigh was originally defined as a photon emission rate from an observed column of gas. However, using some assumptions, the rayleigh can be interpreted as an apparent surface radiance (Baker and Romick, 1976):

$$1 \text{ rayleigh} = \frac{10^6}{4\pi} \text{ ph s}^{-1} \text{ cm}^{-2} \text{ sr}^{-1}$$

It is this relationship that provides the link between the quantity of radiance (power or photon rate per unit area per unit solid angle) measured by remote sensing instrumentation and the reported column emission rate expected by aeronomers.
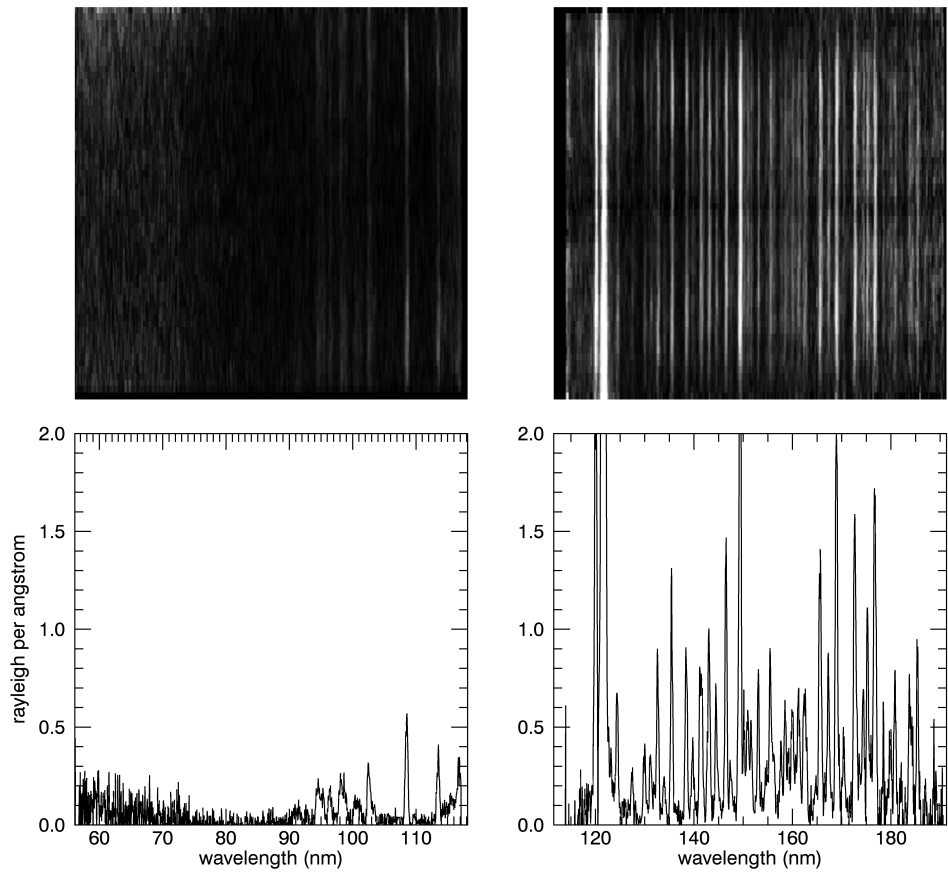
Page 31 (7/31/18 - 9:26 AM)

Figure 3.4 – Top panels: image of the calibrated average EUV (left) and FUV (right) array. Bottom panels: spatially averaged calibrated EUV (left) and FUV (right) spectrum. Images have been scaled from 0 to 2 rayleigh per angstrom.

4. Saturn's Aurora

-- How to calibrate observations from Saturn's poles

Jacques Gustin

4.1 Introduction

In a very general sense, the aurora are luminous phenomena resulting from the collision between precipitating charged particles and the atmosphere of a planet. Following this definition, aurora have been observed at Venus, Earth, Mars, Jupiter, Saturn, Uranus, Neptune and even at a few satellites (Io, Europa, Ganymede). Aurora have always been observed on Earth and started to be studied in a scientific way in the 17th century. Giant steps forward have been taken since that time, thanks to the start of the space exploration in the late fifties. Several spacecraft and scientific instruments have been launched and have observed the aurora of the different planets, in multiple wavelength ranges (e.g., Voyager 1 and 2, Galileo, Image, FUSE, the Hubble Space Telescope). The Cassini-Huygens spacecraft follows these renowned missions and has provided unique data on Saturn's system since 2004.

In the case of Saturn, the auroral photons in the UV are produced by the interaction between the atmosphere and magnetospheric electrons. The magnetospheric electrons precipitating into the atmosphere undergo elastic and inelastic collisions with the H_2 molecules of the upper atmosphere and create secondary electrons through ionizations (see for example Grodent et al., 2001 for more details on this process). The FUV auroral emission is dominated by the H_2 Lyman $(B^1\Sigma^+_u \rightarrow X^1\Sigma^+_g)$ and Werner $(C^1\Pi_u \rightarrow X^1\Sigma^+_g)$ system bands and the Lyman continuum in the 900-1700 Å bandwidth. Below 1200 Å, the emission includes the higher energetic Rydberg transitions $(B'^1\Sigma^+_u \rightarrow X^1\Sigma^+_g , D^1\Pi_u \rightarrow X^1\Sigma^+_g , B''^1\Sigma^+_u \rightarrow X^1\Sigma^+_g$, and $D'^1\Pi_u \rightarrow X^1\Sigma^+_g)$ (see Figure 3 of Gustin et al, 2004 for more details). The auroral emission also includes lines from the atomic hydrogen Lyman series (HLy-α at 1216 Å, Hly-β at 1025 Å,...).

The aurora can be studied through UVIS spectroscopic and imaging capabilities:

- *Low-resolution spectroscopy*. The auroral emission is potentially attenuated by the hydrocarbon layer situated near the auroral peak. The main hydrocarbon responsible for absorption is methane (CH_4), which has a significant absorption cross-section shortward of 1350 Å. By comparing the observed spectra with un-attenuated H_2 spectra (obtained from a model or from laboratory measurements), the methane column can be derived. A model of the atmosphere (like Moses et al. 2000) is then used to relate this methane column to the pressure level and the H_2 column overlying the auroral emission peak. The energy deposition of the precipitated electrons can then be estimated from a stopping power table, which gives the average path length traveled by monoenergetic electrons into H_2, as they slow down to rest. Examples of this procedure may be found in the following references: Gustin et al., (2004, 2009), Dols et al., (2000), Ajello et al., (2005). All the UVIS auroral observations to date have been obtained with the low-resolution slit, providing spectra at ~5.5 Å FWHM. Although this resolution is high enough to examine the effect of hydrocarbons on the auroral emission, it is too low to resolve the individual rotational lines and provide information on the temperature of the gas.

- *Imaging*. By slewing the 1024x64 slit above a region of interest, UVIS is able to acquire images of the polar aurora. Images can be used to study the morphology of the aurora, determine

the brightness of the different auroral features and their variations with time, or investigate the interaction between the ionosphere, the magnetosphere and the solar wind. See for example Grodent et al. (2003) or Clarke et al., (2005) for more details on the auroral morphology and ionosphere/magnetosphere interactions.

4.2 Calibration procedures

The PDS web site contains two types of UVIS files: the raw data (*.DAT, in counts) and a calibration matrix (*_CAL.DAT). The calibrated data in kilorayleigh per angstrom are obtained by multiplying the raw data by the calibration matrix. For the EUV data, the combination of raw data and calibration matrix provides the final product in kilorayleigh per angstrom for all datasets. In the FUV, special consideration is required on a case-by-case basis because of the low response of the "evil" pixels described in Chapter 3. Indeed, the UVIS datasets may be binned in the spectral and/or spatial dimensions onboard Cassini to reduce data volume. If the binning is moderate (BIN<4), the raw FUV data and calibration matrix provide the final product in kilorayleigh per angstrom. If the binning is heavier than 4, the calibration matrix automatically produced (*_cal.DAT) is not valid and the calibration needs special requirements. This chapter gives details on the general calibration procedure for both the EUV and FUV UVIS channels, with an emphasis on the FUV channel calibration in the case of heavily binned data.

It should be noted that the EUV and FUV data can be calibrated by using the "cube generator" software described in Chapter 12. Cube Generator provides both the raw and calibrated data, as well as all the geometric parameters needed to determine the field of view of the instrument, the distance to the planet, the solar phase angle, etc. Cube Generator may be used to calibrate all the EUV and the moderately binned FUV data but is not appropriate for the heavily binned datasets.

4.2.1. Read the data

The UVIS data in PDS are posted at http://pds-rings.seti.org/cassini/uvis/access.html
Each dataset is composed of a *.DAT files containing the data and a *.LBL file containing important information on how the data have been obtained (See also Chapter 2). Here are the main variables needed to read/calibrate the data in the *.LBL file for dataset FUV2005_172_03_35.DAT:

```
AXIS_NAME                    = (BAND, LINE, SAMPLE)
CORE_ITEMS                   = (1024, 64, 163)
FILE_RECORDS                 = 163
SPACECRAFT_CLOCK_START_COUNT = "1/1498017812.897"
INTEGRATION_DURATION         = 240.000 <SECOND>
SLIT_STATE                   = LOW_RESOLUTION
UL_CORNER_LINE               = 2
UL_CORNER_BAND               = 0
LR_CORNER_LINE               = 61
LR_CORNER_BAND               = 1023
BAND_BIN                     = 1
LINE_BIN                     = 1
```

In this case, 163 records (SAMPLE) of 240 seconds have been obtained, each of them characterized by 1024 pixels in the spectra dimension (BAND) and 64 pixels in the spatial dimension (LINE).

Important notes:
a. If data compression has been performed onboard, the pixels in the spectral and/or spatial direction are <u>summed</u>, although the abuse of language "rebin" is often used instead. The keywords BAND BIN and LINE BIN give the bin performed in the spectral and spatial directions, respectively.
b. The illuminated matrix of a given observation may be different from the [1024 x 64] matrix of the detector. The keywords UL_CORNER_LINE, UL_CORNER_BAND, LR_CORNER_LINE and LR_CORNER_BAND delimit the four corners of the detector sub-array containing valid data.

To read the EUV set obtained on 2005 DOY 172 at 03:35, do:

```
data=read_binary(EUV2005_172_03_35.DAT',data_dims=[1024, 64,
163], endian='big', data_type=12)
```

For the FUV counterpart:

```
data=read_binary(FUV2005_172_03_35.DAT',data_dims=[1024, 64,
163], endian='big', data_type=12)
```

4.2.2. EUV calibration

Four aspects should be taken into account in the calibration process: the background noise due to the RTG, the "mesa", the flatfield, and the conversion from counts to physical units.

- RTG: The RTGs produce a constant background noise of $\sim 4 \times 10^{-4}$ counts/pixel that needs to be subtracted from the observation. If the data have been summed onboard, the RTG background must be multiplied by LINE_BIN and BAND_BIN before subtraction.
- A small light leak allows undispersed interplanetary H Lyman-α to reach the EUV detector for pixels <720, corresponding to wavelength shorter than 920 Å. This creates a background referred as the "mesa" by the UVIS team. This problem is solved by having the occultation port open during the EUV/FUV observations, which masks the leak on UVIS flight measurements since 2007-124.

For observations obtained before this date, the data must be carefully examined to determine if the mesa is present or not. If it is there, it should be manually subtracted from the data using a calibration observation performed on 16 April 2007, when the telescope was pointed on the sky. It allowed the mesa background alone to be recorded, which can be scaled and removed from the EUV data. It should be noted that the spectral shape of the observation background may be slightly different from the 16 April 2007 background, as the observed source is not necessarily uniform. In that case, spectral rows that are viewing into space should be used instead to define a background to subtract.

- For wavelengths $>\sim 1150$ Å (EUV pixel 971), another wavelength dependent background arises from internal instrument scattering of H Lyman-α. This contribution to the EUV signal is small below 1170 Å, and is estimated to be less than 7% of the total signal, based on

comparisons with a modeled H_2 spectrum (Ajello et al., 2005). To account for this background, the user should use a UVIS observation of the interplanetary H Lyman-α, scale it to the Lyman-α line of the dataset under consideration and remove from the dataset the interplanetary H Lyman-α seen in the EUV.

• When all the noise sources discussed above are subtracted from the signal, the raw observation is ready for the next procedures. The first is the application of a flatfield. Two flatfields are available. The first must be applied to the data for observations performed before June 6 2002 (FLATFIELD_EUV_PREBURN) and the other one for more recent observations, which is the case for all auroral data (FLATFIELD_EUV_POSTBURN). The flatfield (FFD) must be first put into the size of the observation and then rebinned:

•

```
IDL>FFD = FFD(UL_CORNER_BAND: LR_CORNER_BAND, UL_CORNER_BAND:
LR_CORNER_LINE)
IDL>FFD = rebin(FFD,spectral dimension,spatial dimension)
```

For each record, FFD must then be used as a multiplier to the data matrix, previously converted into counts seconds^{-1}.

• The last step of the procedure is produce the calibration curve which converts the counts sec^{-1} to kilo-Rayleigh Å^{-1} and provides the wavelength scale. This is done with the "Get_EUV_03_Lab_Calibration.pro" and "E_Flight_Wavelength.pro" procedures found at http://pds-rings.seti.org/volumes/COUVIS_0011/SOFTWARE/CALIB/VERSION_1/. Four keywords are needed before running it:

- bin_definition = [band_bin,line_bin]
- window_definition=[ul_corner_band,ul_corner_line,lr_corner_band,lr_corner_line]
- input_spectrum : selects calibration for continuous spectra (1) or for discrete lines (2). The auroral data require input_spectrum=1
- slit_width: selects ocultation (0), low_resolution (1), or high_resolution (2) slit. To date, all the auroral data have been collected with the low resolution slit.
- SPACECRAFT_CLOCK_START: determined by SPACECRAFT_CLOCK_START_COUNT. In our case, SPACECRAFT_CLOCK_START =1498017812.897

After compilation of E_Flight_Wavelength.pro and Get_EUV_03_Lab_Calibration.pro, run Get_EUV_03_Lab_Calibration:

```
IDL>Get_EUV_03_Lab_Calibration,e_wavelength,e_calibration,e_cali
bration_error,slit_width,input_spectrum,window_definition,bin_de
finition,spacecraft_clock_start
```

The main outputs of Get_EUV_03_Lab_Calibration are:
- e_wavelength: wavelength scale associated to the spectral dimension
- e_calibration: calibration array that needs to be multiplied to the data to get the final calibrated file.

From a calibrated file [x,y,z], a sum of rows in the x dimension produces an image, a sum of rows y and z produces a spectrum. Figure 4.1 shows an example of EUV auroral H_2 spectrum after calibration.
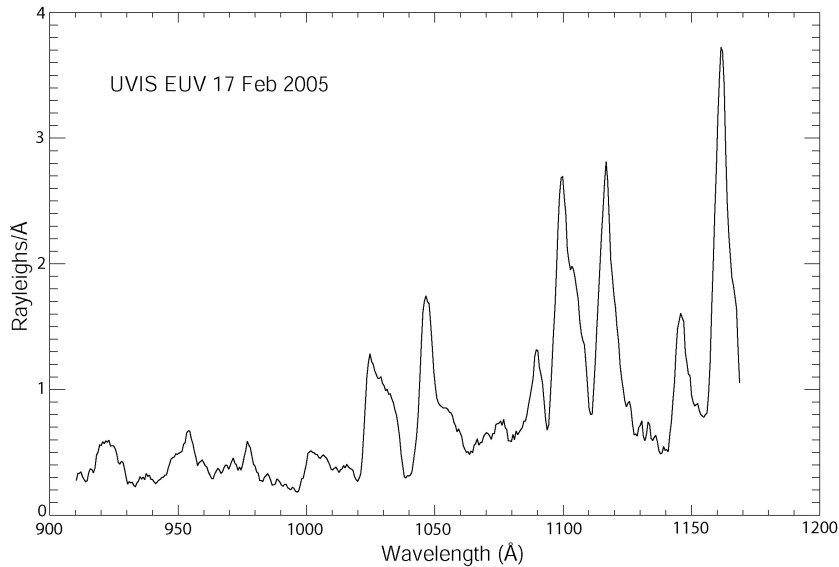
Figure 4.1: Example of EUV auroral H_2 spectrum after calibration (from Gustin et al., 2009)

4.2.3 FUV calibration

The FUV channel data require several steps before analysis The following points have been detailed in Chapter 3 and are summarized here:

- The FUV detector experienced a change in sensitivity as a function of wavelength and time (see Chapters 3 and 9 for more details). The sensitivity is stable with time for wavelengths ~1300 Å and below, while an increase is observed at longer wavelength. This problem has been addressed by observing the star Spica in a regular basis and fit an exponential function to the fractional change over time at each wavelength. A "red patch" has been included in the FUV calibration routine (Get_FUV_07_Lab_Calibration.pro) in order to deliver a time-dependent calibration curve that accounts for this problem.

For data with a spectral rebin lower or equal to 2, the calibration approach described below is exactly the same as that in Chapter 3. The data can thus be calibrated by using the *._CAL.DAT file or Cube Generator. A significant number of pixels in the FUV detector exhibit anomalously low responses relative to their immediate neighbors. They are called "evil pixels" by the UVIS team. In order to eliminate the effect of these pixels, they are replaced with NaNs (not-a-numbers) in the FUV flatflield files and can then be interpolated (see Chapter 3). These NaNs may be a problem for heavily binned data because the Nan's are included in the calibration curve in the calibration routines and as a result for data with a spectral rebin higher than 2, the calibration curve becomes Nan for every spectral pixels and unusable. Thus a different calibration approach than that in Chapter 3 has been taken for the heavily binned data of the FUV observations.

- *Spectral and/or spatial rebin ≤ 2:*

The procedure is identical to the EUV pipeline:

- Once the data are read and converted into counts sec^{-1}, the RTG background must be subtracted to the data. This is the only background observed in the FUV channel.

- Compile F_Flight_Wavelength.pro and Get_FUV_07_Lab_Calibration.pro and run Get_FUV_07_Lab_Calibration with slit_width, input_spectrum, window_definition and bin_definition as previously defined. The files FLATFIELD_FUV_POSTBURN.txt and FLATFIELD_FUV_PREBURN.txt are required in the working directory (posted at http://pds-rings.seti.org/volumes/COUVIS_0011/SOFTWARE/CALIB/VERSION_1/):

-
```
IDL>Get_FUV_07_Lab_Calibration,f_wavelength,f_calibration,f_cali
bration_error,slit_width,input_spectrum,window_definition,bin_de
finition, spacecraft_clock_start
```

gives the wavelength scale (F_WAVELENGTH) and the conversion from counts sec^{-1} to kR Å^{-1} (F_CALIBRATION). Since the flatfield is already applied in the Get_FUV_07_Lab_Calibration procedure, F_CALIBRATION contains the NaN. Once F_CALIBRATION has been applied to the data as a multiplier, the data array needs to be interpolated to the evil pixel. This is done with the procedure interpolate_nans2.pro.

- After compilation of interpolate_nans2, run it the following way:

-
```
IDL>interpolate_nans2, UVIS_kRA1, UVIS_kRA2
```

with UVIS_kRA1 the data before interpolation. UVIS_kRA2 is the array with the final calibrated data.

The product obtained following the above mentioned procedure corresponds to the output obtained from the "cube-generator". In the case of a rebin>2, the calibration is not handled by the "cube-generator" and the following procedure should be applied instead:

- *Spectral and/or spatial rebin > 2:*

Here the rebin of the "f_calibration" vector is altered by the large number of NaNs. This is why the approach must be different from what is described above and in Chapter 3: the interpolation of the calibration curve must be performed before its rebin to the size of the data.

Apply Get_FUV_07_Lab_Calibration.pro with the keywords defined in the previous paragraph: window_definition, input_spectrum, slit_width,bin_definition= [1, line_bin]
This gives 1) F_WAVELENGTH as a 1024 vector that needs to be scaled to the spectral dimension x of the data:

```
IDL> f_wavelength=rebin(f_wavelength,x)
```

and 2) F_CALIBRATION with 1024 pixels in the spectral dimension, with the NaNs. This matrix must be first interpolated to the evil pixels (NaNs) and then rebinned to the dimension of the data. It has then to be divided by the spectral rebin (the data are not rebinned in the sense of the IDL routine, but summed by bins of the size of the spectral rebin).

After conversion of the data to counts sec^{-1} and application of the RTG, the data must be multiplied by the new F_CALIBRATION array. Since the pre-flight lab-based measurements implicitly include the evil pixel, the interpolation of F_CALIBRATION underestimates the sensitivity by ~10%. The data need to be multiplied by 1.10 to get the final calibrated

observations. The two plots in Figure 4.2 and Figure 4.3 show the FUV spectra from FUV2005_172_03_35.DAT, before and after calibration respectively:
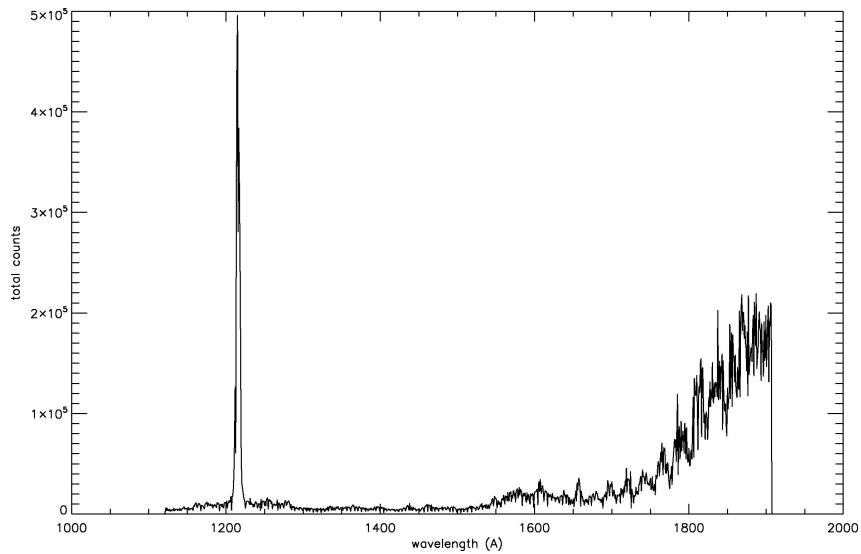

Figure 4.2: A raw spectrum of UVIS auroral observation from 2005 DOY172. In this example, all the raw spatial pixels and records (samples) have been summed.
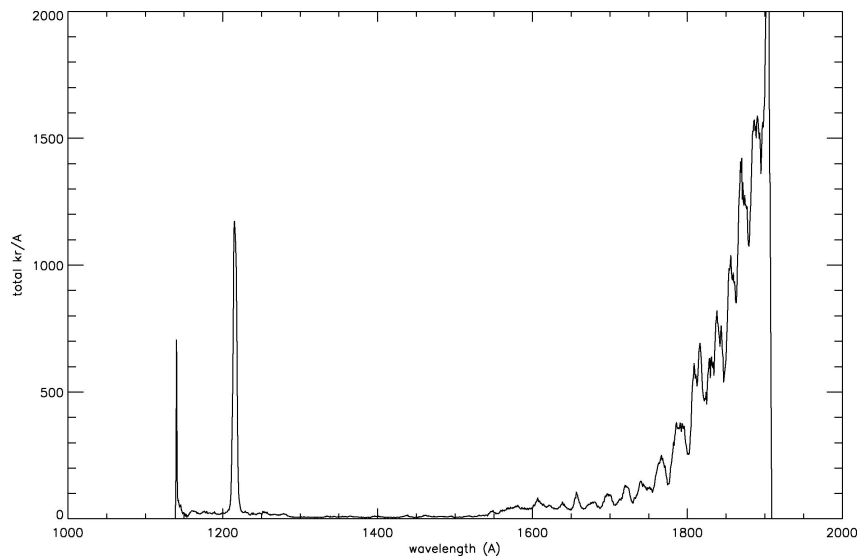
Figure 4.3: Same data as the observation shown in Figure 4.2 but with calibration carried out. It is seen that the flatfield has an important effect on the pixel-to-pixel intensity distribution, while the calibration curve enhances the two sides of the spectrum:

Image with all the spectral pixels summed from the raw data:
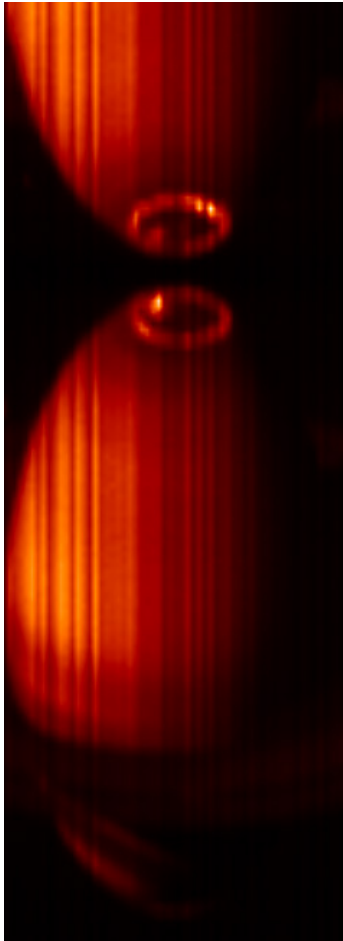
Image with all the spectral pixels summed from the calibrated data:
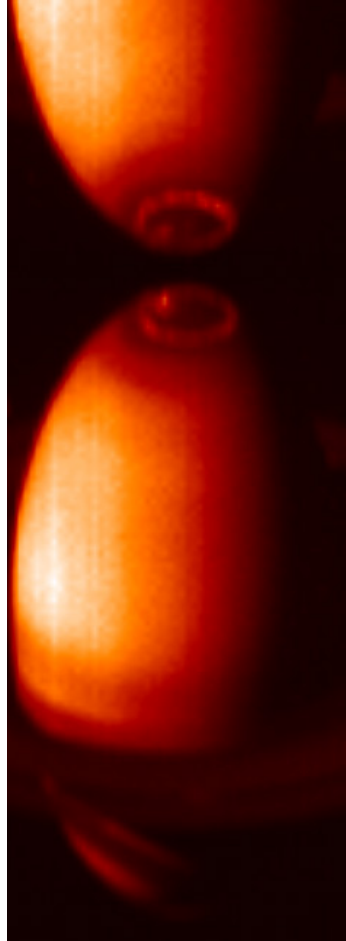
Figure 4.4: Same data as the observation shown in Figure 4.2 but here only the spectral pixels have been summed: the image corresponds to the successive records put together.

This example illustrates well 1) the effect of the flatfield (vertical stripes in the left image) and 2) the effect of the calibration curve, which enhances the long wavelength part of the spectrum (i.e. the reflected sunlight) in the right image.
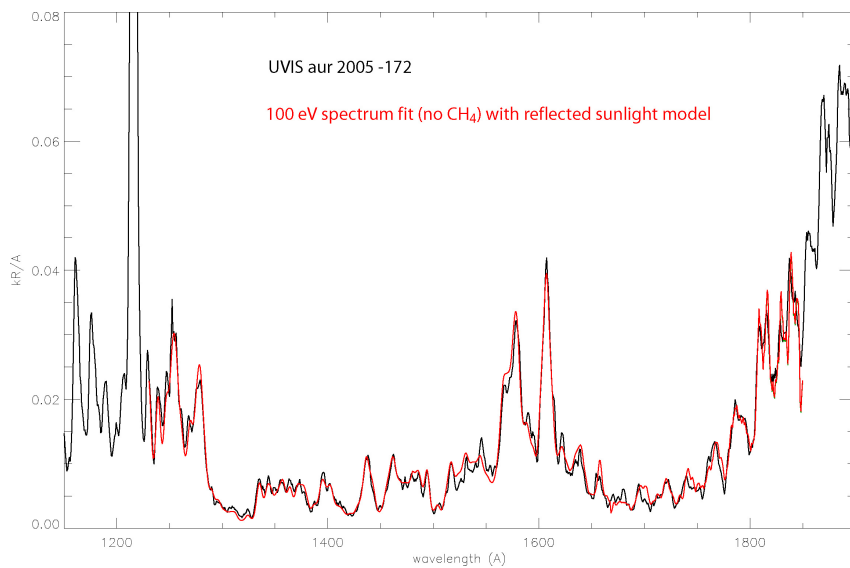
Figure 4.5: Comparison of the auroral spectrum observation in Figure 4.2 and a model that includes reflected sunlight model and a H_2 laboratory spectrum obtained from electron impact.

The previous examples show one of the few observation where the full spectral resolution has been preserved, providing spectra at ~5.5 Å resolution. In most of the cases, the data have been binned by 16 or 32 in the spectral dimension. The following example shows the shape of an auroral H_2 spectrum binned by 32. The main effect of the spectral rebin is to smooth the spectrum and cut off a big part of the H_2 features. The procedure described in paragraph 4.3 must be applied to get the final calibrated product.

Figure 4.6: An auroral H_2 spectrum binned by 32.

Final note: The pixels at the four edges of the detectors often exhibit odd behaviors in terms of quantum efficiency and calibration reliability (see for example the 1st and 2nd pixel in the last example). This is why it is strongly suggested to reject these pixels in any analysis.

5. HDAC Observations

Pascal Hedelt

5.1 Introduction

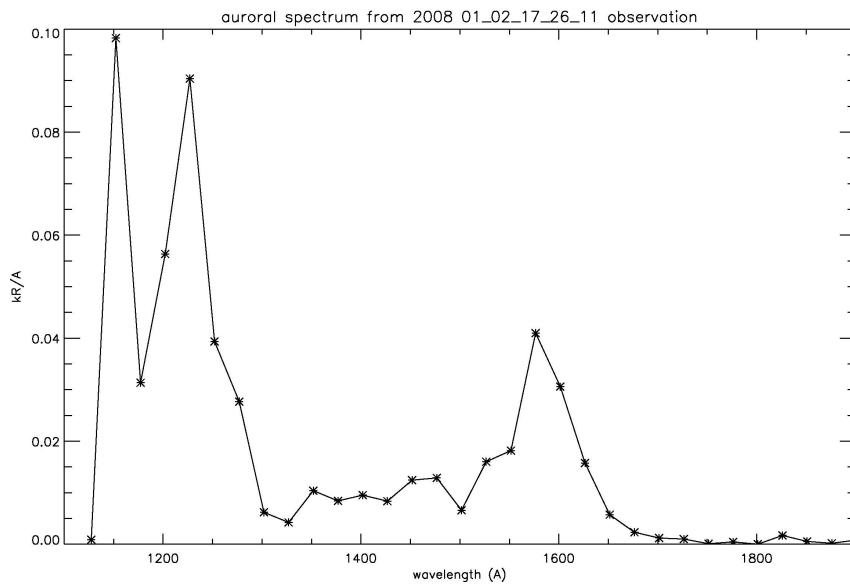The Hydrogen Deuterium Absorption Cell (HDAC) is part of the Ultraviolet Imaging Spectrograph (UVIS) aboard the Cassini orbiter. The HDAC instrument was designed to determine the D/H ratio of Titan's and Saturn's atmospheres. HDAC measures the relative abundance of atomic deuterium and hydrogen from their Lyman-α emission at 121.533nm and 121.567nm, respectively. A general description of UVIS and HDAC can be found in Esposito et al. (2004). Due to problems with the instrument (see below), the D/H ratio cannot be determined. Nevertheless, the H cell can be used e.g. to infer exospheric atomic hydrogen densities. For this reason, the only target observed so far was Titan.

HDAC consists of a baffle for suppressing scattered light, three absorption cells and a Channel Electron Multiplier (CEM) as a photon detector (denoted 'detector' in Figure 5.1). One HDAC absorption cell consists of a long tube, 8.5 cm in length and with a diameter of 2.5 cm, separated by Magnesium fluoride (MgF$_2$) windows. MgF$_2$ has a transmission range between 115 nm and 7,500 nm (Heath and Sacher 1966). A single 2.5 cm diameter MgF$_2$ lens attached to the front of the instrument focuses the incoming light onto the detector, yielding a circular field of view (FOV) of 3 deg in diameter ($6.85 \cdot 10^{-4}$ steradians).

The absorption cells are filled with molecular hydrogen, oxygen and deuterium, respectively. Oxygen acts as a broad band filter from 115 nm to 180 nm, except for a transmissive window in the Lyman-α region (Maki 1993). Unfortunately, the oxygen cell had to be vented prior to flight; hence HDAC is now sensitive to a very broad wavelength range from 115 nm to 240 nm. (see Figure 11 in Esposito et al. 2004).

The hydrogen and deuterium cells (hereafter referred to as 'H cell' and 'D cell') are heated via a hot tungsten filament to dissociate the molecules into atoms. The atoms resonantly absorb the hydrogen and deuterium Lyman-α radiation passing through the cells, which leads to a decreasing count rate in the CEM. Thus, the cells act as adjustable filters: by switching the filaments on and off and measuring the differences in signal strength, the instrument can measure the intensity of the incoming Lyman-α radiation for atomic hydrogen and deuterium. Since the atomic density in the cells depends on the filament temperature only, a set of different absorption 'filters' can be attained. Note that the optical depth of molecular hydrogen and deuterium in the Lyman-α region is negligible compared to the optical depth of atomic hydrogen or deuterium. Furthermore the H and D Lyman lines are well separated, compared to the thermal width of the lines.
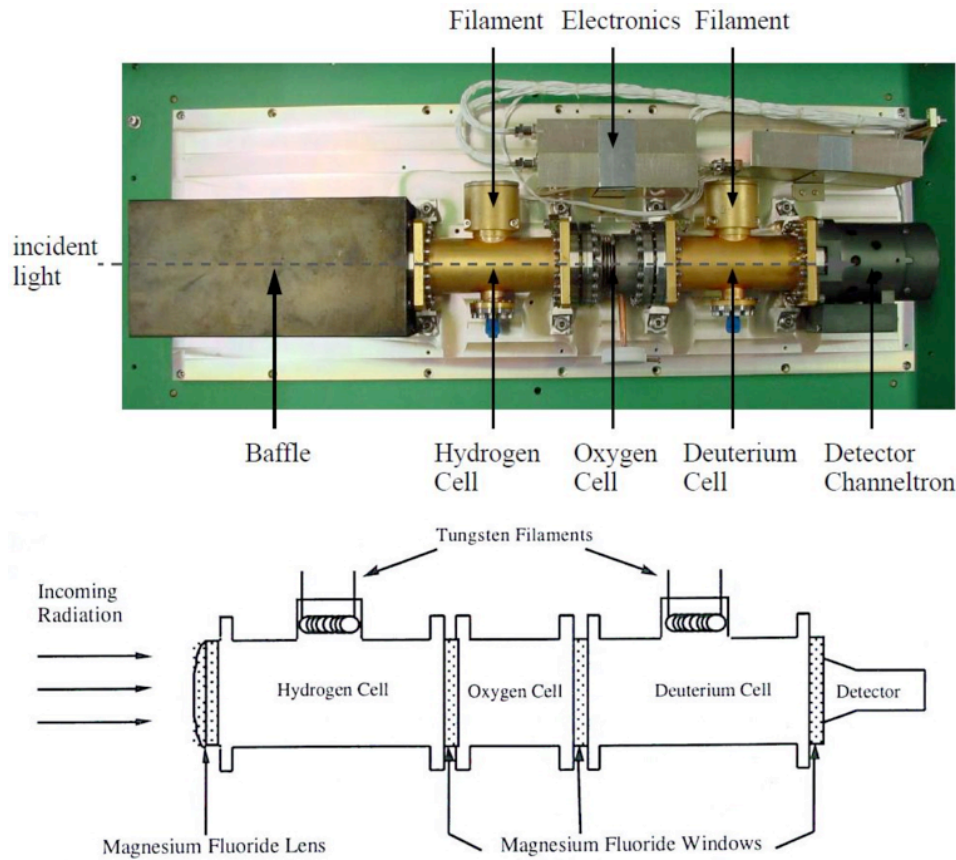
Figure 5.1: Detailed overview of the HDAC instrument (Esposito et al. 2004).

5.2 Measurement principle

The absorption cells are operated at a temperature of T_{HDAC} = 300K. When no power is applied to the filaments, the absorption cells contain only molecules, and the cells are transparent with respect to incoming Lyman-α radiation. When power is applied to the filament in the cell, the molecules dissociate into atoms, which weaken the incoming Lyman-α radiation by absorption. The wavelength-dependent transmission

$$\mathcal{T}(\lambda) = \exp\left[-n\sigma(\lambda, T_{HDAC})L\right] = \exp\left[-\tau(\lambda)\right] \qquad (5.1)$$

of the cells is a function of the length of the cell (L = 8.5 cm), the wavelength and temperature dependent resonance scattering cross section α (λ, T_{HDAC}), and the atomic number density n, which in turn depends on the filament power.

The wavelength dependent resonance scattering cross section of atomic hydrogen is given by

$$\sigma(\lambda, T_{\text{HDAC}}) = \sigma_0(T_{\text{HDAC}}) \exp\left(\frac{\lambda - \lambda_0}{\Delta\lambda}\right),$$

(5.2)

with σ_0 being the cross section at the line center ($\lambda_0 = 121.567$nm) and $\Delta\lambda$ the Doppler width. At a cell temperature of $T_{\text{HDAC}} = 300$K, the cross section for atomic hydrogen at the line center is $\sigma_0 = 3.4 \times 10^{-13}$ cm^2.

HDAC is sensitive to radiation over a wide spectral range, hence the signal measured is directly proportional to the integrated intensity of the incoming radiation over this range. The total signal can be expressed as

$$I = \int_0^\infty S(\lambda)H(\lambda)\mathcal{T}(\lambda)\mathrm{d}\lambda,$$

(5.3)

where I is the measured signal by the detector, $H(\lambda)$ is the intensity of the radiation, $S(\lambda)$ is the sensitivity of the whole instrument (including the sensitivity of the detector and the transmission of the MgF$_2$ windows), and $T(\lambda)$ is the transmission of the filter provided by the absorption cells. The ratio of the modulated intensity I (i.e. when the cell filaments are switched on) to the unmodulated intensity I_0 (i.e. when the cells do not absorb the incoming radiation) is given by the factor

$$R = \frac{I}{I_0} = \frac{\int_0^\infty S(\lambda)H(\lambda)\mathcal{T}(\lambda)\mathrm{d}\lambda}{\int_0^\infty S(\lambda)H(\lambda)\mathrm{d}\lambda}$$

(5.4)

assuming no background. Because the background level is unknown, it can be eliminated from the measurement by taking the difference of modulated and unmodulated signals, giving an effective filter

$$I_0 - I = \int_0^\infty S(\lambda)H(\lambda)[1 - \mathcal{T}(\lambda)]\mathrm{d}\lambda.$$

(5.5)

Due to the movement of the spacecraft with respect to Titan (resulting in a Doppler shift of the measured Lyman-α lines), HDAC is able to measure the line shape of the Lyman-α line: during ingress, the relative speed of the approaching spacecraft with respect to Titan is negative, hence the emitted Lyman-α radiation is shifted with respect to the HDAC absorption, allowing HDAC to absorb radiation redwards of the emitted radiation. Close to the closest approach the Doppler shift is zero, hence HDAC absorbs radiation exactly at the line center and during egress the blueward side of the Lyman-α radiation emitted by Titan is absorbed.

5.3 HDAC Calibration

Pre- and inflight cell calibrations have been summarized in Maki (1993), Warlich (1997) and Regehly (2003). Here the important points of these works are reviewed.

5.3.1 Sensitivity

The sensitivity $S_{\text{Ly}\alpha}$ of the instrument is the count rate per input flux:

$$S_{Ly\alpha} = \frac{10^6}{4\pi} \cdot QE \cdot \Omega \cdot \mathcal{T}_W^3 \cdot \mathcal{T}_L, \qquad (5.6)$$

where $S_{Ly\alpha}$ is in units of counts per second and Rayleigh (cts s^{-1} R^{-1}), QE is the quantum efficiency of the CEM detector in units of counts per photon (cts ph^{-1}), Ω is the solid angle of the FOV of HDAC in units of steradians, $T^3_W T_L$ is the transmission of the three MgF$_2$ windows and the single lens. $S_{Ly\alpha}$ is continuously calibrated using measurements of the local interstellar medium (LISM) and comparing them with a model. In general, the sensitivity of an instrument decreases with time, with the highest sensitivity at the beginning of the mission and then slowly decreasing to a stable value. See Figure 5.2 for the sensitivity change between the mission start and June 2010 (R. Reulke, priv. com.). The sensitivity of HDAC over the FOV is shown in Figure 5.3. Note that recent measurements of the HDAC sensitivity indicate a value of $S_{Ly\alpha} = 14$ cts s^{-1} R^{-1} for the year 2010 (R. Reulke, priv. com.).

The detector is able to detect radiation within two pre-defined integration times of 0.125 s and 4 s. Calibration measurements showed that the longer CEM integration times could lead to so-called rollover events. Rollover events mainly occur because the detector accuracy is limited to 16bit, hence the maximum number of counts is 65,536. If an overflow is detected, then its value is reset, leading to a spike in intensity. Hence for current observations, CEM integration times of 0.125 s have been chosen.
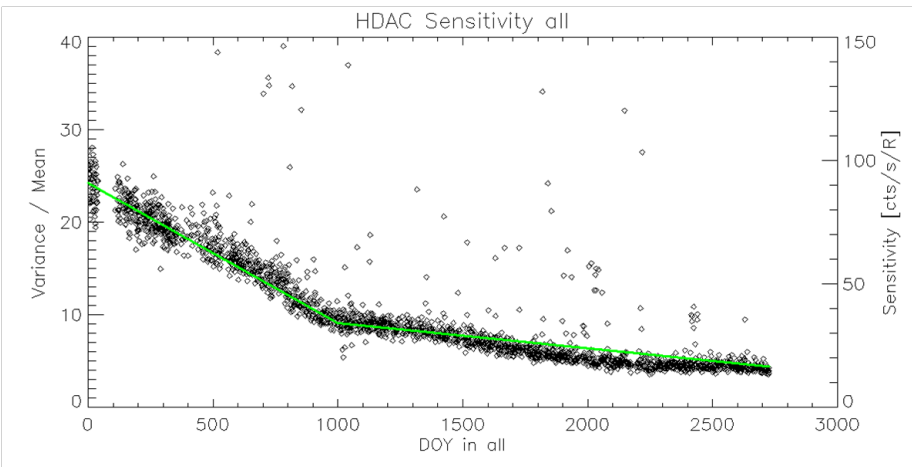

Figure 5.2: HDAC sensitivity change until June 2010. The sensitivity has been fitted by a linear fit (solid red line). Data provided by R. Reulke (priv. com.).
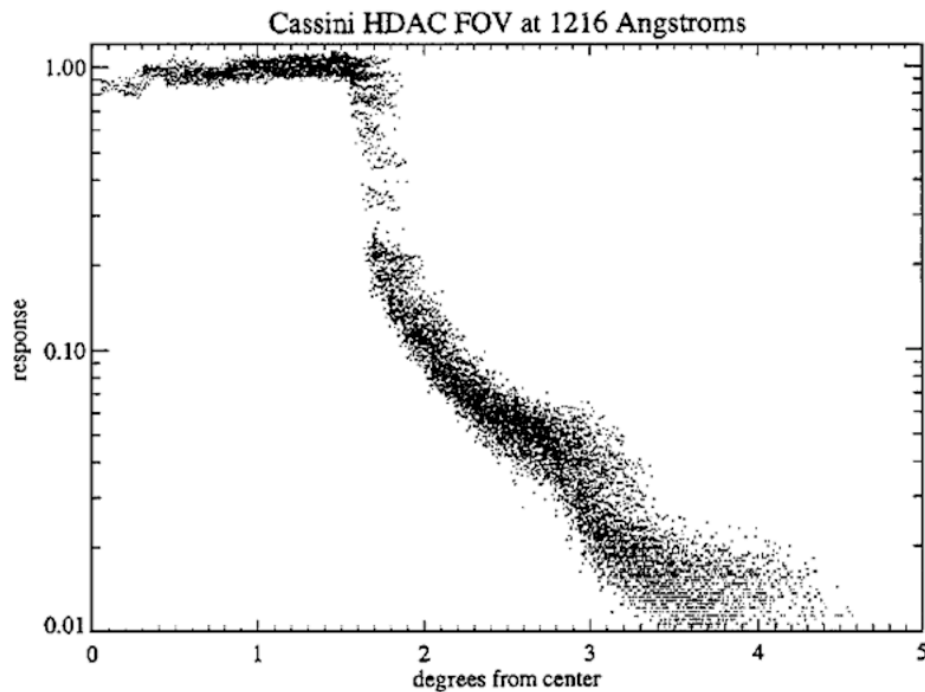
Figure 5.3: Off-axis response of HDAC's circular FOV. Image obtained from Esposito et al. (2004).

5.3.2 Cell optical depths

During the preflight calibrations, the optical depths of both absorption cells were measured as displayed in Table 5.1, showing a significant contamination of the deuterium cell with hydrogen: τ_{HD} is the atomic deuterium optical depth in the H cell and τ_{DH} the atomic hydrogen optical depth in the deuterium cell. The H cell, however, was not contaminated by deuterium.

In-flight calibrations on Jupiter and the local interstellar medium (LISM) as well as performing photometry on bright stars yielded much lower optical depths as shown in Table 5.2. The D cell showed a strong signal excess. Moreover, it was not possible to infer the deuterium optical depth because the objects observed exhibited themselves a very faint D-Lyman-α line due to very low D/H ratios. Nevertheless the atomic hydrogen optical depth in both cells could be determined.

Table 5.1: Preflight calibration of optical depth versus filament power step in the H and D cell, respectively. τ_H and τ_D are the atomic hydrogen and deuterium optical depths in the H and D cell, respectively. τ_{HD} is the atomic deuterium optical depth in the H cell, whereas τ_{DH} is the atomic hydrogen optical depth in the D cell.

Filament voltage step	H cell		D cell	
	τ_H	τ_{HD}	τ_D	τ_{DH}
0	0.0	0.0	0.0	0.0
1	0.0796	0.0	0.3	0.02
2	0.668	0.0	1.5	0.16
3	1.062	0.0	2.8	0.25
4	1.533	0.0	4.5	0.37
5	3.193	0.0	6.2	0.87
6	3.855	0.0	7.5	1.06
7	4.555	0.0	10.0	1.28

Table 5.2: Inflight calibration of the optical depth versus filament step in the H and D cell. It was not possible to determine the deuterium optical depth in the deuterium cells (indicated by "-").

Filament voltage step	H cell		D cell	
	τ_H	τ_{HD}	τ_D	τ_{DH}
0	0.0	0.0	-	0.0
1	0.0024	0.0	-	0.0336
2	0.0468	0.0	-	0.0
3	0.085	0.0	-	0.01639
4	0.1073	0.0	-	0.1118
5	0.4081	0.0	-	0.2401
6	0.6553	0.0	-	0.2241
7	0.8655	0.0	-	0.2239

5.4 Measurements

Since optical depths determined during the afore mentioned in-flight calibrations were lower than in preflight calibrations, the deuterium and hydrogen absorption cells of HDAC are currently operated using a sequence of filament steps, defined by the maximum voltage level (voltage step "7") and cells off (voltage step "0") during the flyby. One sequence consists out of 16 voltage steps.

For the Titan flyby on December 25, 2005 (namely `T9'), a voltage sequence pattern of [0777777777777777] for the H cell and [0707070707070707] for the D cell was used, hence during the first step both cells were switched off and thus enables to detect the background signal. During the flyby, 53 sequences were performed, with a total detector integration time of 9 s per step. The count rate was measured using 72 single integrations for each step, with a duration of 0.125 s (72·0.125 s=9 s).

Analysis of this flyby (Hedelt et al. 2010) has revealed an undersampling problem using the afore-mentioned voltage patterns: Only few measurements in photometer mode where

performed among a large set of measurements where either the H cell or both cells were switched on. This causes the differential signal to result in spikes, especially during FOV changes. In order to compensate for this, more frequent photometer measurements are required, as was done during the flybys on January 28, 2010 (`T66') and April 05, 2010 (T67). The sequence pattern for these flybys were [0707070707070707] for the H cell. The D cell has not been used after the T9 flyby because of the unknown amount of Deuterium in the D cell and the contamination by H. Nevertheless, data analysis using D cell data is encouraged. For the T9 analysis however, the average of measurements one step before and after each measurement in photometer mode was taken to calculate the difference signal. This decreases the number of data points to 52 points throughout the observation, which are still noisy but without spikes caused by undersampling.

5.4.1 Difference signal and background removal

Background signals need to be removed in order to investigate the radiation emitted from Titan. The background signal is an additional signal which can be excluded by taking the difference between measurements performed in photometer mode and when the cells are switched on (I_0 and I, respectively, as given by the equations in section 5.2). Background sources are the radiation from the LISM, the solar radiation and especially at the end of the encounter Saturn, which was in the FOV. The main reason for background signals is the missing oxygen cell, allowing the detection of radiation by the photodetector in a broad wavelength range from 115 nm to 240 nm. Below 115 nm radiation is blocked by the MgF_2 windows. The sensitivity of the instrument above 140 nm is of main importance, since beyond this wavelength the UV output of the sun begins to increase rapidly with increasing wavelength: Data from the Solar Radiation and Climate Experiment (SORCE, Pankratz et al. 2005) show the solar spectrum in the wavelength range, HDAC is sensitive for (see e.g. Figure 5.4).
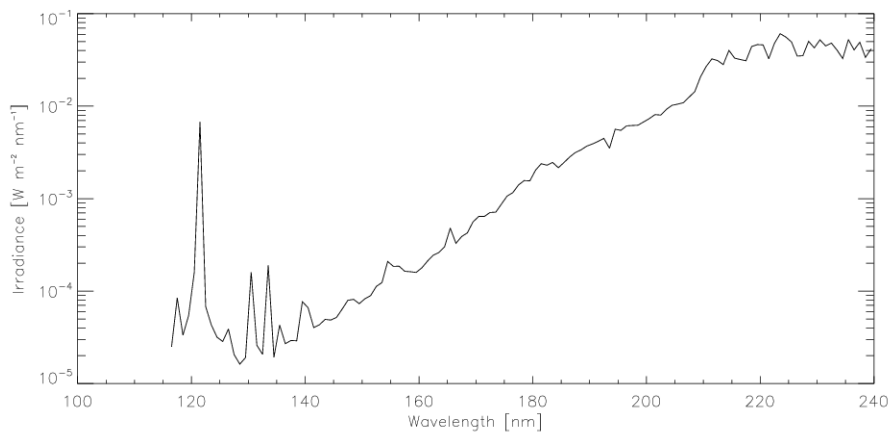

Figure 5.4: Solar spectrum in the wavelength range, HDAC is sensitive for. Note that the irradiance is measured for a solar distance of 1AU. Data obtained from SORCE (http://lasp.colorado.edu/sorce).

5.5 Related publications

Hedelt et al. (2010) has analyzed HDAC data obtained during the Cassini T9 encounter on December 26th, 2005 to determine the atomic hydrogen distribution in Titan's exosphere. During the encounter, the closest approach was achieved at an altitude of 10,410 km.

The measurements performed during the flyby have been modelled by performing Monte Carlo radiative transfer calculations of solar Lyman-α radiation, which is resonantly scattered on atomic hydrogen in Titan's exosphere. Two different atomic hydrogen distribution models have been applied to determine the best fitting density profile. One model is a static model that uses the Chamberlain formalism to calculate the distribution of atomic hydrogen throughout the exosphere, whereas the second model is a particle model, which can also be applied to non-Maxwellian velocity distributions.

The density distributions provided by both models were able to fit the measurements although both models differ at the exobase: Best fitting exobase atomic hydrogen densities of $n_H = (1.5 \pm 0.5) \times 10^4$ cm^{-3} and $n_H = (7 \pm 1) \times 10^4$ cm^{-3} were found using the density distribution provided by both models, respectively. Figure 5.5 shows the measured difference signal between measurements performed in photometer mode and when the H cell was switched on in comparison with the best fitting simulated signal. This is based on the fact that during the encounter, HDAC was sensitive to altitudes above about 3,000 km, hence well above the exobase at about 1,500 km. Above 3,000 km, both models produce densities which are comparable, when taking into account the measurement uncertainty.

Furthermore, a best fitting exospheric temperature of atomic hydrogen in the range of $T_H = (150 - 175) \pm 25$K was obtained when assuming an isothermal exosphere for the calculations. The required exospheric temperature depends on the density distribution chosen. This result is within the temperature range determined by different instruments aboard Cassini.
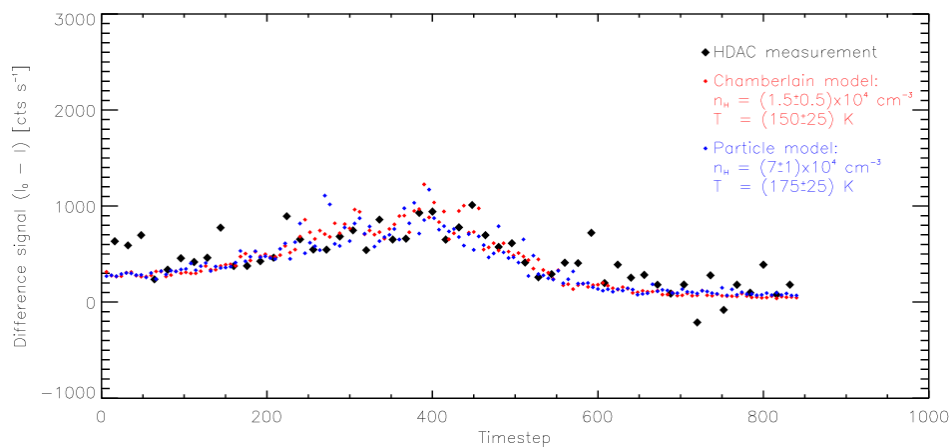

Figure 5.5: Best fit to measured data. Thick black diamonds show the measured difference signal during T9. Small red and blue diamonds show the best model fit, using the Chamberlain model profile and the Particle model profile, respectively.

6. Cassini UVIS Ring and Icy Satellite Stellar Occultation Data

Joshua Colwell

6.1 Introduction

The Cassini UVIS High Speed Photometer is primarily used to probe the structure of Saturn's rings by observing the intensity of starlight from a star as it is occulted by the rings. Occultations of stars by Saturn's moons have also been observed by the HSP and have detected the plume and jets of water vapor emitted from vents on Enceladus. These data are discussed in section 6.4. The raw data consist of a time series of photometric measurements of the star. If the rings are optically thick, less starlight reaches the HSP and the data values are low; conversely, if the ring is optically thin, more starlight reaches the HSP and the data values are correspondingly high. To make use of the HSP ring occultation data and convert the measured signal into a quantity that describes the ring properties, the time series must be transformed to a geometric space in the plane of the rings (that is, the location in ring coordinates of the source of each measured point must be determined). In addition, effects such as changing instrumental sensitivity and background light sources must be taken into account to get a properly calibrated measure of ring optical depth. In this chapter I discuss the geometric and photometric corrections made to convert raw UVIS ring stellar occultation data to a profile of the ring's optical depth as a function of position in the ring plane.

Several papers describe the data, the instrument, ring occultations, and data reduction procedures (Esposito et al. 1998, 2004, 2008, Colwell et al. 2006, 2007, 2009, 2010), and these should be consulted for further information when analyzing UVIS ring occultation data. Much of what is included in this chapter is taken directly from Colwell et al. (2010). In addition to raw data, some occultations have been calibrated, geometrically corrected and delivered to the PDS following the procedures outlined in that paper and in this chapter. These files can be obtained by making an inquiry to the PDS Rings node.

6.2 Observations

The Cassini Ultraviolet Imaging Spectrograph (UVIS) observes stellar occultations by the rings through two channels: the High Speed Photometer (HSP), and the Far Ultraviolet (FUV) spectrograph. The HSP is the primary channel for measuring ring structure because of its fast sampling time of 1 to 8 ms. The sampling time is fixed for the duration of an occultation and was generally selected to be as short as possible within the data volume constraints of the observation time period. The sampling time maps directly to the spatial resolution in the ring plane as the rings move in front of the star. The FUV channel is used for simultaneous measurements of the UV ring spectral reflectance as well as for imaging the star and rings to facilitate determination of background levels in the HSP data. The HSP and FUV have the same spectral bandpass of approximately 110-190 nm (Esposito et al. 2004), while the FUV has 1024 spectral resolution elements and 64 spatial resolution elements along the slit and the HSP is a single detector photometer. A single FUV integration produces much more data than the HSP which is typically operated in a 9-bit compression mode (see below). The FUV is less sensitive than the HSP and cannot be read out as quickly as the HSP, so it is not used for measurements of ring structure.

However, the imaging capabilities of the FUV do allow simultaneous measurements of the ring brightness in the same part of the spectrum that the HSP measures. Due to data rate limitations, the integration period for these simultaneous FUV observations is typically at least 60 s compared to 1-8 ms (usually 1 or 2 ms) for the HSP. (Longer integration periods have been used when observing faint stars and when there were spacecraft data volume limitations.)

The sensitivities of both the FUV and HSP changed in different ways over the course of the mission. The HSP sensitivity declined with the total number of counts accumulated. In time, this is marked by a significant decrease in the summer of 2008 when a series of occultations of the bright star Beta Centaurii occurred. Long baselines of the star were obtained prior to the star passing behind the ring, leading to a large accumulation of counts. This was done in part to address the instrument's "ramp-up" behavior described below and in Colwell et al. (2010). On Cassini Rev 030 (in Cassini parlance, "rev" refers to the number of the revolution of the spacecraft around Saturn; "Rev 030" is not the 30th revolution because the trajectory was modified to insert Revs A, B, and C in place of the original Rev 1 and 2), the total FUV sensitivity to α Vir was ~ 20,000 counts/s compared to over 500,000 counts/s observed in the HSP. For some occultations the FUV data can be used in constructing a model of the background component of the HSP signal (Section 3.3; see also Colwell et al. 2007). Because this process depends on additional models of the instrument response and the azimuthal behavior of ring brightness, we do not use the FUV data in determining the background provided to the Planetary Data System. Where available, scans of the FUV brightness taken simultaneously with ring stellar occultations have been converted to low spatial resolution radial profiles and delivered to the PDS. These scans can be used by the interested user to create a new background model making use of this additional information. This procedure is discussed in detail in Colwell et al. (2007) for one occultation and is summarized in Section 6.3 below.

Each data point recorded by the HSP is referred to as the photon count rate because it represents a number of photons detected during the HSP integration period. The photon count rate, I, measured by the HSP includes light from the star and a background photon count rate, b, and depends on the transparency, T, of the intervening ring material. The background has contributions from interplanetary Lyman-α emission and sunlight reflected off the rings. The latter component of the background is highly sensitive to the occultation viewing geometry and dominates b for observations of the sunlit face of the rings. The interplanetary Lyman-α signal is the dominant source of background when the unlit face of the rings is observed. It, too, varies over the course of the occultation due to the different transparency of the rings at different times in the occultation, allowing more or less interplanetary Lyman-α to shine through the rings. A direct measurement of b is only possible when there is no signal from the star. This is typically only the case when the star is behind the opaque central B ring, though for fainter stars or occultations at low elevation angle above the ring plane, B, the star is not detected at other locations as well. If the measured photon count rate due to the unoccluded star alone is I_0, then the measured photon count rate is given by

$$I = I_0 T + b. \tag{6.1}$$

The count rate due to the unoccluded star, I_0, is measured in regions where $T=1$ and $I=I_0+b$. With the background determined from measurements where $T=0$ and $I=b$, then I_0 can be determined. Tables 6.1 and 6.2 list the locations of regions we use to determine b and I_0.

Table 6.1: Opaque Regions for Background Determination

Number	Inner Radius (km)	Outer Radius (km)

1	100,190	100,210
2	100,260	100,280
3	100,750	100,770
4	101,780	101,800
5	102,090	102,110
6	103,870	103,890
7	104,460	104,480
8	104,860	104,880
9	105,390	105,410
10	106,100	106,150
11	107,870	107,900

Table 6.2: Gap Regions for Determination of I_0

Name	Inner Radius (km)	Outer Radius (km)
D Ring	74,420	74,450
G1	75,760	75,800
Colombo	77,770	77,820
Maxwell	87,360	87,400
Dawes	90,213	90,215
Huygens	117,720	117,760
Herschel	118,200	118,210
Herschel	118,270	118,280
Russell	118,605	118,625
Jeffreys	118,935	118,955
Laplace	119,860	119,950
Barnard	120,310	120,312
Encke	133,500	133,700
Keeler	136,495	136,505
Roche	137,000	137,500

Subsets of the gaps were used to avoid eccentric edges and ringlets within the gaps. Full gap boundaries are in Colwell et al. (2009).

Ignoring stellar variation, I_0 is ideally constant and a single measurement either in a ring gap or outside the rings would be sufficient to determine it for the entire occultation, leaving all the uncertainties in b. While stellar variability is not a significant source of variation or uncertainty in I_0 for any of the UVIS occultations, the HSP unfortunately does not have a constant response to bright signals. This results in variations in the measured value of I_0 over the course of an occultation so that it can only be precisely determined (ignoring for the moment uncertainties in b) in the sparsely spaced gaps in the rings. The nature of the HSP response to bright signals is shown in Figure 6.1.
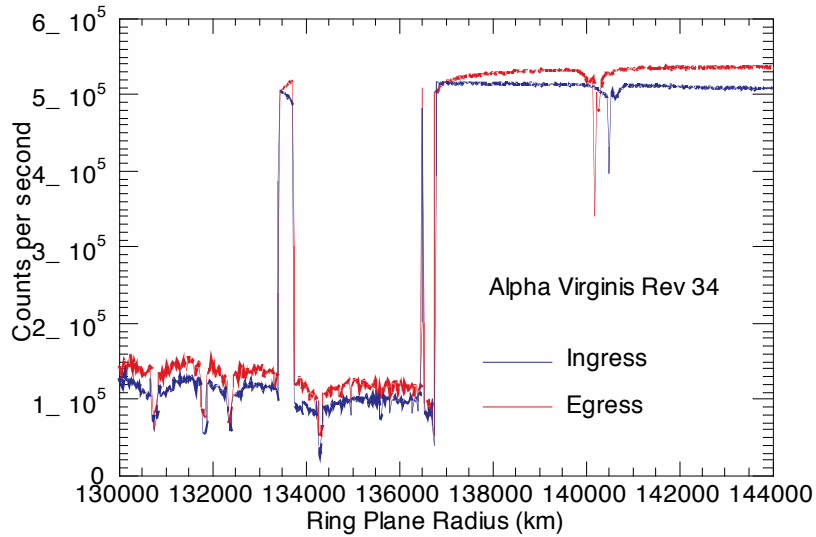
Figure 6.1: Outer A ring region and the F ring in the ingress (blue) and egress (red) portions of a chord occultation of the star α Virginis. The Encke Gap at 133,500 km illustrates the change in instrument response as a function of its history of exposure. The signal is low when it first crosses the Encke gap edge and gradually increases while it is behind the gap. The instrumental response is also responsible for the offset between the ingress and egress light curves in the region beyond the outer edge of the A ring at 136,750 km. The difference in signal in the A ring is not due to instrumental effects: just inside the gap values of I_0 for both ingress and egress are equal so the instrument sensitivity is equal at this location for both ingress and egress. Just interior to the inner edge (where I_0 is observed to be the same) values of I are different, and this must therefore not be due to instrumental effects.

When exposed to a bright star, the photon count rate measured by the HSP increases rapidly for several minutes and then increases more gradually. When the star passes behind a gap in the rings, the photon count rate is initially lower than when the star was last previously observed unocculted and then begins to gradually increase again (see also Colwell et al. 2007). The value of I is different when the star is first occulted by a ring and when it emerges from the ring. Without a validated model of the instrument's non-linear behavior, it is therefore not possible to know what the value of I_0 would be at each point when the star is behind the ring more precisely than the difference in the observed values of I_0 on either side of the ring. At the time of this writing there is no model that correctly predicts the signal, I_0, that would be observed by pointing at a star with no occulting rings in the line of sight. We therefore use a more simple method of linear interpolation between gaps (see below). The estimated value of the star photon count rate, I_0, is used to calculate the slant path optical depth,

$$\tau = \ln(1/T) = \ln\left(\frac{I_0}{\max[I-b, I_{min}]}\right), \tag{6.2}$$

where the denominator is the maximum value of $I-b$ and a selected minimum detectable photon count rate, I_{min}.

Before Eq. (2) can be used, the uncertainties in I and b must be estimated, in part to place a lower detectable limit, I_{min}, on the quantity I-b. In practice, I-b can be negative due to statistical variations in the data and systematic uncertainties in b. Placing a non-zero minimum value on I-b is equivalent to specifying a maximum normal optical depth that can be distinguished from infinite optical depth, τ_{max}. In practice, we determine τ_{max} based on counting statistics as described in Section 3.3 and calculate the normal (perpendicular to the ring plane) optical depth using τ_{max} instead of I_{min}:

$$\tau_n = \min\left[\mu \ln\left(\frac{I_0}{I - b} \right), \tau_{max} \right] \tag{6.3}$$

where $\mu = \sin(B)$, and B is the angle between the ring plane and the line of sight from the spacecraft to the star. The normal optical depth at a particular location in the rings varies with the azimuthal viewing geometry due to self-gravity wakes (elongated, canted clumps of ring particles), so that even occultations of the same star yield different optical depth profiles (e.g. Colwell et al. 2006, 2007). This can be seen, for example, in the difference in the photon count rate between the ingress and egress portions of the α Virginis occultation in the A ring (Figure 6.1).

In addition to the variation in sensitivity of the HSP during a single occultation, the average sensitivity of the detector has been declining with use over the course of the mission. The sensitivy has declined linearly with total accumulated counts, with most of the absolute decline occurring during the high-inclination sequence that concluded the Cassini Prime mission and began the Cassini Equinox mission, from early 2008 through early 2009. Thus, absolute counting rates for individual stars and minimum background values have declined over the course of the mission so that each occultation must be individually calibrated.

6.3. Calibration

In order to generate a full profile of τ_n from the data, profiles of b and I_0 are constructed by linearly interpolating between regions where each value can be measured directly, or by extrapolation. The data are recorded as a time series with a constant integration period. One approach for interpolation and extrapolation of b and I_0 would be to work in the original uniformly-sampled time domain of the data. The approach we adopt is to calculate the location in the ring plane of each data point and then interpolate and extrapolate in the ring plane radius domain. The reason for this choice is that it is variations in the radial structure of the rings that is primarily responsible for variations in b and I_0, rather than temporal variations. We note that this linear model is simplified and that more complex models could be adopted by the interested user to try to better match the non-linear behavior seen in Figure 6.1. The ramp-up instrumental response described in Section 2 and in Colwell et al. (2007, 2010) depends both on time and on the history of the signal into the instrument. For ring occultations, this signal is most strongly dependent on structure in the rings. The first step in our data processing is therefore the calculation of the ring intercept point of each sample in the occultation data.

6.3.1 Calculation of occultation geometry.

The calculation of occultation geometry is described in detail in French et al. (1993), and we follow that general procedure closely. Here we summarize the steps we follow to calculate the occultation intercept points. We get the spacecraft trajectory from SPICE kernels at the Navigation and Ancillary Information Facility (NAIF) of the Planetary Data System (PDS). We

use ephemeris kernels with combined spacecraft and planetary state data based on reconstruction of the spacecraft trajectory by the Cassini navigation team. Stellar coordinates, proper motions, and parallax are taken from the Hipparcos catalog and are propagated forward from the Hipparcos epoch of 1991.25 to the time of the occultation and corrected for parallax to the location of Cassini and for aberration due to motion of Saturn with respect to the solar system barycenter. The ring plane is assumed to be exactly normal to the pole of Saturn which is retrieved from NAIF planetary constants kernels for the time of the occultation. We make a non-iterative correction for general relativity treating Saturn as a sphere. The general relativistic correction is on the order of 10 m or less. The primary uncertainties are in the position of the spacecraft along its trajectory and the pole direction of Saturn. Based on comparisons of different occultation profiles to features that are circular or nearly so (Nicholson et al. 1990, French et al. 1993), these errors are on the order of 1 km. Ring longitudes are referenced to the ascending node of the ring plane on the J2000 inertial X-Y plane.

Users who are not concerned with a very precise geometric solution may avoid the complication of doing the full geometric solution of the occultation by inspecting the raw data for prominent circular (or nearly circular) features in the rings (such as the Encke Gap and other features in Nicholson et al. 1990 and French et al. 1993) and assigning those radial positions to those features, and then doing a spline or other interpolation to get ring radius positions in between those fiduciary features.

6.3.2 Binning the data.

We next bin the data to a uniform radial scale. The raw data typically have radial sampling intervals of several meters to a few tens of meters, though for occultations that cut a chord across the rings, the radial distance between points essentially vanishes at the minumum ring plane radius sampled by the occultation. To facilitate the intercomparison of occultations and the generation of model profiles of b and I_0, we rebin the data to a radial resolution of 1 km. This process can introduce a small error in the number of counts because we are specifying the new bin boundaries to be separated by exactly 1 km, and the boundaries of the raw data measurements in general do not coincide with the new boundaries. When there are 10 or more raw integration periods within the 1 km bins, we sum the points whose boundaries lie closest to the 1 km bin boundaries. If there are fewer points, we perform a linear interpolation between the two points that straddle the bin boundary and divide the counts in the raw data bin that straddles the boundary of the 1 km bin proportionally between the two adjacent 1km bins.

Users who wish to avoid this somewhat complicated binning procedure may simply bin the data by a constant number of points across the occultation (essentially binning in time rather than in ring plane radius). This has the advantage of being quick and simple with the only disadvantage being a varying radial resolution across the resulting occultation profile.

6.3.3 Determination of b and I_0.

We next identify regions where the star is completely occulted to determine the background photon count rate, b. Parts of the B2 and B3 regions of the B ring have shown no transmitted signal in any occultation (Colwell et al. 2009). The regions we use to determine the background are listed in Table 1. Even in these opaque regions there are hints of structure, but the photon count rates there are reasonable estimates of the background. Determination of b in the C and A ring regions requires either additional data or perfect knowledge of I_0 and τ, so we assume a constant value extrapolated from the B ring region. The Titan ringlet in the inner C ring

appears to have narrow opaque regions in the core, interrupted by small-scale (~1 km) structure. Users may opt to simply extend the B ring background value to the inner edge of the rings, or to identify the core of the Titan ringlet (look for data that has Poisson statistics (that is, the mean is equal to the variance) within the ringlet and extrapolate to that value of b in the C ring. It is also possible to determine b in regions outside the B ring with simultaneous measurements of the ring UV reflectance with the FUV channel. Colwell et al. (2007) did this for some occultations in their analysis of self-gravity wakes. Their procedure was to measure the FUV signal as a function of ring plane radius and use that as a guide for the radial dependence of the background photon count rate. The background was then normalized by the measured values in opaque regions of the ring. The measured FUV signal on the rings is a combination of scattered sunlight and Lyman-α transmitted through the rings. FUV data is not available for all occultations, however, and there are complications associated with interpreting FUV data taken during stellar occultations when the star is in the FUV field of view. Some of the star signal gets mislocated onto other rows (see Esposito et al. 1998, 2004 for detailed descriptions of the instrument and its different operational modes). If that signal is attributed to ring or Lyman-α background, then the background signal would be overestimated.

For those occultations that have coincident FUV data we derive a radial profile of the FUV signal at 4000 km radial resolution by removing the data that show the signal from the star. This radial profile is obtained from data taken at different longitudes than the HSP occultation data so the azimuthal asymmetries in ring brightness due to self-gravity wakes (e.g. Colombo et al. 1976, Porco et al. 2008) create additional complications in using the FUV data for the background determination. Because of the complications involved in using FUV data for background determination, mentioned above, and because of the partially subjective nature of adapting the FUV profile to the HSP background model, we do not use the FUV data for our standard model of b. Instead we provide the derived FUV radial profile to the PDS for users who wish to use it to develop their own model of b. Examples of the FUV radial profiles are shown in Figure 6.2. Further information on how the FUV profiles delivered to the PDS were generated is in Colwell et al. (2010).
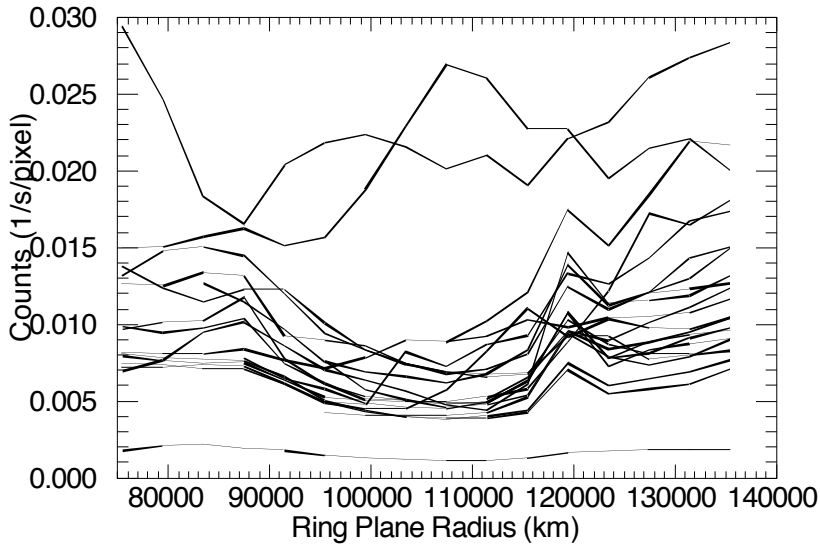
Figure 6.2: Measured FUV signal for several occultations with the signal from detector rows 28-36 (where stellar signal is prominent) removed. The observations shown are primarily for the unlit face of the rings where Lyman-α is the dominant source of background, leading to minimum signal in the opaque B ring and larger signals in the more transparent ring regions. Contamination of the signal from the star is also an issue in those regions due to the instrument's spatial point spread function.

The minimum background in the HSP has been established by a number of observations of the shadowed rings and dark sky (Chambers et al. 2008) as well as observations of VIMS stellar occultations. The HSP count rates in these observations were typically between 100 and 150 counts per second in measurements made in 2004-2005. The signal observed from stars ranges from a few thousand counts per second to several hundred thousand counts per second. In some cases the scattered sunlight background signal can be up to ~10 times higher than the dark sky count rate and can be a significant fraction of the overall signal for faint stars. Although it is not a practical concern because we analyze each occultation independently, it is important to remember that the overall HSP sensitivity is declining with total accumulated exposure such that the background levels observed later in the mission are at lower absolute counting rates than those reported in Chambers et al. (2008) and Colwell et al. (2007).

Our standard procedure for estimating *b* outlined here, based only on opaque regions in the central B ring, likely underestimates *b* elsewhere in the rings because we simply assume a constant value of *b* from the B ring regions to the edges of the ring system. FUV data, where available, and the signal in apparently opaque regions of the Titan ringlet, suggest that the background may roughly double from the central B ring to the inner C ring and to the outer A ring (Figure 6.2). For many occultations the background signal is negligible, and the derived optical depths are insensitive to systematic uncertainties in the background. Drifts in the instrument's sensitivity within an occultation make it difficult to identify broad, low-optical-

Page 58 (7/31/18 - 9:26 AM)

depth features within gaps and also complicate the determination of the appropriate value of the star brightness to use.

The unobstructed stellar photon count rate, I_0, is modeled by taking measurements in transparent regions in the rings where the observed photon count rate is I_0+b and subtracting the modeled background photon count rate. We use linear interpolation between the gaps in the rings, and assume a constant value of I_0 beyond the innermost and outermost gaps. Within some of the broader gaps, notably the Huygens Gap and the Encke Gap, the observed photon count rate changes noticeably due to the changing detector response (e.g. Figure 6.1). We do not model this changing signal within a gap; we use the simpler technique of taking an average gap value and doing linear interpolation between gaps so that the instrumental effect is clear and we do not risk convolving the effects of broad faint rings, known to exist in some gaps, with our modeling of I_0. We use gaps in the A ring, C ring, and Cassini Division, as well as the Roche Division between the A and F rings, and the optically thin outer D ring (exterior to the D73 ringlet), to determine I_0 (Table 6.2). When the nominal geometric solution of an occultation leads to a misalignment of the gap with our nominal ranges, we manually adjust the fit to use only data actually within the gap.

6.3.4 Estimated Maximum Detectable Optical Depth.

The next step is to combine the binned data with the models of both I_0 and b to generate a normal optical depth profile using Equation (3). Whatever binning scheme is used (if any), the model vectors for I_0 and b should have the same number of points as the data vector. Colwell et al. (2010) select τ_{max} to be the largest normal optical depth that has a finite 1-sigma upper error bar ($\tau_{max} = \mu \ln\left[I_0 / \sqrt{I}\right]$), but in practice any finite value can be used for τ_{max} in Equation (6.3). See Colwell et al. (2010) for more discussion of uncertainties in the calculated optical depths. Examples of radial optical depth profiles calculated following the procedure described above at 1 km and 10 km radial resolution are shown in Figures 6.3-6.7.
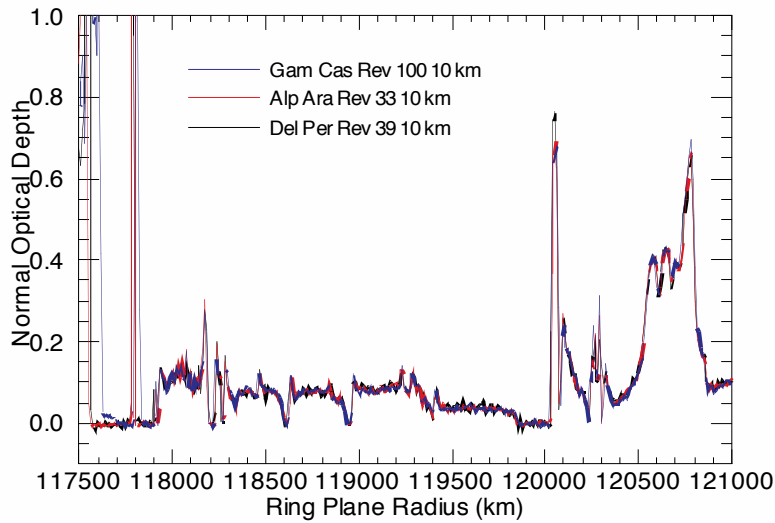
Figure 6.3: Three optical depth profiles of the Cassini Division at 10 km resolution. The optical depth in the Huygens Gap is not uniformly zero in the γ Cas Rev 100 occultation profile due to the instrumental effects described in the text. Each of these three stars is far above the ring plane (*B*>54°) so the effects of self-gravity wakes on the measured optical depth are not noticeable.
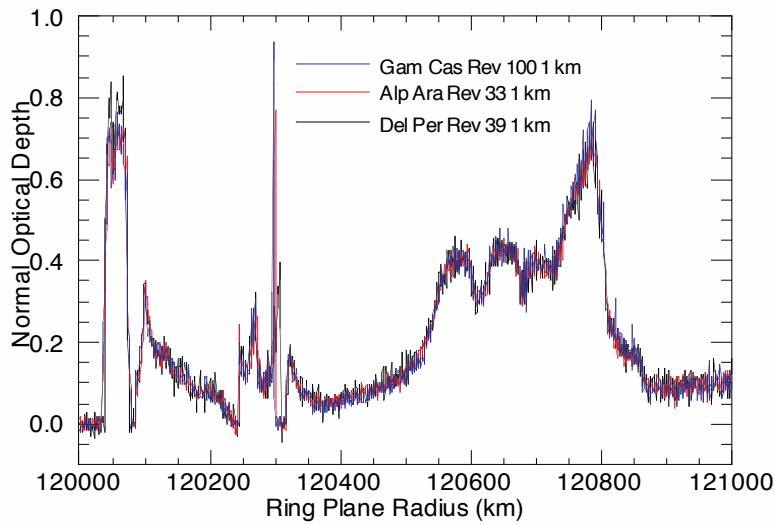

Figure 6.4: Three optical depth profiles of the outer Cassini Division at 1 km resolution from the same occultation profiles shown in Figure 6.3.
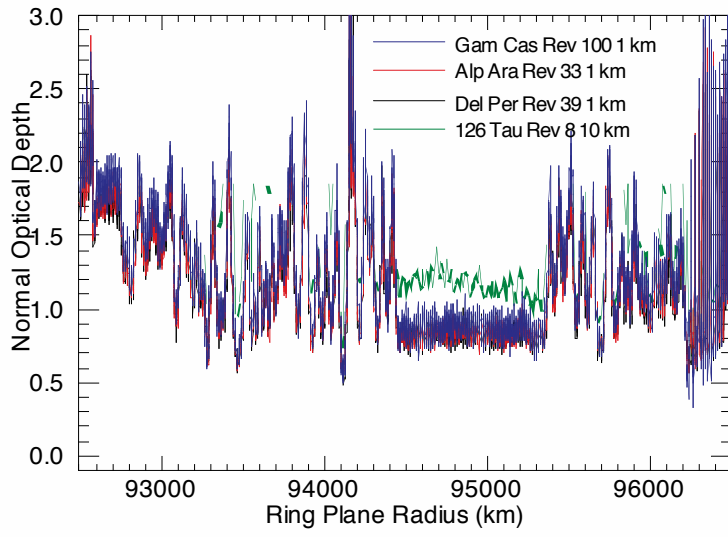
Figure 6.5: Comparison of optical depth profiles in the inner B ring at 1 and 10 km from four different occultations. The star 126 Tauri has B=21.1° so the presence of self-gravity wakes affects the measured optical depth resulting in a noticeable difference between the profile for that star and the other three that are closer to normal incidence (Colwell et al. 2007).
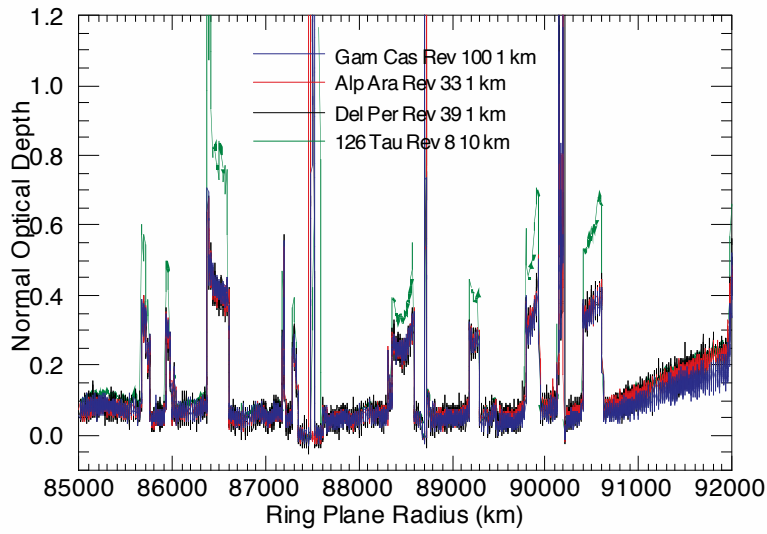
Figure 6.6: Four optical depth profiles of the outer C ring using the same occultations shown in Figure 6.3. The 126 Tauri is shown at 10 km resolution because the star is fainter than the other three. There is a smaller offset in the low-τ regions that may indicate that the background for 126 Tauri is overestimated (see also Colwell et al. 2007 for a detailed discussion of this occultation and its complicated background).
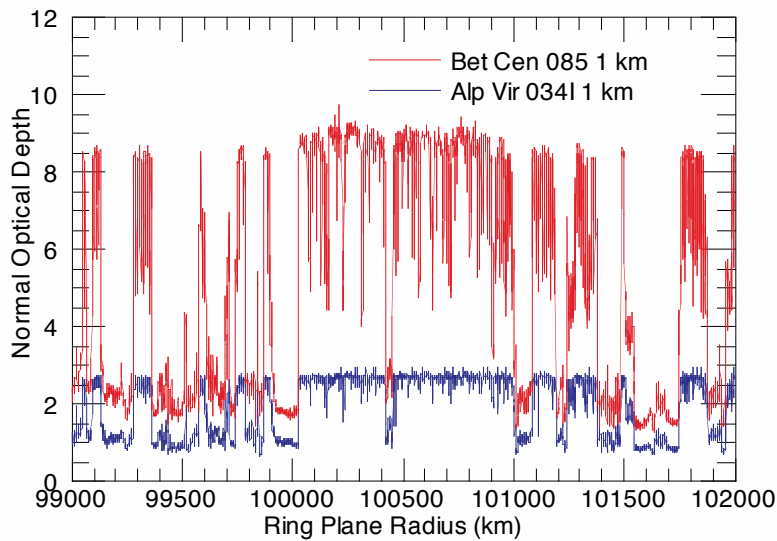
Figure 6.7: Optically thick region of the B ring seen in two occultations at very different incidence angles. The high incidence angle β Centauri occultation is able to measure much larger normal optical depths, and this region of the rings remains opaque at this geometry: $\tau = \tau_{max}$ for both stars over much of this and other regions in the B ring. Where τ is measured, it differs between the two stars due to the effect of self-gravity wakes (Colwell et al. 2007). Some high optical depth structure that is only suggested by the α Virginis occultation shows up at $\tau \sim 5$ in the β Centauri occultation.

6.4 Icy Satellite Occultations

Occultations of stars by Saturn's icy satellites have also been observed and data processing for those measurements is described in this section. The purpose of these observations is to detect and characterize any exosphere, plumes or significant dust concentration in the vicinity of an icy satellite. The observations are called "ICYEXO" and "ICYOCC" in the PDS and utilize the UVIS FUV and HSP channels. Typical FUV integration time is $2 - 5$ sec; the typical HSP integration is 8 msec. FUV data provide a spectral signature of the absorbing gas while the HSP data provide a higher spatial resolution profile of the line-of-sight optical depth of the atmosphere but with no spectral information. Egress HSP data suffers from the instrumental ramp-up issues described above. Since this produces a light curve that is similar to what would be produced by a satellite exosphere, it has not been possible to use egress data to search for tenuous icy satellite atmospheres, though sharp absorptions produced by a locally enhanced concentration of gas or dust would be detectable. The most important results have come from occultations of stars by Enceladus' water vapor plume.

HSP data has been used to detect individual jets within the plume. This is most successful when the occultation is a horizontal cut through the plume, as was the case in 2007. As shown in

Figure 6.8 HSP data is simply summed to 200 msec. At that integration enhanced absorption of the signal corresponds to the jets. The analysis of the Enceladus plume occultations is described in more detail in Hansen et al. (2006, 2008). Because of the short duration of the absorption, a simple linear fit is used to get the baseline stellar signal (plus background), I_0+b, and the line-of-sight optical depth is then obtained simply from equation (6.2). We have assumed that the background is negligible compared to I_0 for these measurements, justified by the high signal of the stars observed (Figure 6.8) compared to typical HSP background rates which are at most ~1000 counts/second when observing the fully illuminated rings. The background from the satellite observations is certainly less than that, which makes b less than 1% of the signal shown in Figure (6.8), for example.

Observations of Enceladus' plume have additionally used data from the EUV and FUV channels. An example of the use of the FUV is given in Chapter 1, example 3. While the analysis steps outlined in Chapter 1 are correct, other factors must be considered. It is best to plot every row to see whether or not the star has moved from one row to another over the course of an occultation. Due to the point-spread-function it may also be best to sum data over multiple rows to capture the entire signal.
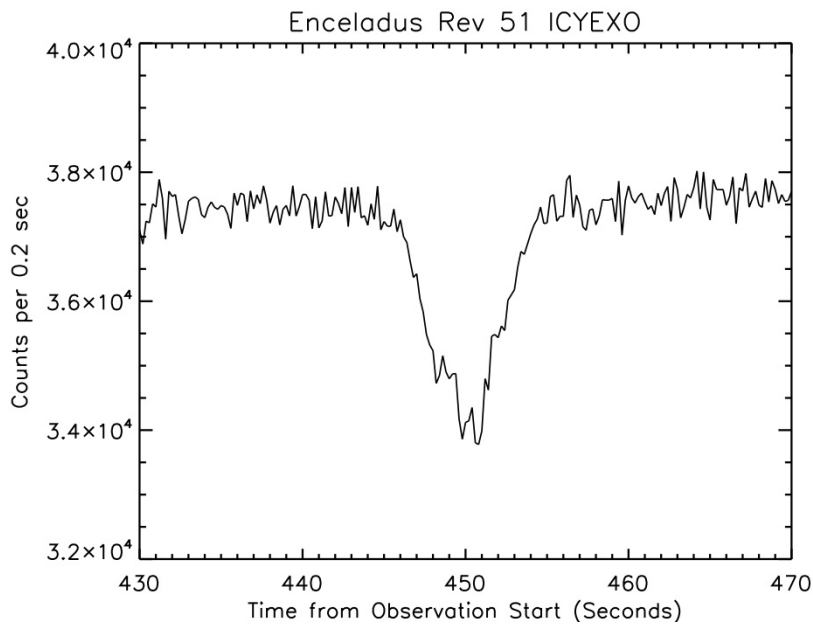

Figure 6.8. HSP data is shown for the time records surrounding the occultation of zeta Orionis by Enceladus' plume (Hansen et al. 2008). Because the occultation was short in duration and the absorption of signal was only at the ~10% level the HSP sensitivity stability is not an issue.

7. Rings Spectroscopy Data Reduction
E. Todd Bradley

7.1 Introduction

This document describes an approach for using the Cassini UVIS spectra for analysis of Saturn's rings. Observations of Saturn's rings with the UVIS began at orbit insertion in 2004 and will continue throughout the extended mission. The majority of rings spectroscopic observations have been configured with the UVIS acting as the secondary instrument; thus the observational geometry and spacecraft slew rate have been driven by other instruments. As of January, 2011 the UVIS had only been the primary instrument one time for making rings spectroscopic measurements. This may not be the case for the extended mission where the UVIS may be used as the primary instrument for ring spectroscopy. Nevertheless, as a secondary rider the UVIS has acquired hundreds of spectroscopic observations of the rings. Observations of the rings by the UVIS for the purpose of ring spectroscopy deals with the instrument collecting solar photons that have irradiated Saturn's rings and either reflected back into the instrument (lit side observations) or have been transmitted through the rings into the instrument (unlit side observations). Typically both EUV and FUV spectra are collected. Table 7.1 lists parameters and typical observational aspects of the rings. For a complete description of the UVIS see Esposito et al, 2004.

Rings spectroscopic data suitable for analysis requires calibration of the raw spectra and then subsequent data reduction that depends on both observational geometry and the needs of the investigator using the data. There is therefore no systematic approach that can be used for all situations. However, data reduction may be broken down into distinct categories and the importance of each determined by the investigator. This document aims to present an overview of the important data reduction categories with the goal of conveying an approach for applying different data reduction steps.

Wavelength range	EUV (56.3-118.2 nm) FUV (111.5-191.2 nm)
Integration time	60 – 600 seconds
Spectral slit	High resolution slit (0.75 mRad) or low resolution slit (1.5 mRad). Most pre-2007 observations are high resolution and most 2007-2010 are low resolution slit
Spectral binning	Either 1 or 2 with the majority of the observations being a 2
Spatial binning	Usually always set to 1
Lit / Unlit side observations	80% lit side
Typical pixel field of view	< 4000 km

Table 7.1. Parameters and observational aspects used for ring observations from orbit insertion through 2010. With the exception of the wavelength range, all of these parameters may be varied. The values listed in this table represent the majority of all observations made so far.

7.2 Calibration of raw spectra

Calibration consists of first subtracting a background from the raw counts. The background arises primarily from detector dark counts introduced by Cassini's three radioisotope thermoelectric generators (RTGs). There are other backgrounds that may or may not contribute to the total raw counts; however the RTG background is internal to the spacecraft and must always be dealt with. The other backgrounds will be discussed in the next section. We then multiply the data by a calibration factor that includes flat fielding and converts raw spectra in counts per integration time to radiance in kilo-Rayleights/Å, where 1 kilo-Rayleigh = 10^9 photons sec^{-1} cm^{-2} emitted over 4π steradians. Details of the UVIS instrument and calibration are given in Chapters 3 and 4. Figure 7.1 shows typical radiance from the B ring on the lit side. Lyman- α is clearly present as well as the solar continuum. This data was acquired using a spectral binning of 2 with the low resolution slit. Software developed by the UVIS team is publicly available that will convert raw data downloaded from the PDS to calibrated data. This software, called Cube Generator, is described in Chapter 12.
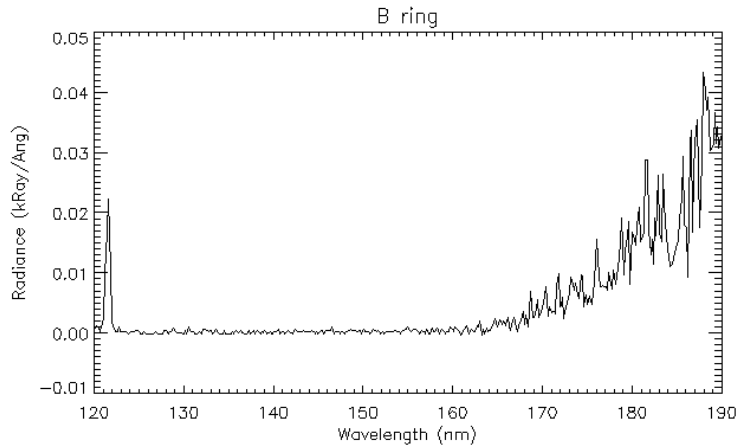

Figure 7.1 An example of radiance from the B ring measured from the lit side of the rings. Lyman- α is clearly present. The spectra longward of 160 nm is due to solar irradiance reflecting from the rings.

7.3 Data reduction

This section describes other data reduction steps that may be taken depending on the observational geometry and the needs of the investigator. Most of these steps depend on observing geometry, which may be determined using Cube Generator that is described in Chapter 12. Investigators are strongly encouraged to look at the geometrical configuration of observations being used for analysis. Special attention should be given to the location and size of pixels projected onto the ring plane and the angle of the line of sight with respect to the dayside of the planet. The importance of these provisions is explained in the following subsections.

7.3.1 Saturn shine

Solar irradiance reflected from the atmosphere of Saturn may contribute to the signal by either reflecting off of Saturn's rings and entering into the instrument or by entering the instrument when the Saturn-spacecraft-boresight angle is sufficiently small, also known as off-axis light. The magnitude of Saturn shine varies on a number of factors. Presumably the peak Saturn shine reflected from the rings is for regions extending radially outward from local noon, with the magnitude decreasing for both increasing ring plane radius and solar hour angles away from local noon. Similarly off-axis light peaks for small off-axis angles on the dayside hemisphere and decreases for both increasing off-axis angle and observations away from local noon. Furthermore, Saturn shine that reflects off of the rings and into the instrument is spectrally modified by the reflectance properties of Saturn's rings whereas off-axis light presumably bears the same spectral shape as that of Saturn's atmosphere. An expression for the reflectance of the rings with both cases of Saturn shine included may be written as:

$$I = aF_{Sun}\,r \; + \; bF_{Sat}\,r \; + \; cF_{Sat}$$

$$r = \frac{I - cF_{Sat}}{aF_{Sun} + bF_{Sat}}$$

(7.1)

where F_{sun} is the flux from the Sun divided by π, F_{Sat} is the flux from Saturn's atmosphere divided by π, and a, b, and c are constants. The first term on the right is due to solar radiation being reflected/transmitted after only interacting with the rings, the second term on the right is due to solar radiation first reflected off of Saturn's atmosphere and then reflecting from the rings into the instrument, and the last term on the right is due to solar radiation reflecting from Saturn's atmosphere and then into the instrument. Figure 7.2 shows the radiance measured from Saturn's atmosphere for observations that looked directly at the atmosphere. This corresponds to F_{Sat} given in Equation 7.1. For non-negligible Saturn shine analysis code will have to be written to solve for the constants in Equation 1. There may be situations where Saturn shine reflected from the rings is negligible or off-axis light is negligible; in which case the constants b and c, respectively, will be zero.
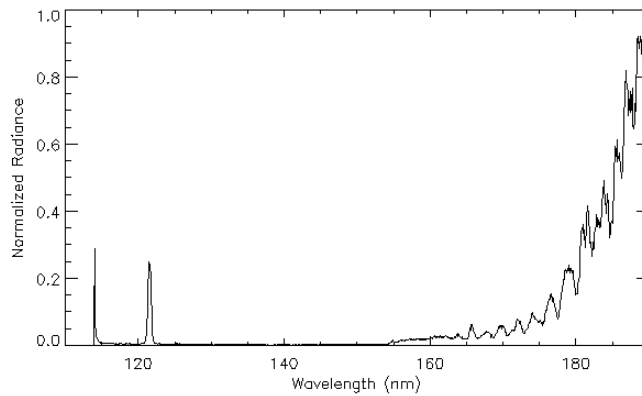
Figure 7.2. Normalized radiance measured from Saturn's atmosphere. For small off-axis angles above the dayside this spectra may contribute to the total signal from the UVIS for rings observations. Also, for observations of the rings near local noon, a radiance such as this may reflect from the rings and contribute to the measured radiance from the instrument.

7.3.2 Skewed field of view

The optical system of the FUV and EUV channels images an extended source to an entrance slit and is then spectrally dispersed onto a 64 spatial X 1024 spectral detector, where the spatial direction is co-aligned along the length of the slit. The projected size of a pixel is ~ 1 mrad in the direction along the length of the slit and 0.75 mrad or 1.5 mrad in the cross slit direction for either the high resolution or low resolution slit, respectively. Depending on the position and orientation of the spacecraft with respect to the ring plane, the shape of a pixel may be either rectangular or non-rectangular when projected onto the ring plane. Furthermore, the relative motion between the spacecraft and ring plane during an integration period results in the projected field of view being different than the instantaneous field of view. Figure 7.3 shows the projected field of view of a pixel at the initial, middle, and final times for a three hundred second integration period. The pixel begins in the outer B ring and moves into the Cassini Division. Thus the data for that pixel has contributions from both rings regions. This complicates analysis of ring observations and has led to procedures for binning the data and interpolating to evenly spaced grids as will be discussed in the next section.
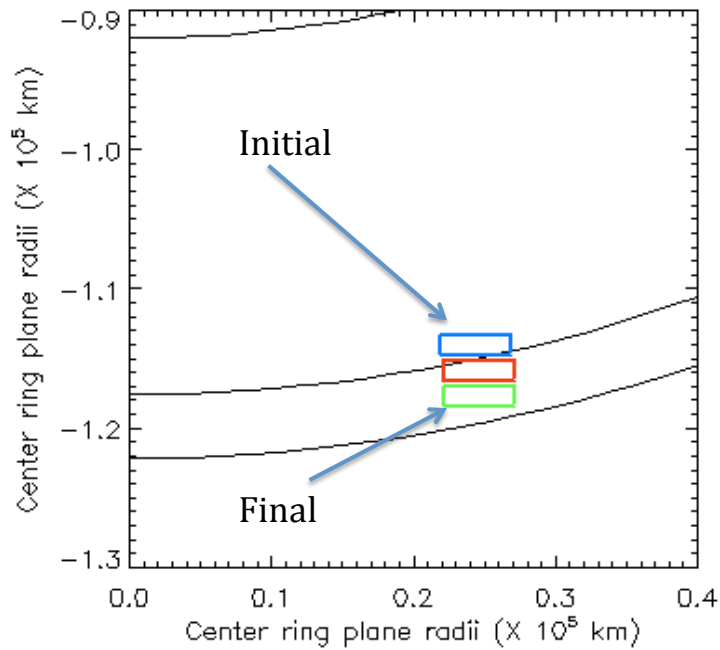
Figure 7.3. The projected pixel begins in the outer B ring and drifts into the Cassini Division. Contributions to the signal arise from both the outer B ring and the Cassini Division. Cube generator (Chapter 12) now returns the coordinates of the corner of the pixel at the initial, middle, and final integration period

7.3.3 Binning the data

During an observation the field of view of a pixel projected onto the ring plane is affected by the spacecraft motion and the angle and orientation at which the line of sight intersects the ring plane. This results in pixels that are non-uniform both in size and distribution in the ring plane. Azimuthally binning pixels within relatively large radial bins may bias the result towards regions within bins where there is a higher concentration of pixels. Figure 7.4 shows how pixels may be unevenly distributed within a ten thousand km radial bin in the outer B ring, denoted by the heavy lines. In this simple example there are two pixels that lie at the outer edge of the radial bin with other pixels overlapping one another radially for decreasing radius. Simply averaging the spectra from all of the pixels within the ten thousand km radial bin will weight the average towards the outer most portion of the radial bin since there are more pixels in the outer region of the bin than in the inner region. However, notice that there are pixels outside of the radial bin on both sides, which allows for a technique to deal with uneven sampling of the rings. An example is taken from Bradley et al (2010) for resampling the data into an evenly spaced grid. In anticipation of data being azimuthally binned over some radial increment, we only consider the radial direction when resampling the data. We divide the rings into a 100 km radial grid and for each grid element, we select all pixels that intersect that element. The size of the pixels takes into account the skewed pixel size as described in Section 7.3.2.
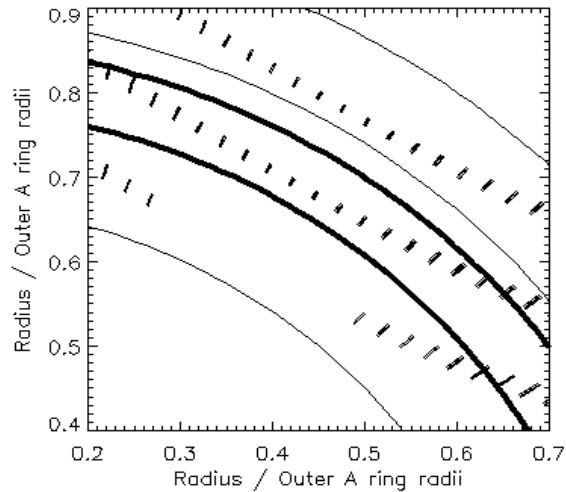
Figure 7.4. Field of view for pixels projected onto the ring plane. The thick lines represent a 10,000 km radial bin in the outer B ring. The non-uniform sampling is apparent since the outer portion of the radial bin contains more pixels than the inner region resulting in an average weighted towards the outer B ring.

The fraction, f, of each pixel within the element is multiplied by the value of I/F for that pixel and summed according to

$$f_i = \frac{100}{R_i}$$

$$I/F(resampled) = \frac{\sum_{i=1}^{n}(I/F)_i * f_i}{\sum_{i=1}^{n}f_i} \qquad (7.2)$$

where R_i is the length of the ith smeared pixel in the radial direction and n is the total number of pixels for which some fraction falls within the grid element, I is the radiance of the signal, and πF is the solar flux, this F is the solar flux divided by π. For this example all of the pixels were larger than 100 km so that none of the pixels fit completely within an element. The result is an evenly weighted radial distribution of I/F values in 100 km increments. For other data with different projected pixel sizes a value different than 100 may need to be used. After the data were evenly gridded, we then binned the results in larger radial increments to improve the signal-to-noise ratio.

7.3.4 Lyman- α scattering

The Lyman-α spectral line occurs at 121.6 nm and depending on the magnitude may produce scattered counts at other spectral pixels. This is due to both the instrument point spread function and to grating scatter. However, the reflectance of the rings is such that this is typically not a problem for ring observations except for spectral regions very close to line center of Lyman-α. Figure 7.5 shows the radiance for an observation of the B ring within the shadow of the planet. Lyman-α is clearly present; however any photons from Lyman-α that make it to longer wavelength pixels are clearly negligible except for pixels less than 1 nm from line center. The increase in the noise for wavelengths longer than 165 nm is due to decreasing sensitivity of the detector for those wavelengths. If the goal of the investigator is to measure Lyman-α reflectance from the rings, then the radiance over the entire broadened spectral line must be summed and multiplied by the bandpass of the instrument. This is the same as numerically integrating a spectral line that has been broadened due to spectral point spreading where the radiance is the dependent variable and the bandpass is a finite increment of the independent variable in wavelength space.
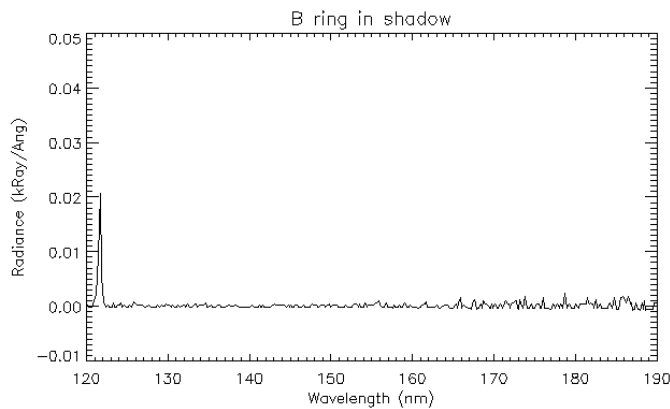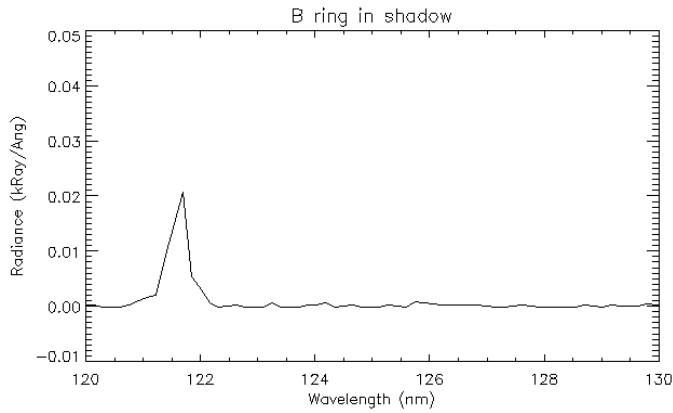
Figure 7.5 Radiance from an observation of the B ring while in Saturn's shadow. The upper panel shows the full spectral extent of the FUV channel while the lower panel shows only the spectra from 120-130 nm. Lyman-α scattering at longer wavelength pixels is negligible except for wavelengths less than 1 nm from line center. If the goal of an investigator is to measure Lyman-α reflectance from the rings, then the radiance over the entire broadened spectral line must be summed and multiplied by the bandpass of the instrument.

7.3.5 Long wavelength photon scattering into short wavelength spectral pixels

Saturn's rings are brighter at wavelengths longer than the water ice absorption edge at ~ 165 nm, where water ice is highly absorbing at wavelengths lower than 165 nm. Some photons from wavelengths longer than 165 nm scatter into the short wavelength spectral pixels resulting in an increased background. Figure 7.6 shows spectra from the B ring from an observation where there is a background at short wavelength pixels. This background is the sum of RTG counts and long wavelength photons that were scattered into the short wavelength pixels. Therefore one possible technique for background subtraction is to average the raw counts from pixels at wavelengths shorter than Lyman-alpha, red squares, and subtract this from the raw counts. This technique will result in subtracting RTG counts and any long wavelength photons that were scattered into short wavelength pixels, with the assumption that on average the same number of long wavelength photons scatter into each pixel.
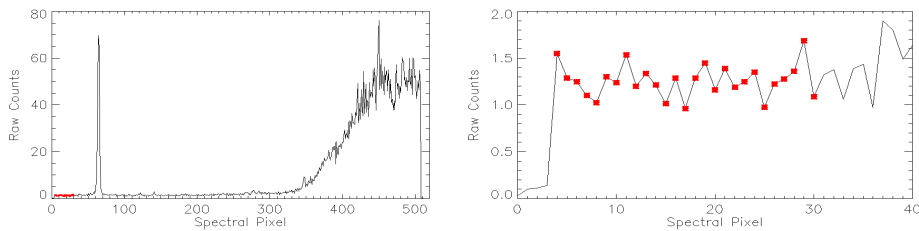

Figure 7.6 Raw spectra from the B ring showing a background at short wavelength pixels. The right panel is a magnified view of the short wavelength region from the left panel. The large peak near spectral pixel 65 is Lyman-alpha.

Page 72 (7/31/18 - 9:26 AM)

Using this technique Figure 7.7 shows a comparison between I/F for the same observation but for different background subtractions from the raw spectra before the calibration factor is applied. In one case only RTG counts are subtracted from the raw counts and for the other case the average of 27 spectral pixels at wavelengths shorter than Lyman-alpha was used as the background, resulting in lower I/F values at shorter wavelengths. Note that the latter background subtraction includes long wavelength photons scattered into short wavelength pixels and RTG counts.
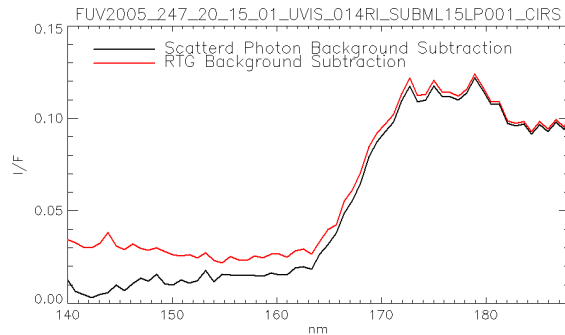

Figure 7.7 I/F computed where two different backgrounds were subtracted from the raw spectra.

7.4 Conversion to I/F

Often it is desired to convert radiance to I/F. The solar flux (πF) at the time of the observation is divided by μo to get the radiance of a perfect Lambert surface and the observed radiance is then divided by that to produce I/F. Due to solar variability, the solar flux measured from Earth orbiting spacecraft must be adjusted to the time the observation was made at Saturn. Thus the side of the Sun that was facing Saturn at the time of the observation is the desired side observed by the Earth orbiting spacecraft. Furthermore, the observed solar flux from Earth orbit must be divided by the square of the Sun-Saturn distance at the time of the observation. A solar continuum should also be smoothed to the bandpass of the instrument using the instrument point spread function.

7.5 Summary

This chapter is an overview of the steps that should be considered to take Saturn rings spectra from the PDS and turn it into a useful data set for analysis. The details of Saturn shine have been explained with a plot of a spectra of Saturn's atmosphere taken with the FUV channel of the UVIS. Equation 1 presents a possible method for dealing with Saturn shine. The investigator is encouraged to look at the observational geometry for any observation being used for analysis to gain insight into the relative contributions of Saturn shine reflected from the rings and off-axis light. A procedure has been given for dealing with unevenly spaced data points that accounts for pixel skewing due to spacecraft motion with respect to the ring plane. This procedure was taken from Bradley et al (2009) and serves only as a representative example. Lyman-α scattering has been shown to be negligible except for spectral regions less than 1 nm

from Lyman-α line center. If the total radiance of Lyman-α is desired then the radiance from the broadened Lyman-α line must be summed and multiplied by the bandpass.

8. Reflectance Spectroscopy of Icy Moons and Saturn

Amanda Hendrix, Candice Hansen, Robert West

UVIS observations of Saturn and her icy moons are used to derive reflectance spectra as well as images.   The techniques are similar for Saturn and for the moons. The satellite surface compositions are dominated by the presence of water ice that has a strong absorption edge near 165 nm. Mapping the strength and location of this absorption edge allows the UVIS data to be used in determining water ice concentrations and grain sizes, as well as probing non-water ice constituents.

The types of UVIS icy satellite observations and their instrument setups are shown in Table 8.1. In determining icy satellite surface reflectances, the primary observations are the ICYLONs and ICYMAPs, so we focus here on those data, from the FUV channel. ICYLON observations have historically had the focus of building up phase angle and longitudinal coverage of the moons. ICYMAP observations have generally been used for close-in observations during close flybys. The number of rows returned in each observation depends on the data volume available; this varied from observation to observation. ICYEXO analysis is discussed in Chapter 6.

Table 8.1. UVIS Icy Satellite Instrument Configurations

	Slit	integration time	Channels	Use
ICYLON	Low res (1.5 mrad)	120 sec	FUV, EUV	Longitudinal and phase coverage
ICYMAP	High res (0.75 mrad)	30 sec	FUV, EUV	Close flyby coverage
ICYSTARE	Low res (1.5 mrad)	120 sec	FUV, EUV	Distant observations
ICYECL	Low res (1.5 mrad)	120 sec	FUV, EUV	Distant eclipse observations
ICYPLU	Low res (1.5 mrad)	180 sec	FUV, EUV	Plume observations
ICYEXO, ICYOCC	Low res (1.5 mrad)	5 sec	FUV, HSP	Stellar occultations (see section 6.4 for analysis steps)
LOPHASE	Low res (1.5 mrad)	120 sec	FUV, EUV	Longitudinal and phase coverage

The treatment of UVIS observations of the reflectances of the icy Saturnian moons can be distributed generally into two broad areas, depending on whether the observation is disk-resolved or whole-disk. If the body is distant enough that it is sub-pixel (i.e., smaller than the width of the slit, usually 1.5 mrad), so UVIS sees the whole-disk (Figure 8.1), then it is a "stare" type observation, where the optical remote sensing (ORS) slits are held steady on the body for the duration of the observation. For these observations, if a pointing vector other than UVIS_FUV was used, then the body is not centered in the UVIS slit. In this case, the body may or may not be entirely within the UVIS slit; sometimes the body is only partly within the slit, making the observation of limited value in terms of deriving surface reflectance. If the body is close enough

that it is larger than the width of the UVIS slit, it is a disk-resolved observation (Figure 8.2) and there may have been a scan performed across the body, or a mosaic (usually an ISS rider observation), where the slit is positioned in particular locations throughout the observation. Nearly all stare observations are in the ICYLON class. Scans and mosaics may be ICYMAP (usually very close) or ICYLON. LOPHASE observations are distant, disk-integrated observations that use the ICYLON instrument setup while covering particularly low phase angles.

The UVIS instrument measures spectral radiance (units of kR/Å) in each spatial row (1 kR is equal to $10^9/4\pi$ ph/s/cm^2/str). The reflectance is defined as

$$r = I/F = P/(S/\pi) \tag{8.1}$$

where P is the calibrated signal from the body with background subtracted, in kR/Å. The solar flux is denoted by S, where $S = \pi F$.
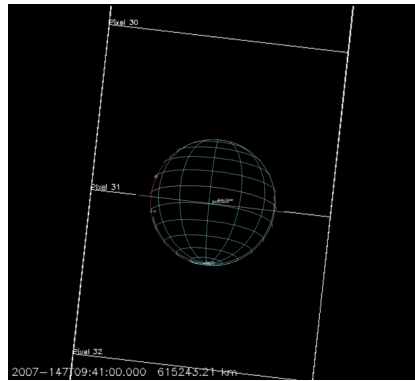
Figure 8.1. Example of a disk-integrated observation; Enceladus is sub-pixel (0.8 mrad).

If the body is sub-pixel, we must carefully determine the filling factor, the percentage of the pixel filled by the body. This involves using reconstructed kernels to get the distance to the body. The filling factor is

$$FF = \text{body size/pixel size} \tag{8.2}$$

where the body radius is used to determine its size and the pixel size is projected onto the sky at the distance of the body. We divide Eq. (8.1) by the filling factor (Eq. 8.2) to determine the whole-disk reflectance.

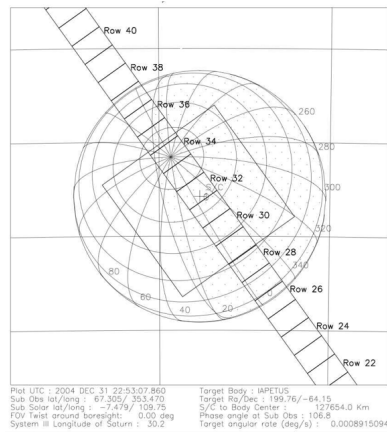Figure 8.2. Example of a disk-resolved observation where UVIS was staring at (rather than scanning across) Iapetus. The UVIS low-resolution slit is shown, along with the ISS narrow angle camera (NAC).

The calibration step can be performed before or after background subtraction and involves the use of IDL routines "feuv_reader" to open and read the data files and "Get_FUV_2013_Lab_Calibration" to generate the calibration array for the date of the observation. These routines are available on the PDS. The reader is referred to Chapter 4 for additional information on reading and calibrating UVIS data files.

8.1 Background subtraction

The measured spectrum includes not only the reflected solar signal from a satellite's surface, but background sources such as RTG noise and interplanetary Ly-α. We must subtract out this background signal before dividing by the solar spectrum when determining the reflectance spectrum. For a background spectrum we use (when possible) a night side spectrum obtained during the same time period as the dayside spectrum. It is not always possible to use a night side spectrum, so often we use an off-body spectrum. A night side spectrum is preferable so that we can obtain a reflectance value at Ly-α. Because the dark-sky Ly-α signal is higher than the reflectance from the surfaces of the icy moons, we cannot subtract off the background and obtain a reasonable Ly-α albedo. The nightside signal includes RTG noise as well as reflected Saturn system Ly-α. The contribution from interplanetary Ly-α, to both the day and night sides, is negligible compared to solar Ly-α. Thus the only difference between the day and night signals is the reflected solar spectrum. Figure 8.3a shows a background spectrum displayed along with Phoebe's reflected solar spectrum; even at the shorter wavelengths where the signal is low, the Phoebe signal is above the background level in this observation. For the nightside data, we looped through the data and chose rows/times when the incidence angle was greater than 100 deg.
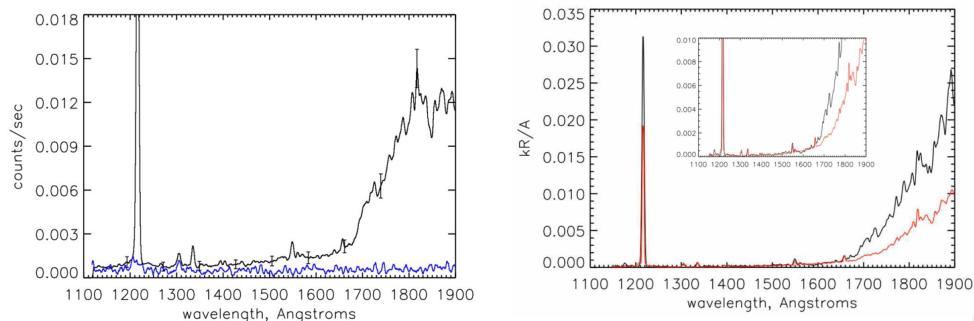
Figure 8.3. Sample spectra from Phoebe (phase angle = 42°). (left) Average raw spectrum (counts/s) from the dayside (average of 1224 spectra) and nightside background spectrum (in blue), with sample statistical error bars shown. (right) Average calibrated spectrum (kR/Å), nightside background subtracted, with scaled solar spectrum overplotted (in red). The solar spectrum has been scaled by fitting to the reflected 1335 Å C II feature in the Phoebe spectrum.

8.2 Solar spectrum division

We use the solar data as measured by SOLSTICE on the SORCE spacecraft (McClintock et al., 2000), scaled to the heliocentric distance of Saturn on the day of the observation, making sure to use the solar spectrum for the sub-solar longitude appropriate for the UVIS observation. (We use the solar spectrum measured at Earth but adjusted forward or backward in time to account for the difference between the sub-solar longitudes facing Earth and facing Saturn on the day of the observation.) See Figure 8.3b for a sample Phoebe spectrum compared with a scaled solar spectrum. The solar flux decreases dramatically below ~1500 Å, and in addition, the reflectance of water ice is very dark at wavelengths <1650 Å. The combination of these two effects means that the icy moons generally do not reflect very much light at the shorter FUV wavelengths, and as a result, the signal is extremely low. The resultant reflectance continuum is noisy, so we often choose to create binned reflectance values at the wavelengths where the satellite spectrum exhibits reflected solar lines such as the carbon line at 1335 Å (see for instance Figure 8.4a). Figure 8.4b is an example reflectance spectrum showing division by the solar continuum.
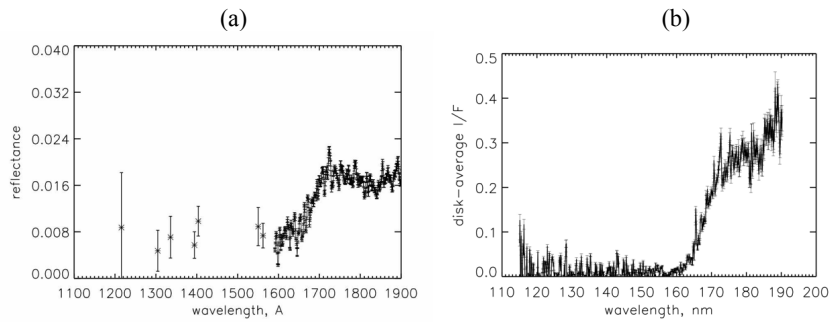
Figure 8.4. Sample reflectance spectra. (a) Phoebe (phase angle α=42°). (b) Enceladus (α=2°).

8.3. Saturn reflectance spectra

The goals and methods for Saturn science are similar to those for the icy satellites. The reflected intensity (I/F) contains information on a few hydrocarbons (principally acetylene) and the scattering and absorbing properties of haze. Most of the Saturn data obtained with UVIS as the prime instrument are named EUVFUV in the observation ID. These are image cubes, where the slit was scanned across the disk of Saturn resulting in two spatial dimensions and one spectral dimension. The scan stops at many places to allow other instruments to image, then continues to build up a complete image. Viewing and lighting geometry information is needed to interpret the data. The required geometry consists of view and emission angles of the outgoing and incoming photons relative to the local zenith direction, and the phase angle (angle between incoming and outgoing rays). The following list is an example of step-by-step instructions for a user wishing to calibrate the UVIS data and obtain the geometry needed to interpret the data.

1   Download new EUVFUV (or other data) files from the data repository.
2. Create a list of file names if there are multiple files in a data set. This is just a text file with a list of all the file names going into the cube program.
3. Download applicable SPICE kernels, corresponding to the days of the observations, from the Cassini NAIF kernel repository (see ftp://naif.jpl.nasa.gov/pub/naif/pds/data/co-s_j_e_v-spice-6-v1.0/cosp_1000/aareadme.htm and http://starbrite.jpl.nasa.gov/pds/viewDataset.jsp?dsid=CO-S%2FJ%2FE%2FV-SPICE-6-V1.0)

4. Compile (currently IDL) and then run cube_generator.pro (see Chapter 12) (substitute your own directory pointers – the following are examples)
    -   Input files and input batch files are located in the directory /dst/SaturnFUV/RawData/ or /dst/TitanFUV/RawData/.
    -   Output should be the default, "improved" output file format. Save the output file in the folder /CalibratedData/ found either in /dst/SaturnFUV/ or /dst/TitanFUV. The filename must match the syntax of the files already in those folders.

- Use 'LT' aberration
- Check RTG correction (and use default value of 0.0004 counts/second/pixel)
- Select "Saturn" for target body.
- Use the default "full calibration and flatfielding sequence).
- Kernels and kernel batch files are located in the folder /Kernels/.
- Once all the above is entered, click "Create." Note that for some datasets, correct kernels still generate a kernel error because of holes in the kernels. If an error is encountered, check to see that "loaded kernels" all match date of observation, then check "override kernel checks" and click "Create" again.

5.   Calibrate to I/F by division by a solar spectrum as described above. Alternately one can run a 'forward calculation' as described elsewhere in this document (see Chapter 10) to estimate instrument count rates given a model intensity spectrum, and compare the simulated counts with observed counts.
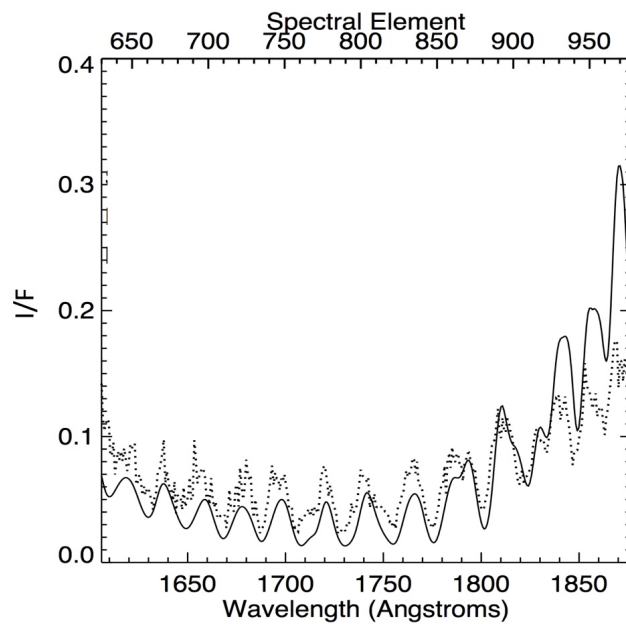
Figure 8.5. Sample Saturn spectrum. I is the measured intensity; πF is the incidence solar flux.

9. Stellar calibration of the UVIS FUV channel

Donald E. Shemansky

9.1. Introduction

The UVIS fuv channel has been calibrated on an absolute scale using observations of αVir. A model of the stellar spectrum is used in the analysis to accurately account for instrument properties. The absolute scale is fixed by calibrating the αVir spectrum against the observations obtained using the Copernicus and IUE (*Cp-IUE*) spectrographs as benchmark references. It has been found that the laboratory based calibration of UVIS FUV agrees with the absolute scale established by *Cp-IUE* in the mid wavelength range 1300 - 1500 Å. The results of the analysis shows a variable sensitivity for UVIS fuv in the long wavelength region as a function of time in the mission. The overall sense of the change at longer wavelengths is toward higher sensitivity as time progresses. The magnitude of the change is an order of magnitude at 1900 Å. In the cases where the star calibrations cover all of the spatial pixels a flatfield is established. The flatfields calculated here are preliminary and will require corrections in a few particular locations in the spectrum where narrow spectral features in the stellar spectrum are not accurately modeled. Only a few of the available αVir stellar calibration sequences have been reduced with the methodology applied here, but the full set of available observations can be reduced without a large expenditure of effort based on the present experience. The results obtained in this chapter indicate that the understanding of the physics of scattered solar radiation by aerosols and surface reflection will be significantly changed through the use of the spectral sensitivity curves provided in this report. This investigation was undertaken after finding that theoretical aerosol scattering properties could not be reconciled with observed UVIS fuv spectra.

The calibration curves developed in this chapter differ from those described in Chapter 3 because we use here a forward modeling approach. Our analysis and data reduction use forward modeling for the purpose of accurately accounting for the effects of the instrument point spread function (psf). The calibration data submitted to the PDS are described in Chapter 3, and account for temporal changes in sensitivity. Differences in the sensitivity curves presented in this chapter and those in the PDS are caused by psf effects, differences in flatfield, and in particular locations in the spectrum. The flatfields developed here are designed to operate on prefiltered data vectors. Comparison of the impact of these different methodologies have not been investigated in detail, but will be examined in the future as a means of determining limitation in accuracy of reduction processes. The data treatment described in this chapter is designed for detailed spectral modeling and application to the construction of image cubes from UVIS system scan observations that use the entire slit in accumulating virtual images.

Future deeper exposures with multiple scans of αVir will be conducted once per year to provide updated accurate flatfields. The current standard starcals are adequate for determining the time dependent spectral sensitivity.

9.2. Stellar model and the absolute flux reference

The αVir of model emission properties at the surface of the star have been obtained from the detailed non-LTE (nLTE) blanketed calculations by R. Kurucz and J. Aufdenberg. The model parameters have been determined here by testing a range of blackbody temperatures underlying the nLTE blanket in order to fit the *Cp-IUE* observed spectra. The LISM extinction properties have been roughly approximated in order to provide an accurate fit to the *Cp-IUE* spectra > 1150 Å. The LISM properties should be refined to provide an accurate model at shorter wavelengths. Our nominal stellar model at the observing instrument that conforms to the *Cp-IUE* spectra falls within the uncertainties in visible-infrared measurements of surface temperature, stellar radius, and distance to the star. αVir is a binary and both components are included in the present model, although the smaller companion has only a small effect. The stellar parameters are given in Table 9.1. The Copernicus spectrum is obtained from Code et al.(1979) (see Herbison-Evans et al., 1971; Rogerson et a., 1973; Code et al., 1970; Meade & Code, 1980), and the IUE spectrum, swp50032rl, from M. Festou (private communication).

Table 9.1 Physical Properties of αVir

Star[a]	r[b]	$r0_\odot$[c]	T[d]	v[e]
Primary	73.6	7.97	23000	1.
Secondary	73.6	3.64	19000	1.

[a]binary period 4 d; E(B−V) = 0.025
[b]distance (pc)
[c]radius in solar radii
[d]surface temperature (K)
[e]radial velocity (km s^{-1})

Figure 9.1 shows the stellar model compared to the *Cp-IUE* observations. The model deviates from the Copernicus spectrum at and below 1100 Å, but the spectra are well-filled by the model over the full range of the UVIS fuv. The spectra are given in absolute photon flux units as indicated in the figure. The model spectrum, calculated at a resolution of about R ~15000, is convoluted with a 2 Å Gaussian point spread function (psf) in Figure 9.1. The αVir model is based on the privately communicated nLTE calculations by R. Kurucz and J. Aufdenberg.
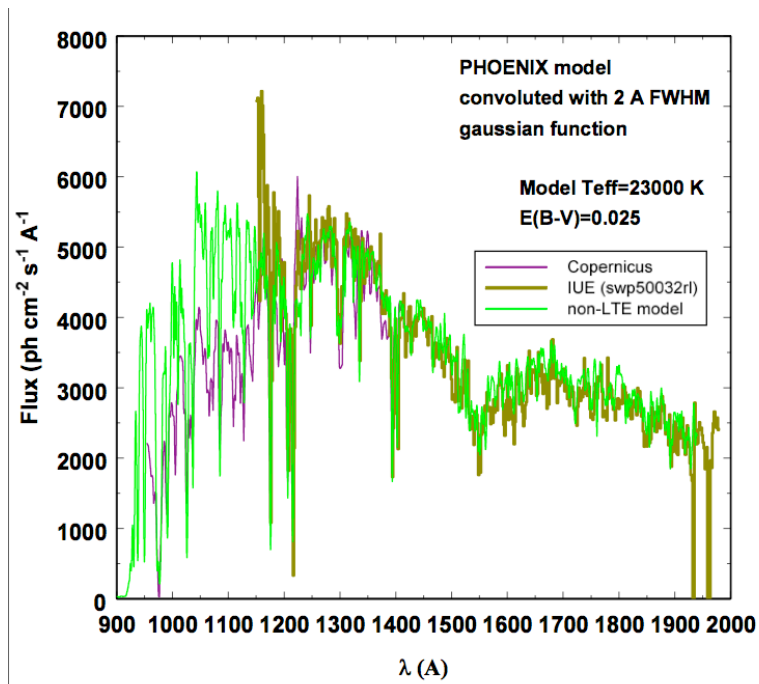
Figure 9.1: Comparison of αVir spectra from Copernicus and IUE exposures giving differential photon flux in the range 900 – 2000Å. The nLTE calculations of blanketed surface flux by R. Kurucz and J. Aufdenberg are plotted on the observed spectra as indicated.

9.3. Reduction methodology

UVIS FUV star calibration raw data obserbed in 2003 and 2005 were obtained from G. Holsclaw (see Chapter 3 by Holsclaw). Archived data from 2001 are from an exposure of 1740s duration (2001 093 09 05 28) centered on spatial pixel (pxs) 32. The data from 2003 consists of 14 files (2003 139 18 12 02 - 2003 140 06 22 38) used by A. Steffl in flatfield development. The data from 2005 is a single scan (2005 295). The scans in 2003 and 2005 were at a rate of 0.02 mrad s^{-1}, giving an assumed 50s integration period per pixel. Unlike the standard approach (see Chapter 3, section 5), no spectral data numbers are excluded in the reduction process. The author disagrees with discarding the "evil" pixels (Chapter 3). In this alternate approach, we average over all pixels not excluding any, resulting in a reduced spectral resolution. The normal reduction process at Space Environment Technologies/Planetary and Space Science Division (SET/PSSD) is to filter the spectral vectors using a single normalized 1,4,6,4,1 pass filter. This process moderately reduces the spectral resolution, while providing a much more tractable fixed pattern correction. This is not considered a loss of information because the fixed pattern in the fuv channel is severe. Figure 9.2 shows the data reduction in selected pxs (spatial pixels) for 2001, 2003, and 2005. The results shown here are counts normalized to a 100s pxs^{-1} integration period.

The nLTE αVir model after transformation by the UVIS fuv instrument simulator is plotted twice in this figure, once using the laboratory sensitivity curve (calibration file cuvisfu10.cal), and once using the curve modified to fit the 2001 observation (cuvisfu11.cal). The model and data show agreement to ~10% in the 1200 – 1500 A region, indicating agreement between the independently calibrated Copernicus, IUE, and UVIS fuv in this part of the spectrum. The known strong depletion in pxs 32 shown in the 2003 and 2005 data is evident in Figure 9.2, although there is an indication of a moderate recovery in 2005. At wavelengths > 1500 Å increasing sensitivity with time is evident. In this analysis pxs 24 is used as the calibration reference for the 2003 and 2005 data and pxs 32 for 2001 by necessity.
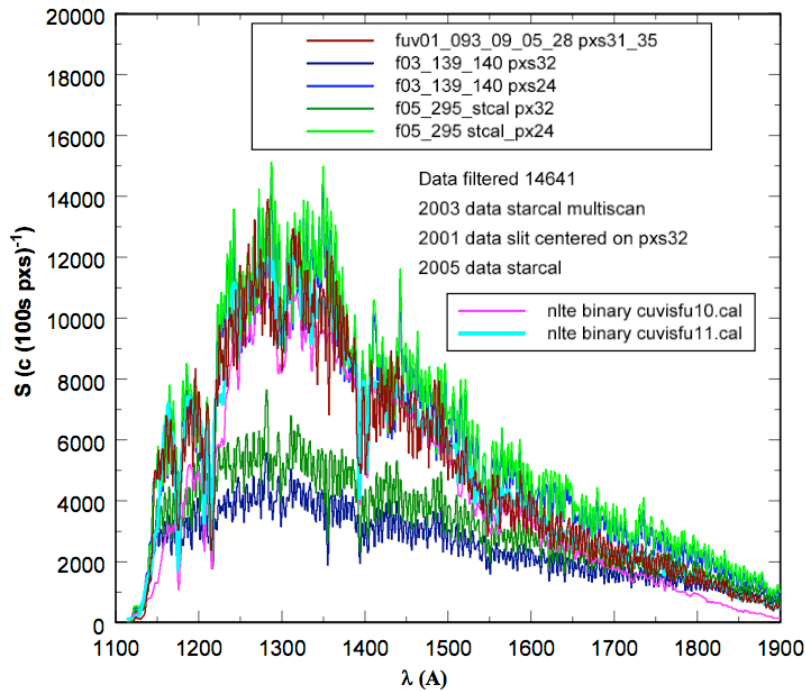

Figure 9.2: Comparison of αVir spectra from UVIS fuv exposures giving signal counts (100s pxs)[-1] in the range 1100 – 1900Å. The forward modeled nLTE calculations of blanketed surface flux by R. Kurucz and J. Aufdenberg are plotted on the observed spectra using the original laboratory calibration file and the calibration file fitting the 2001 measurement. The 2001 exposure was centered on pxs 32 only. The 2003 and 2005 data for pxs 32 and 24 are shown on the plot. In the 1200 - 1400Å region the 2003 and 2005 pxs 32 response shows severe depletion, while psx 24 is similar to 2001 pxs 32.

9.3.1 Spectral sensitivity curve derivation

The UVIS fuv sensitivity curves are determined by dividing the data by the model of the fuv spectrograph signal for αVir. The instrument sensitivity and flatfield corrections should be handled at the same time: the instrument sensitivity will differ if anomalous pixels with less sensitivity are deleted. In our methodology the spectrum in row 24 is chosen as the reference

vector for 2003 and 2005. The 2001 sensitivity in row 32 is apparently very close in magnitude to the later data in row 24, so the earlier calibration based on row 32 is consistent with the later observations. Figure 9.3 shows the ratio of data to model for the 2001 pxs 32 exposure based on cuvisfu10.cal, and the derived cuvisfu11.cal. The cuvisfu11.cal curve is determined by establishing a loess fit to the data/model ratio for cuvisfu10.cal and scaling the resulting curve to achieve a low-pass curve with a constant mean value of 1, giving cuvisfu11.cal as the best current estimate of UVIS sensitivity.
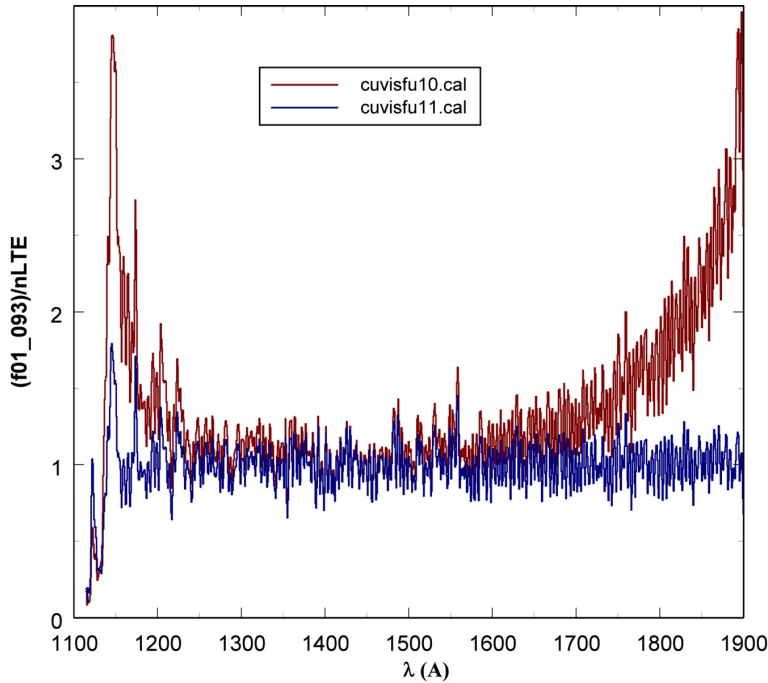
Figure 9.3: The ratio of the UVIS fuv 2001 093 αVir exposure at row 32 to the nLTE model simulation using the original lab calibration sensitivity curve cuvisfu10.cal, compared to the ratio obtained using the simulation with sensitiviy curve cuvisfu11.cal. The cuvisfu11.cal curve is obtained from a low-pass loess fit to the ratio using the simulation with cuvisfu10.cal.

The sensitivity curves derived from the data used in this analysis compared to the original lab calibration are shown in Figure 9.4. The sensitivity is given in count rate per kR for the low resolution slit. The sensitivity quantity refers to a monochromatic source at a given wavelength and therefore is not a differential quantity. The curves show very small changes with time in the 1250 – 1500 Å region. At longer wavelengths the temporal trend is consistently toward higher sensitivity with advancing time. At 1900 Å the laboratory determined sensitivity is below the value in 2005 by a factor of ~8.

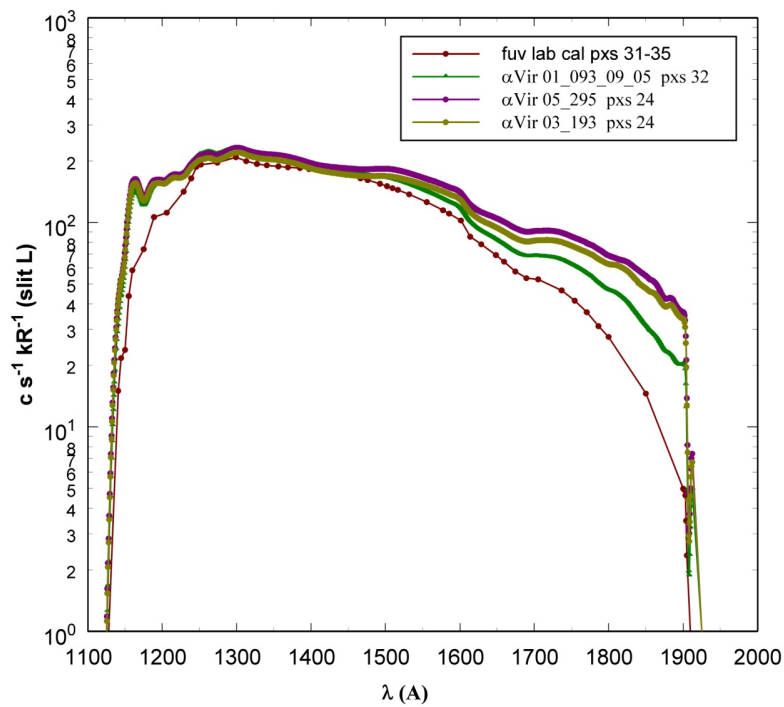Figure 9.4: Sensitivity of the UVIS fuv channel determined from the laboratory calibration, compared to results from observations of αVir in 2001, 2003, and 2005. The sensitivity refers to a monochromatic source at a given wavelength.

Figure 9.5 gives the fundamental intrinsic sensitivity in units of counts per photon for the UVIS fuv corresponding to the Rayleigh brightness scale given in Figure 9.4.
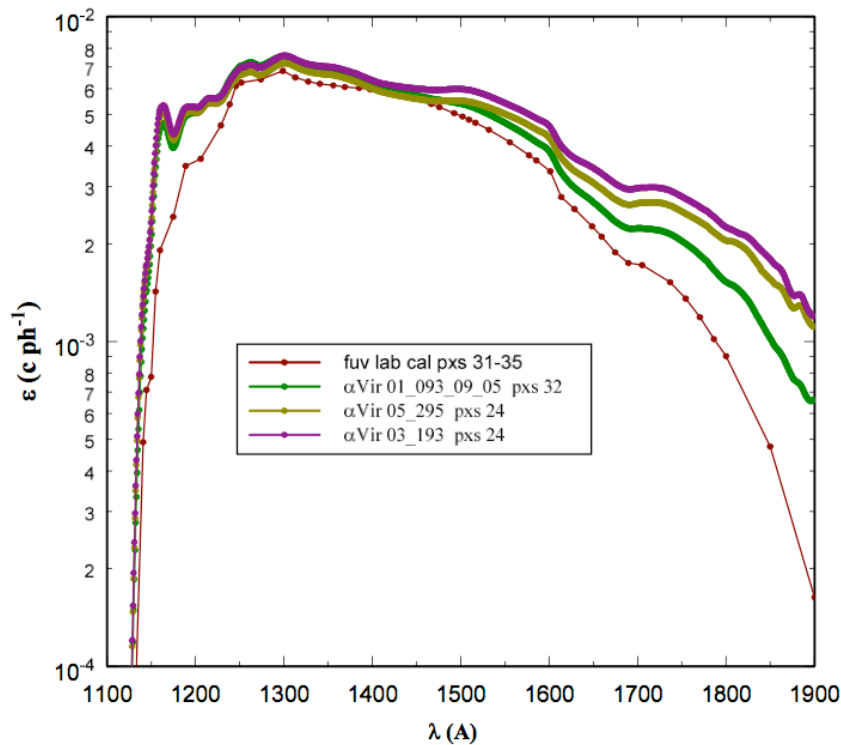
Figure 9.5: Intrinsic monochromatic efficiency, ε (counts/photon), of the UVIS fuv channel determined from the laboratory calibration, compared to results from observations of αVir in 2001, 2003, and 2005.

9.4 Discussion

In general, the sensitivity curves should be used with the corresponding flatfield vectors obtained using the methodology applied here, because the sensitivity varies from row to row. Users interested in this approach should contact the author directly for the latest flat field corrections. In Section 9.3, it was pointed out that selected data values in fuv spectral pixels (pxw) are not removed from the analysis as they have been in standard reductions at LASP (See Chapter 3). All pxw values are given equal weight in the current approach described in this chapter, which is designed specifically to ensure integrity for the reduction of system scans and emission spectral analysis. The flatfield vectors obtained with the present derivation will require adjustment at a few specific spectral locations where artifacts result from structure in the αVir spectrum. Future adjustments will be made using flatfields developed from LISM exposures. The LISM flatfields will be systematically compared to the stellar reductions to ensure integrity.

10. UVIS EUV/FUV channel Saturn and Titan occultation reduction

Donald E. Shemansky

10.1 Introduction

Spectrally resolved occultations of planetary objects using stellar and solar sources are obtained using the UVIS euv and fuv channels. Solar occultations are confined to the euv channel. In general the absorption spectra of the atmospheric species are spectrally overlapped, requiring iterative fitting of the extinction profile. The analysis is complicated by the broad wings of instrument point spread function (psf) particularly in this case because of the large dynamic range in extinction spectra that contain large optical depths. The analysis of occultation spectra is carried out using forward simulation of instrument response to the modeled transmission spectrum, to match the observed spectrum. Analysis of occultation data is described by Shemansky et al., 2005, Liang et al., 2007, Shemansky & Liu, 2012a,b. Details of the instrument properties are provided in the UVIS Calibration Report (McClintock, 2002; Esposito et al., 2004).

10.2. Data reduction methodology

The occultation sequences are designed to include reference spectra free of extinction with signal to noise ratios (SNR) substantially higher than those obtained in the occulted spectra, in order not to limit accuracy. The measurements are based on spectral ratios and therefore do not depend on instrument spectral relative sensitivity. The reduction process is as follows:

1) Data stream records are accumulated at intervals appropriate for obtaining signal levels at a minimum level for analysis in order to maximize the spatial resolution of the atmospheric probe. A reduction code is used to accumulate the extinction free signal, generally with a statistical factor of 10 higher SNR than the extinction spectra. The spectra are accumulated with the full spectral resolution. Solar occultations are accumulated in two independent windows with a fixed protocol in 1s integration intervals. The solar image is defocussed in the spatial dimension and the spatial signal is accumulated in 2 windows distributed across ~40 pixels (pxs). The spectral dimension of the solar image is in focus and is simulated in the model analysis process.

2) Engineering data corresponding to the UVIS data stream is obtained from the UVIS Data Archiving and Processing System (DAPS) data accumulation system. Modified versions of the *geometer* code developed in the LASP UVIS program are used to extract the range of necessary auxiliary data such as the impact parameter (IP) of the line-of-sight (los) to the source, latitude and longitude (lat, long) of the IP, distance to target.

3) The spectra are filtered 1,4,6,4,1 (in the spectral dimension) in order to mitigate the fixed pattern variance in signal rate caused by evil pixels. This process has the effect of moderately reducing spectral resolution.

4)　　　Spectra are forward modeled iteratively in optical depth in order to account for artifacts (caused by other sources in the field of view and by pointing variations during the observation) and for internal scattering.

5)　　　Effective altitudes of the impact parameter are calculated from measured scale heights following reduction of the entire vertical profile. Because of their different vertical profiles, individual species in general have different effective altitudes within the same integration interval.

6)　　　Vertical density profiles are calculated through deconvolution of the abundance profiles, and verified by direct integration compared to the measurements. See C.D. Rogers (1976).

7)　　　Species such as methane and acetylene have temperature sensitive cross sections, requiring iterative determination of temperature and fitted extinction spectra to obtain accurate profiles.

8)　　　Correct for the stellar or solar images motion on the detector. In Titan occultations, in particular, it is often necessary to switch pointing control between reaction wheels and thrusters, causing irregular image motion. Even sub-pixel motion of the source image can generate un-analyzable spectra. Some occultations are not recoverable because of pointing variations.

10.3. General properties of extinction spectra

The species observed in extinction in the Saturn system are H_2, HI, H_2O, hydrocarbons, and nitriles. The extraction of absolute quantities requires of high resolution photo-absorption cross sections. In general molecular absorption cross sections show temperature dependence. In many cases the laboratory data-base is the limiting factor in deriving species abundances, and in particular temperature dependence is a missing factor for many species.

10.3.1 Influence of instrument point spread function (psf)

Figure 10.1 shows a partial spectrum obtained at Titan TB encounter compared to a model fit using the full psf in the reduction code, compared to a model with the same species abundances using the core of the psf without the broad wings. Not using the full psf causes unacceptable errors in the spectral model. Strong narrow features are not correctly modeled, and the absolute intensity is in error without the use of the fully developed psf.

Figure 10.1: Occultation extinction spectrum of αVir at Titan TB encounter against model calculations for an impact parameter altitude of 827 km. The fully developed model is shown in green, compared to the same model in red, but containing only the core component of the psf, illustrating the consequences of inadequate instrument simulation. Derived species abundances are given on the plot. Signal noise limits the analysis to an optical depth of 6.

The entire spectrum containing Figure 10.1 is shown in Figure 10.2, in order to demonstrate the quality of the model fit that can be achieved. The absorption cross-sections for the species that dominate the spectrum in this case were obtained at a temperature of 150 K in the laboratory. At lower altitudes on Titan the temperature drops below 150K and this is evident in the extinction spectrum (Figure 10.3).
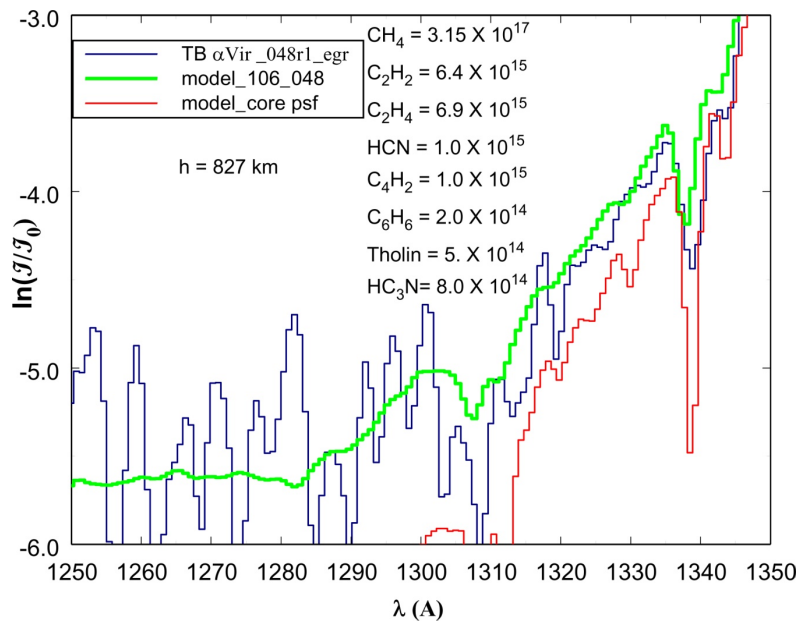
Figure 10.2: Occultation extinction spectrum of αVir at Titan TB encounter against model calculations for an impact parameter altitude of 827 km. Figure 10.1 is a long wavelength component of this spectrum. The fully developed model is show in green. The species CH_4, C_2H_2, and C_2H_4 are built into the model at a temperature of 150 K. Signal noise is evident at an optical depth of 6.

10.3.2 Temperature dependence in molecular cross sections (psf)

In principle, temperature dependence in molecular cross sections can be used to measure atmospheric kinetic temperature, although in the case of hydrocarbons accuracy is limited. As temperature decreases the rotational structure populations concentrate toward the band heads, narrowing the resonance band absorption widths (Wu et al., 2001). Figure 10.3 shows the spectrum near 700 km, where the resonance features no longer fit the 150 K model, particularly for C_2H_2, where the data show deeper, narrower, structure that cannot be modeled with higher temperature cross sections. Derived abundances are given on the figure plots showing values an order of magnitude higher at 700 km compared to 827 km. Derived properties of the Titan atmosphere are described in Shemansky et al.(2005), and Liang et al.(2007).
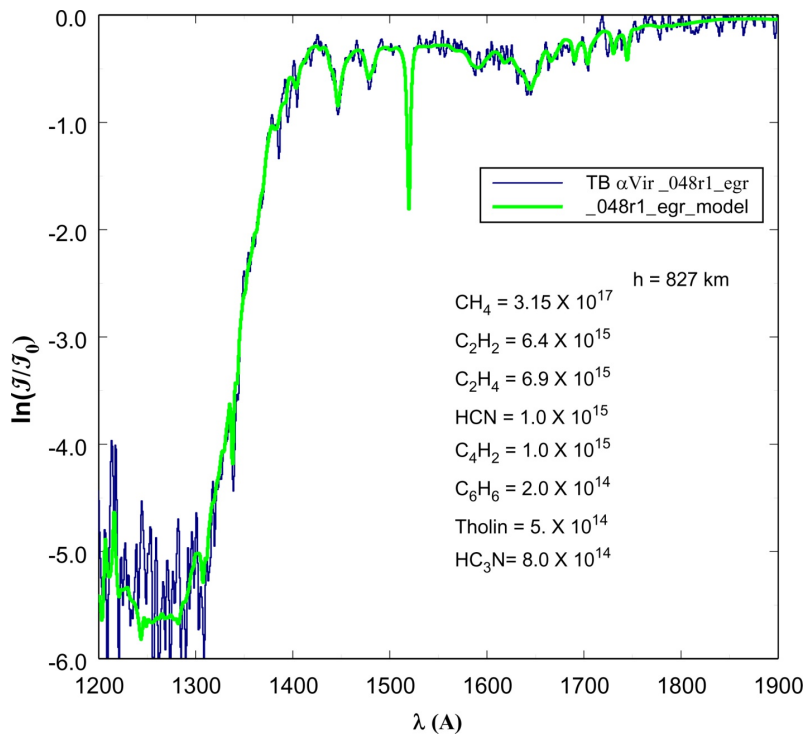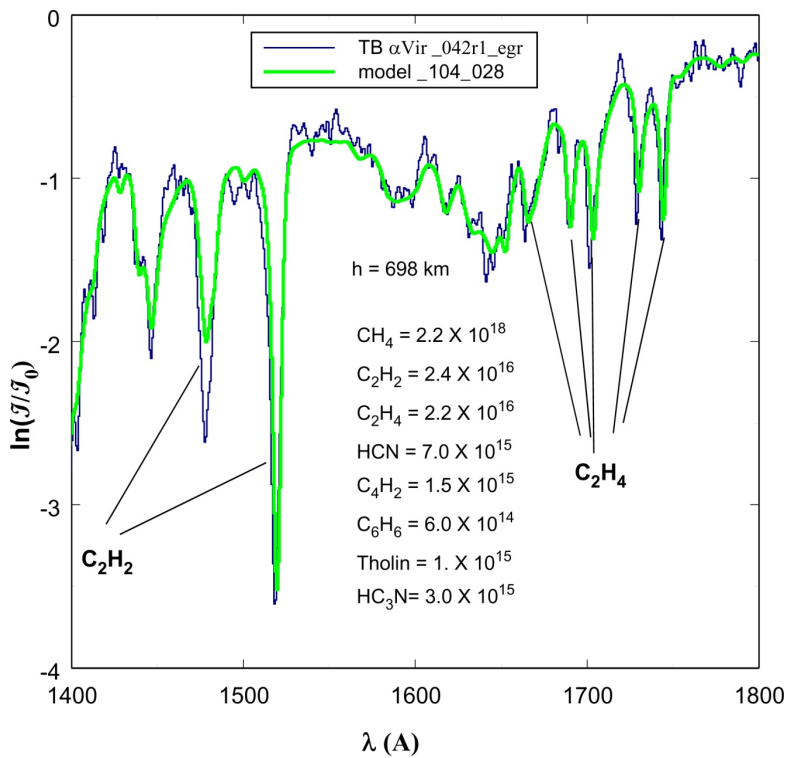
Figure 10.3: Occultation extinction spectrum of αVir at Titan TB encounter against model calculations for an impact parameter altitude (IP) of 698 km. This spectrum is more than 1 optical depth below the location of the spectrum in Figure 10.2. The C_2H_2 and C_2H_4 resonances show deviation from the models likely caused by atmospheric temperature in the vicinity of 135 K. Compare to model fit in Figure 10.2 at 827 km.

10.3.3 Solar occultations

The UVIS euv channel contains a solar occultation port with a principal axis at an angle of 20° to the airglow axes used for stellar occultations. This port restricts input flux with a 50μ aperture and dilutes the image density on the detector with an asymmetric optical reflector (McClintock, 2002). Solar occultations are more subject to pointing instabilities than observations through the airglow ports. At Titan, solar occultations provide the ability to measure the abundance of N_2, particularly at high altitude. Figure 10.4 shows the Titan transmission spectrum at high altitude, where the H Lyγ solar line is absorbed by the N_2 b(3,0) band. The N_2 abundance is measured above the exobase, providing the ability to determine the collision free escape rate. The figure shows the extinction-free spectrum compared to the spectra above the exobase at IP of 1556 and 1721 km. Extinction of the N_2 b(3,0) band is near saturation in both cases. These spectra required spectral phase correction in order to obtain valid abundance

measurements. An example of uncorrected spectral vectors is shown in Figure 10.5 where the displayed spectra are shifted by more than 2 spectral pixels (pxw) by pointing motion.
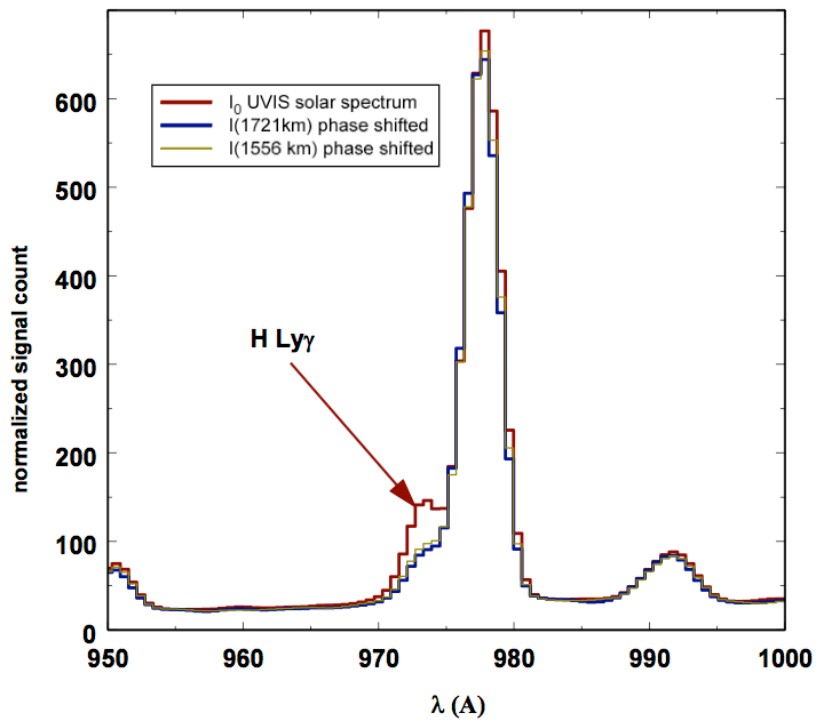

Figure 10.4: Transmission spectrum solar occultation at Titan T10 showing H Lyγ extinction by the N_2 b(3,0) band. The extinction-free spectrum is compared to the spectra at IP 1721 and 1556 km. The spectra are phase shifted to correct for image motion on the detector.
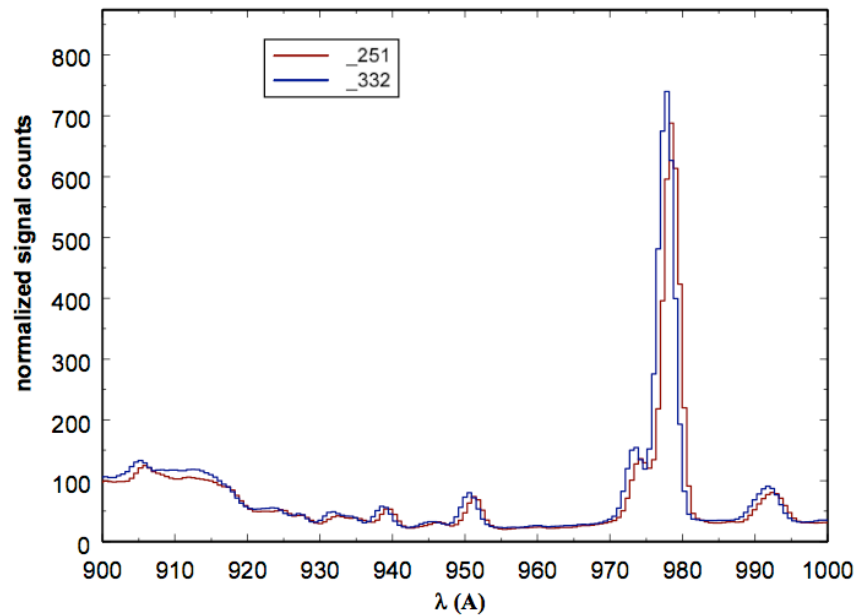
Figure 10.5: Transmission spectrum solar occultation at Titan T10 showing two vector records shifted by more than 2 pxw by image motion on the detector.

10.4. Atmospheric vertical structure

Vertical profiles in atmospheric structure obtained from the combined occultation and engineering data (Sec 10.2) provide the means of determining the nature of the state of the atmosphere, atmospheric dynamics and physical chemistry. UVIS is the only Cassini remote sensing system that can probe the hydrocarbon homopause region of the thermosphere on Titan or Saturn.

10.4.1 Vertical structure at Titan

The results obtained using UVIS overlap with the INMS experiment above 950 km at Titan, and the CIRS experiment in the range 300 km to 400 km at Titan. At Saturn UVIS results can be compared to CIRS at pressures between 1 and 1000 μb (Shemansky & Liu, 2012a). A comparison of number density results for Titan from UVIS observations, INMS and Voyager are shown in Figure 10.6. The indication internally from UVIS observations is that the vertical distribution of N_2 and the hydrocarbons depends on a combination of season and latitude. The UVIS observations of N_2 in general do not correspond well with Voyager, or INMS results. For CH_4 better agreement is obtained between Voyager and UVIS results, but most of the UVIS observations produce higher densities by a factor of ~3 compared to INMS (Shemansky et al., 2005; Liang, et al., 2007; however, see the recent corrections to INMS suggested by Westlake et al.). The measurements of temperature in the Titan upper thermosphere from the UVIS

observations are substantially higher than those published from the INMS experiment. The indication is that exobase temperatures are generally higher by ~50K than the INMS published results. Lower temperatures reported by UVIS (Shemansky et al., 2005) are based on lower altitude results for CH4.
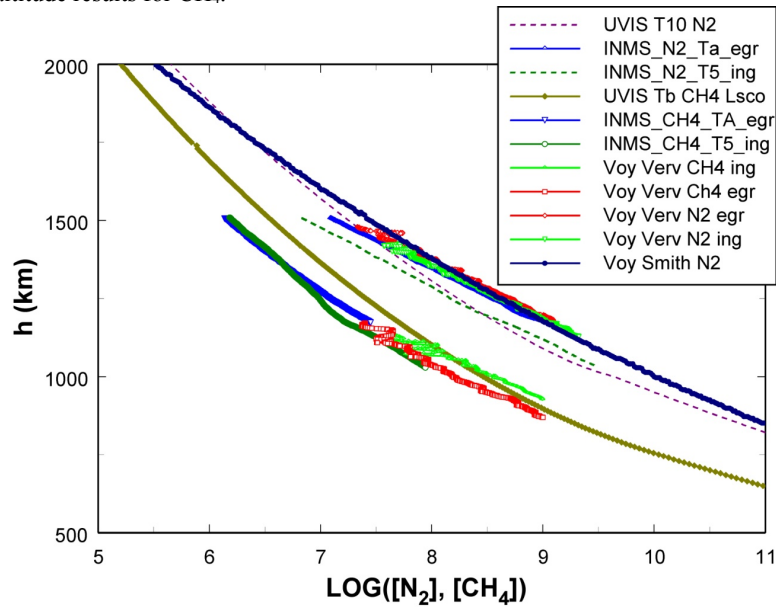
Figure 10.6: Vertical density profiles of N2 and CH4 at Titan from UVIS, INMS and Voyager observations. Sources of the plots are indicated on the figure legend. The line plots are model calculations constrained by the reduced data.

Figure 10.7 shows the vertical abundance distributions of N_2 and CH_4 from the UVIS solar occultations at Titan encounters T10 and T26. These observations were obtained at lat -61° - 51° and -76°. The temperatures in the two cases differ by about 10K, and while the N_2 abundances below 1200km are similar, the CH_4 profiles differ by about a factor of 2. The N_2 curves diverge in the exobase above 1200 km, reflecting the difference in temperature. These results are indicative of slow atmospheric dynamics allowing non-uniformity driven by insolation and deposition from the magnetosphere.
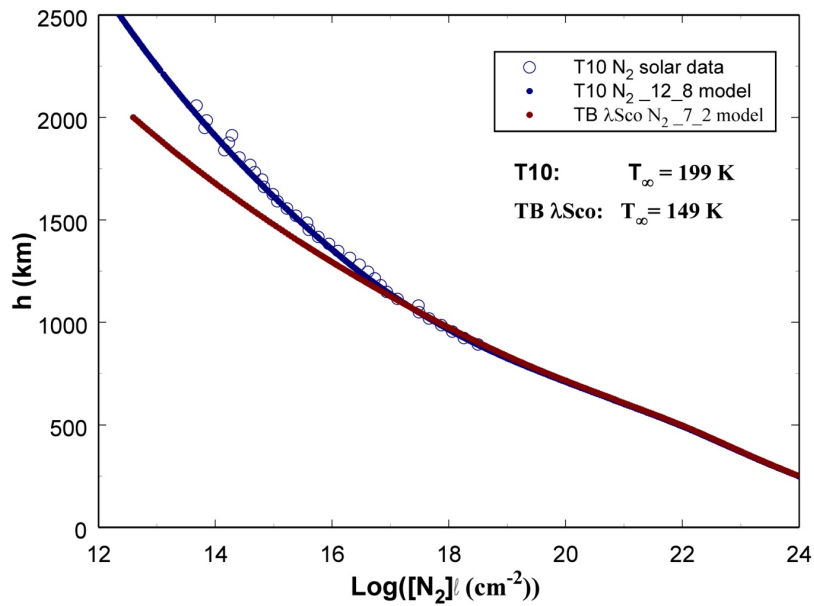
Figure 10.7: Vertical abundance profiles of N2 and CH4 at Titan from UVIS solar occultations at T10 and T26. Sources of the plots are indicated on the figure legend. Plotted points are reduced data, solid and dashed lines and hydrostatic model calculations constrained by the data.

10.4.2 Saturn hydrocarbon extinction compared to Titan

The Saturn and Titan atmospheres have hydrocarbons in common as minor species. The physical chemistry determining the CH_4, C_2H_2, and C_2H_4 components produce similar mixing ratios among these species on the two bodies. There are, however distinct differences in the chemical physics of the higher order hydrocarbons. Titan shows distinct physical chemistry proceeding at high altitude into production of heavy ions and molecular clusters forming aerosols. The aerosols are ultimately the most important component at Titan, because they influence atmospheric dynamics, surface properties, thermal structure, and atmospheric escape. Figure 10.8 shows a comparison in the fuv occultation measurements at similar optical depths in the low order hydrocarbons. The Saturn atmosphere shows near zero extinction at 1875Å, where the low order hydrocarbons do not have measureable cross sections, while the Titan extinction spectrum shows a significant loss over the entire spectral range.

Figure 10.8: Comparison of Saturn and Titan hydrocarbon extinction spectra at similar levels of low order hydrocarbon abundances. Strong aerosol extinction is evident at Titan, but not detectable at Saturn.

10.4.3 Saturn hydrocarbon vertical structure and composition

Figure 10.9 shows hydrocarbon mixing ratios as a function of altitude above 1 bar. The vertical scales show dependence on latitude with more vertical extension at low latitudes. The structural difference is ap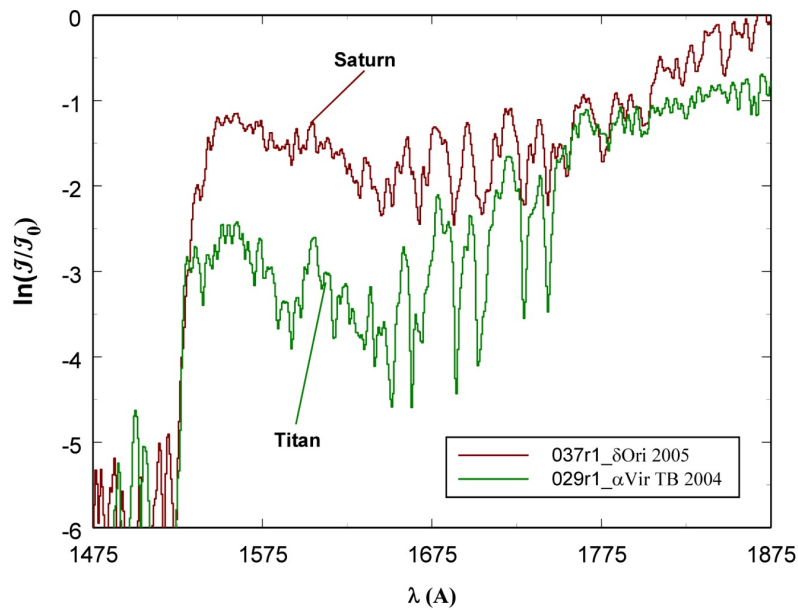parently mainly a matter of atmospheric scale height. Figure 10.10 shows mixing ratio as a function of pressure where the profiles are more closely aligned, but with differing structural detail. C_2H_2 and C_2H_4 show maxima at mid latitude just above and below 1 µb, and minima near the equator. The structure has the scale size of roughly the scale height, indicating strong order of magnitude variation in mixing ratio at particular pressure levels and different latitudes. The vertical resolution in UVIS observations is higher than other instruments can achieve. The homopause in the UVIS observations to date occurs at a common pressure level for the different latitudes (~0.2µb). The wave structure in the hydrocarbon profiles includes CH_4. The UVIS measured hydrocarbons at Saturn are CH_4, C_2H_2, and C_2H_4 (Flasar et al., 2005). Upper limits for C_4H_2 and H_2O have been established for the UVIS occultations (Shemansky & Liu, 2012a, b). The C_4H_2 upper limit is shown in Figure 10.10. The CIRS results from Guerlet et al. (2008) plotted in Figure 10.10 agree with the UVIS results at some pressure levels, but differ by an order of magnitude at other locations in the pressure scale. The results shown for Guerlet et al. (2008) are a combination of model calculation and CIRS data. The Guerlet et al. (2008, 2009) results depend on an independent determination of the CH_4 profile (see also Howett et al., 2007). The model calculations Moses et al.(2005), Moses & Greathouse (2005) are included in Figure 10.10. These profiles use a much larger eddy diffusion coefficient than is inferred from the UVIS results, forcing substantial differences in profile. The UVIS upper

limit for C_4H_2 is compatible with the Moses et al. (2005) model. The CH_4 profile from the Voyager UVS measurements, used by Moses et al. (2005) to establish eddy diffusion properties, as also shown in Figure 10.10. The indication is that significant physical atmospheric changes have occurred since the Voyager encounters, plausibly related to phase in the major solar cycle.
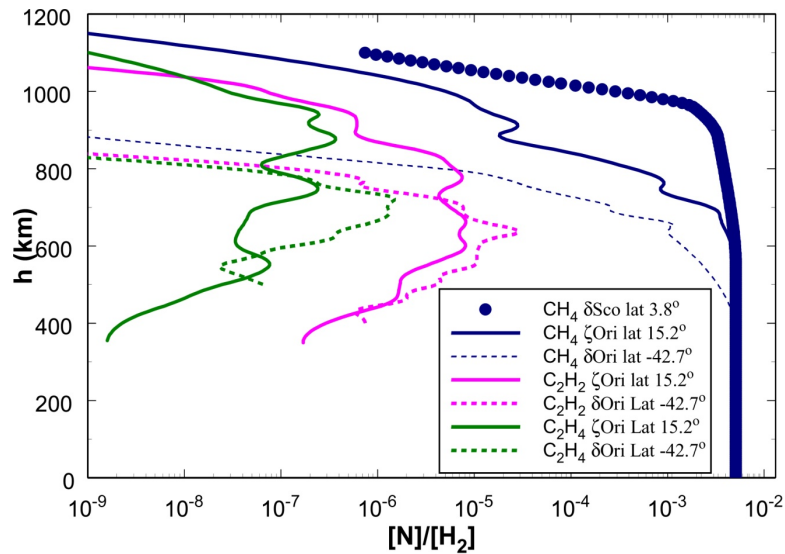

Figure 10.9: Mixing ratios [N]/[H_2] as a function of altitude at Saturn. See Shemansky & Liu, 2012a. The differences in H2 density scale heights between the occultations evidently do not entirely compensate for the hydrocarbon scale differences. The CH_4 δSco result is from the Voyager occultation (Smith et al., 1983).
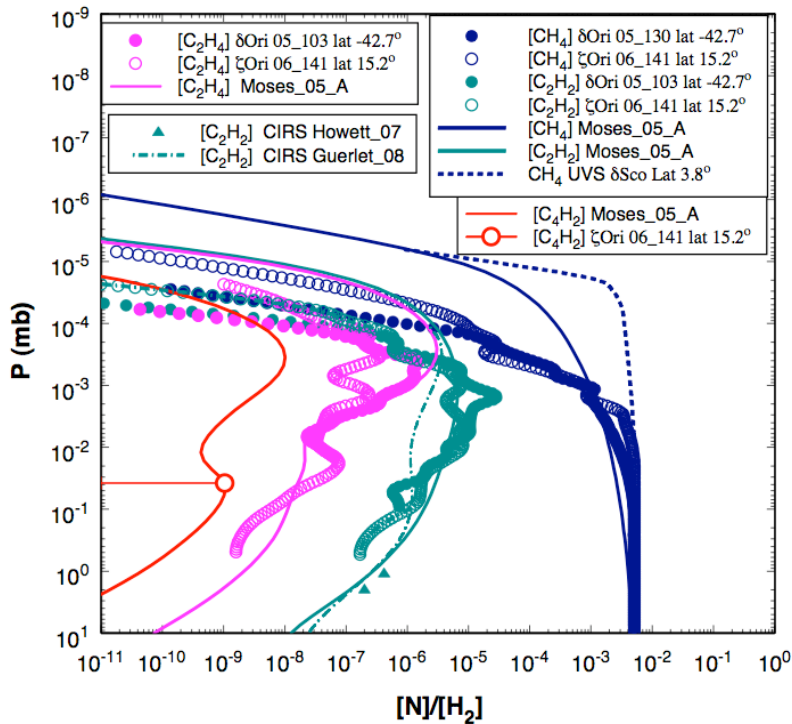
Figure 10.10: Mixing ratios [N]/[H$_2$] as a function of pressure for the hydrocarbons CH$_4$, C$_2$H$_2$, C$_2$H$_4$, C$_4$H$_2$, compared to the Voyager 2 δSco latitude 3.8° CH$_4$ reduced data, Cassini CIRS analyses (see text), and model calcuations by Moses et al. (2005) (from Shemansky & Liu, 2012a). The Guerlet et al. (2008) profile for C$_2$H$_2$ shown as the dash-dot curve is for latitude 16.7°. The Moses et al. (2005) model (A) profiles are global. The plotted points (C$_2$H$_2$) for Howett et al. (2007) are for planetocentric lattitude -42°. The Cassini UVIS occultations at latitudes -42.7° and 15.2° show a common homopause on a pressure scale. The Voyager CH$_4$ profile (Smith et al., 1983) shows a homopause at substantially lower pressure, comparable to the Moses et al. (2005) model. Significant structure appears in the Cassini UVIS profiles (see text). The plotted point for UVIS ζOri C4H2 is an upper limit. Error bars in the Cassini UVIS mixing ratios are smaller than the size of the plotted points, except at the ends of the pressure range.

10.4.4 Saturn hydrogen

The Saturn euv extinction spectrum is dominated by H$_2$. Hydrocarbons are not detectable in this region of the spectrum because H$_2$ reaches extreme optical thickness before the hydrocarbon homopause is reached. Figure 10.11 shows the extinction spectrum, analyzed as pure H$_2$. The H$_2$ X state is in general considered to be in non-LTE in vibration. The spectrum is therefore modeled by iteratively fitting the observation using individual independent absorption vectors associated with the ground state vibrational levels. The rotational populations in the ground state are assumed to be in thermal equilibrium, although this may not be the case at all altitudes. The model calculations for the H$_2$ absorption vectors include coupling and perturbations on state properties, not yet published. A non-LTE model for the physical chemistry of weakly ionized hydrogen has been published (Hallett et al., 2005a,b).
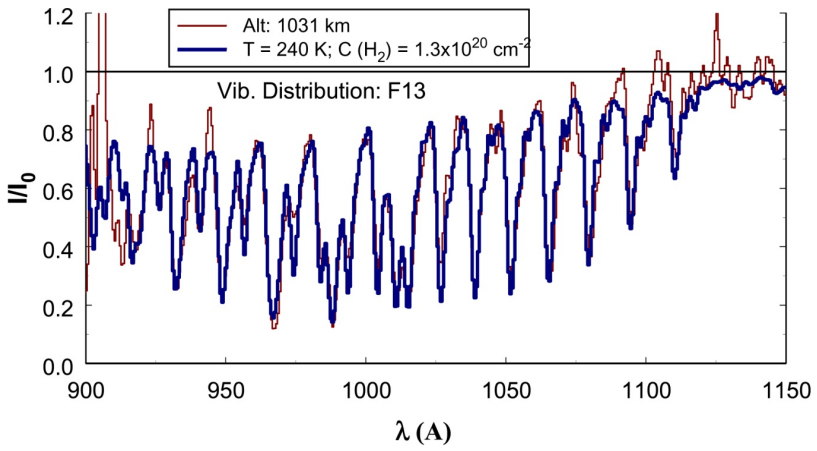
Figure 10.11: UVIS EUV stellar occultation transmission spectrum obtained 2005 DOY 103 at effective impact parameter 1031 km. The rotational temperature is iteratively determined assuming LTE. The vibrational population distribution is non-LTE determined iteratively by fitting separate vibrational vectors into the model for optimal match to the spectrum.

11. Cassini UVIS IPHSurvey Data

Wayne Pryor

11.1. Introduction

IPHSurvey (Interplanetary Hydrogen Survey) data make up a substantial part of the data taken by the Cassini UVIS instrument throughout the mission. IPHSurveys are regularly obtained to monitor directions AWAY from planets and satellites. These observations primarily monitor changes in solar illumination of the interstellar wind: relative motion between the Sun and the local interstellar medium provides a flowing stream of H and He in the solar system, moving from "upwind" near ecliptic longitude 250 degrees to "downwind" near ecliptic longitude 70 degrees. Thomas (1978) provides a good introduction to the interstellar wind and basic modeling efforts. Figure 11.1 (from Pryor et al., 2008) illustrates the interstellar wind flow and its interaction with the solar wind in the outer heliosphere.
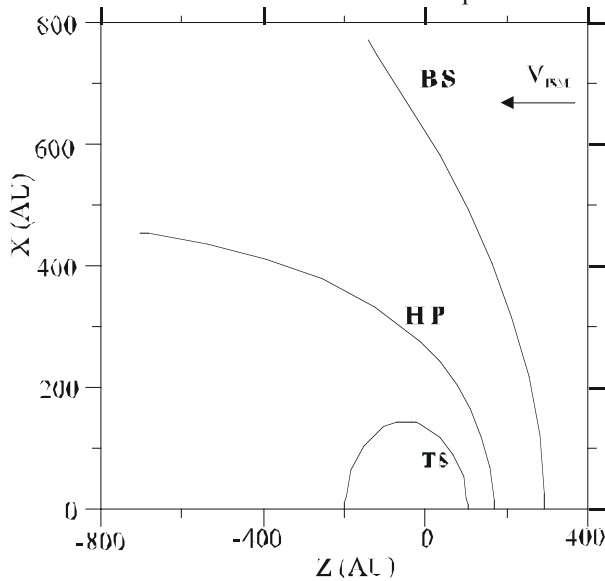
Figure 11.1. Illustrates how a flow of interstellar neutrals and plasma at velocity V_{ISM} from the upwind direction interacting with the solar wind flowing radially outwards from the Sun (located at $Z=0$, $X=0$) sets up a bow shock (BS), heliopause (HP), and solar wind termination shock (TS) in a Baranov-Malama type model.

The UVIS IPHSurvey data may also be relevant to studies of H, He and O originating in the Jupiter and Saturn systems. Finally, because the interplanetary emissions are spatially extended, IPHSurvey data provide a check on the UVIS detector flat fields and their variations in time.

Figure 11.2 (from Pryor et al., 2008) shows the observation geometry for IPHSurvey observations in the cruise phase of the mission before orbital insertion at Saturn in 2004. For

most of that period, Cassini was in the downwind hemisphere. Since 2004, Saturn's orbital motion with its 29.5 year period has gradually moved the spacecraft into the upwind hemisphere.

CASSINI
INTERPLANETARY TRAJECTORY

VENUS SWINGBY
26 APR 1998

VENUS SWINGBY
24 JUN 1999

ORBIT OF
EARTH

DEEP SPACE
MANEUVER
3 DEC 1998

ORBIT OF
VENUS

LAUNCH
15 OCT 1997

EARTH SWINGBY
18 AUG 1999

ORBIT OF
JUPITER

interstellar wind flow

JUPITER SWINGBY
30 DEC 2000
(DOWNWIND)

SATURN ARRIVAL
1 JUL 2004

ORBIT OF
SATURN

PERIHELIA

27 MAR 1998 0.67 AU
29 JUN 1999 0.72 AU
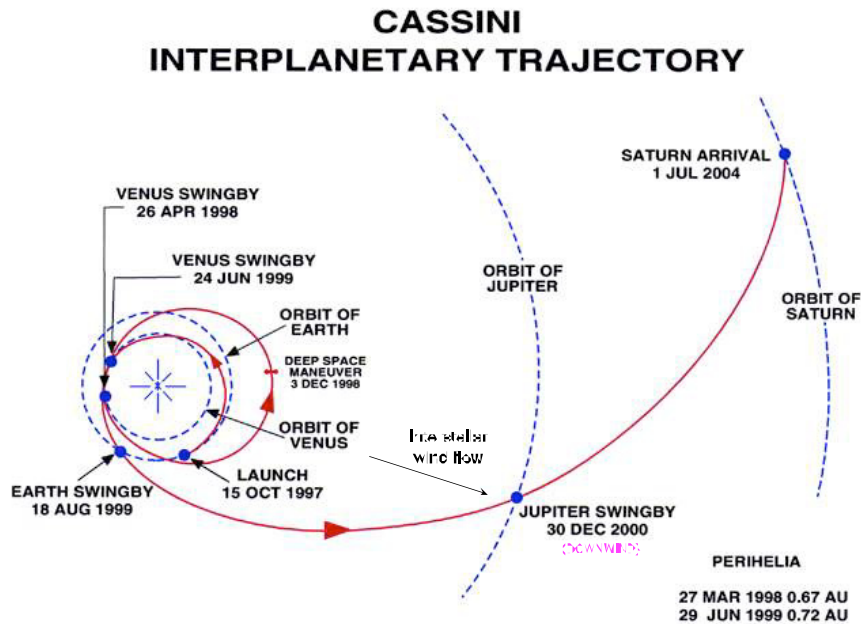
Figure 11.2. The Cassini spacecraft's trajectory to Saturn placed it downwind with respect to the interstellar hydrogen flow in late 2000 during the Jupiter swingby. The view is looking from eclipcit north down onto the ecliptic plane. Downwind is indicated in magenta. The Cassini spacecraft was somewhat more sidewind in 2003-2004. Voyager 1 was upwind during this period.

11.2 The Data Base

IPHsurvey data can be found in the PDS archive label files with target_name="SW". The wide variety of IPHsurvey observations can be further organized in terms of their "ODC_ID" numbers, where each   instrument configuration was categorized by ODC_ID number.   The PDS label files can be searched by ODC_ID number. IPHsurvey ODC_ID numbers include 29, 30, 31, 33, 34, 49, 51, 52, 53, 56, 57, 58, 83, 84, 85, 103, 104, 105, 138,139, 1200, 1208, 1209, and 1212. A variety of data formats and slit widths were used: some preserved only limited spectral information, while some produced full detector readouts (64 spatial pixels by 1024 spectral pixels) which are more suitable for flat-field studies and careful studies where faint star removal is important.

11.3 Sample Data

Figure 11.3 (from Pryor et al., 2008) provides a sample UVIS FUV spectrum, showing primarily Lyman-alpha emission produced at 121.6 nm. Some FUV spectra obtained near Saturn also include 130.4 nm oxygen radiation. Not all such spectra contain this, and the matter is somewhat confused by the structured wing of the Lyman-alpha emission. Attention also needs to be paid to contamination due to stars, which frequently are in the field. These can be removed by comparing (least-squares fit testing) individual spectra to a reference "clean" Lyman-alpha spectra without obvious stars to see if they should be included in interplanetary hydrogen studies.
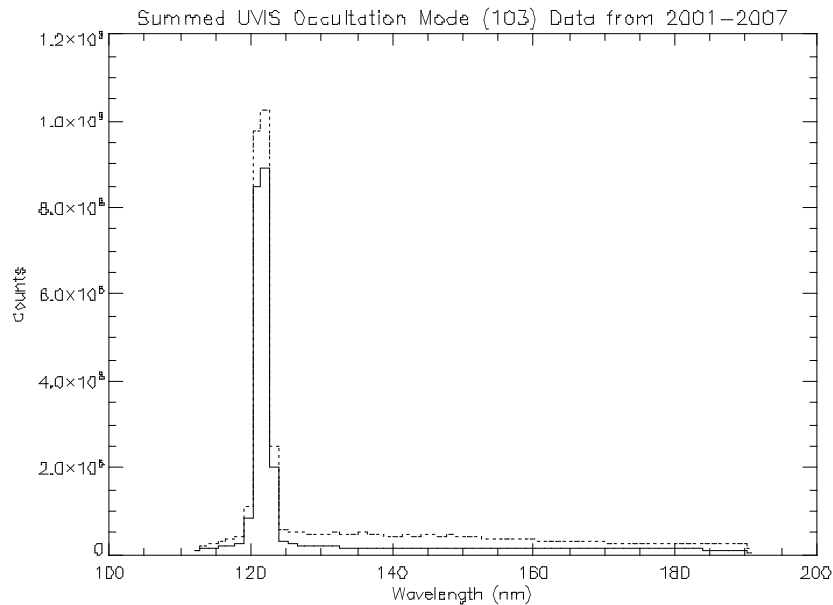
Figure 11.3 Summed UVIS interplanetary Lyman-a spectrum from 2001-2007 obtained in the widest-slit mode (occultation mode, also, for this application, called mode 103). The dotted line in the figure contains contains Lyman-α and starlight at longer wavelengths. In this case, the total integration time was 4.4×10^7 s. Individual spectra with obvious stars have been filtered out (by performing a least-squares fit to clean Lyman-alpha line spectra containing no stars obtained in-flight and rejecting spectra that are dissimilar) to create the solid line (total integration time 3.1×10^7) and the following Cassini data figures.

Figure 11.4 (lower spectrum) provides a summed UVIS EUV spectrum obtained in ODCID-103 mode, where spatial resolution along the slit has been binned together, and spectral information is returned binned into 128 spectral channels using the widest "occultation" slit position. These spectra show atomic hydrogen Lyman-beta near 102.5 nm and atomic helium He 58.4 nm emissions. EUV spectra such as this one obtained early in the mission were heavily contaminated by the "mesa" (Chapter 1): a light leak in the instrument that created counts at the lower wavelength channels below 100 nm in the spectrum. This complicated efforts to interpret the spectra. Notice also that the longest wavelength channels also have higher count levels, due to Lyman-alpha.
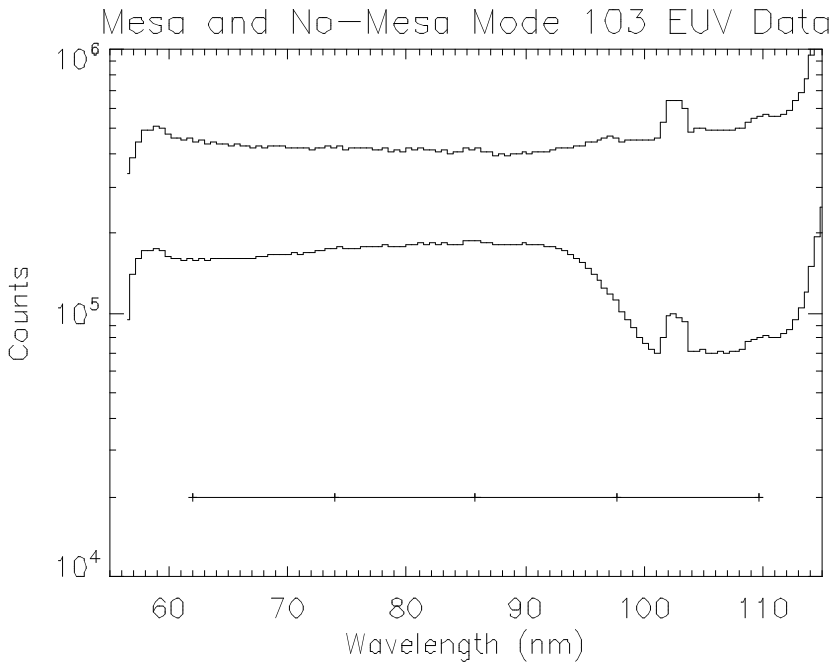
Figure 11.4. The upper curve is a sample of EUV spectral data obtained without a mesa. The lower curve is a sample of EUV spectral data with the mesa and a different integration time. Ticks along the horizontal bar mark grating ghosts due to Lyman-alpha.

11.4 Mesa Removal

During Saturn orbital operations, Ian Stewart found that moving the occultation port door to the "other position" during IPHSurvey observations removed almost all of the EUV "mesa" that had been making short wavelength EUV observations difficult. Figure 11.4 also shows (upper spectrum) a clean IPH spectrum produced after mesa removal. This opens up the lower wavelength end of the EUV spectrum to searches for weak emissions. However, it should be noted that remnants of the mesa can still appear in the EUV spectra and anomalies should be treated with caution.

11.5 Grating ghost

A search was made for weaker emissions in the interplanetary spectrum. The technique to do this takes advantage of the fact that each UVIS detector has three interchangeable slit widths. Dividing spectra obtained with one slit width by another helps to distinguish line emissions reaching the detector from detector artifacts or statistical fluctuations. Figure 11.4, especially the upper spectrum shows several of these unexpected lines in the EUV spectrum even

without the division process.   These lines were separated by about 11.9 nm and were created by Lyman-alpha "grating ghosts".   They showed up at:

121.6   -   11.9 nm   =   109.7 nm
121.6   -   2x11.9 nm   =   97.8 nm
121.6   -   3x11.9 nm   =   85.9 nm and so on.

These locations are marked along the horizontal line in Figure 11.4. The obvious emission at 978 Angstroms is quite close to the expected atomic hydrogen Lyman-gamma emission at 972 Angstroms. True Lyman-gamma emission is not obvious in the UVIS spectra, except in the spectra obtained looking at Venus where it is obvious.

Although the grating ghost was detected from Lyman-alpha, other bright spectral features may of course also cause ghosts and this should be considered in weak line identifications.

11.6. Data Calibration and Degradation

Lyman-alpha is a strong ultraviolet emission and leads to a line shape that leaves real counts all across the FUV detector.   These should all be included in estimating the brightness in Rayleighs. Lyman-alpha also affects the "background" signal in the EUV detector, even though the line center is off the EUV detector. IPHsurvey FUV data in particular should not be analyzed for photometric purposes with the original laboratory calibration. Greg Holsclaw and Bill McClintock have been monitoring the detector performance using a combination of stellar calibrations and have noticed a "reddening": improved performance at long wavelengths relative to short wavelengths.   This has changed the overall Lyman-alpha line shape.   There is also reduced sensitivity at pixels near Lyman-alpha, and in selected rows affected by excess starlight and planetary light.

The calibration pipeline now includes time-dependent flat fields derived from stellar observations suitable for handling these effects. Greg Holsclaw should be consulted for the latest pipeline developments.

11.7 Data Modeling with Interstellar Wind Models

Pryor et al., 2008 compared Cassini UVIS IPHsurvey data from 2004 near Saturn with simultaneous Voyager UVS data obtained much farther from the Sun. When compared with a standard interplanetary hydrogen model (Pryor et al., 1992; Ajello et al., 1994; Pryor et al., 2003) that did not fully include multiple scattering, there was generally good agreement between the model and the Cassini UVIS IPHsurvey data. Comparing the model with the Voyager UVS data from the same time shows that the Voyager data, while modulated in phase with the solar variations, was modulated with lower amplitude (damped), by multiple scattering effects.   Pryor et al., 2008 modeled the damping seen in Voyager UVS data with a full multiple scattering process using the Monte Carlo model of Gangopadhyay et al., 2006. This procedure, adapted from Shemansky et al., 1984 and Quemerais et al., 1996, constrains the interstellar hydrogen density in a calibration-independent fashion. Future work will compare Voyager and Cassini data from the current (2011) epoch, with increasing Lyman-alpha solar activity again providing signal modulation at the Sun.

11.8 Data Cross-Calibration

Lyman-alpha calibrations are notoriously inconsistent (e.g., Ajello et al., 1987) perhaps because the detector responses are time-dependent. It has been suggested by Hall 1992 and others that **mutual observations** where two spacecraft look towards each other, then away from each other, can lead to a clear determination of the relative calibrations of different instruments. Such experiments for Cassini are under discussion with other spacecraft such as New Horizons.

11.9 Application to the Saturn System

Inspection of the IPHsurvey data has shown that in the near-Saturn environment, in addition to the interplanetary H and He signals, there is also enhanced signal from the planetary system, especially at H. Also, O 130.4 nm emission is clearly seen.   While the IPHsurvey data contain this feature, the observer is cautioned that features of the Lyman-alpha wing resemble O 130.4 nm emission, so care should be taken in analyzing these data for the O signal. The IPHSurvey observations occur in random directions, sometimes rolling, and present a largely untapped reservoir of information on near-Saturn hydrogen and oxygen. (Targeted system scans of the extended Saturn system showing enhanced H and O emission have been studied and modeled by Melin et al., 2009. Also see Chapters 9 and 10 in this document.)

11.10 Stars and other artifacts

UVIS also is sensitive to stars, which should be removed from spectra before analysis. Hydrogen Lyman-beta (102.6 nm) analysis is particularly affected by the presence of many weak stars emitting EUV light in the wavelength range above 91.2 nm. Lyman-beta studies are still possible if sufficient attention is paid to removing very weak stars. Hydrogen Lyman-gamma studies are even more problematic, because of the weakness of the expected emission, the presence of stars, the mesa (in the cruise phase of the mission when solar lines were brighter), and the grating ghost described earlier.

One unusual spectrum (from an off-Dione ICYLON observation on 2008 day 181) later turned out to be the Vela supernova remnant (Figure 11.5).   The EUV spectrum shown included intense emissions from CIII 97.7, and OVI 103.1/103.8. Other such surprises are possible and should be watched for in IPHSurvey data analysis.
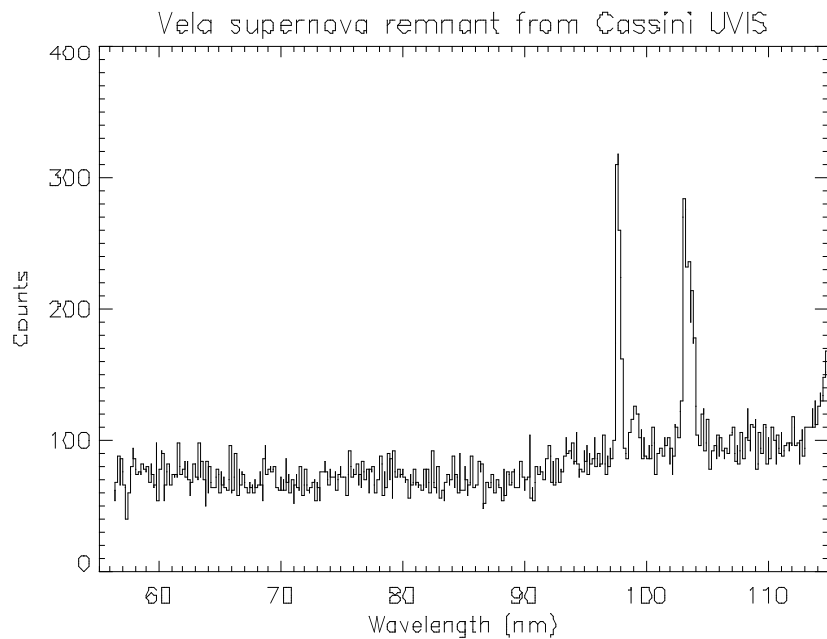
Figure 11.5 Off-Dione observation from 2008 day 181 with Cassini UVIS (EUV channel).

11.11 Conclusion

IPHSurvey data sample large regions of the heliosphere from near Venus to Saturn orbit. They sample a variety of observing geometries from both the upwind and downwind sides of the Sun. Data since 2004 also sample an extended region near Saturn with enhanced hydrogen and oxygen emission. Further study of these data should prove valuable, especially in coordination with similar observations from other spacecraft such as MESSENGER, LRO, SOHO (SWAN), MAVEN, JUNO, and New Horizons. We expect to address questions about the hydrogen and helium densities in the heliosphere, and document changes in the heliosphere due to changes in the Sun. Additional observations have been requested through the Cassini CIMS (Information Management System) software through 2017, the planned end of the mission.

12. Cube Generator
E. Todd Bradley

12.1. Introduction

Cube Generator (CG) is an IDL widget to read and process raw Cassini UVIS data files, and combine the processed data with geometric parameters as calculated by Josh Colwell's Geometer Engine into an *Image Cube* for use in further investigations. Users are given a variety of options regarding the processing of the data and geometer options. This document provides a reference and tutorial for new users to CG. After a brief introduction and comments regarding the installation and compiling of CG, the tutorial is written in the order a typical user would use to create an image cube from raw data.

12.2. Installation

All the necessary files needed to run CG are available on the planetary data system (PDS). Unzip, or save, all the included files to a single directory. Cube Generator will look for the files it needs locally. Many of the files within the CG package are either modified or unmodified versions of code written by other members of the UVIS science team. They have been renamed to avoid confusion or conflict with previously extant code.

12.3. The Interface

Cube Generator requires at least IDL 5.5 and the ICY spice interface, available from ftp://naif.jpl.nasa.gov/pub/naif/toolkit/IDL/.
To run CG, compile and run *cube_generator.pro*, either from the command line or via the IDL development environment. If successful, the following widget will be realized (Figure 12.1).
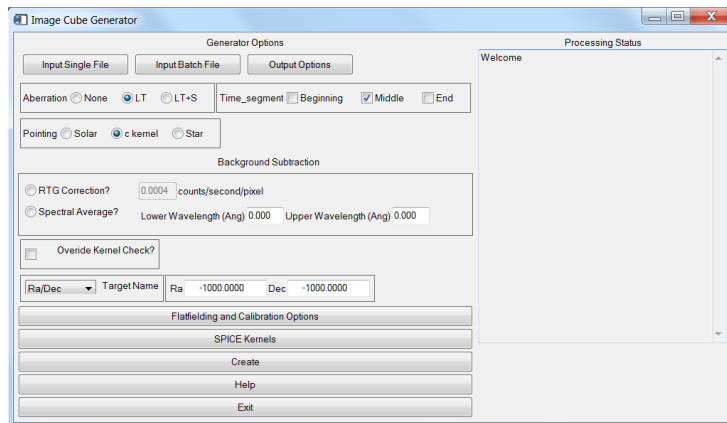

Figure 12.1: Base level menu for Cube Generator.

On the left half of the widget, a series of inputs and menu buttons provide access to the various options that will be discussed in detail in the rest of this document. The text block on the right will update as the widget is used with confirmation and status messages for the user. When the image cube is created, it will also contain a running summary of program steps, status messages, and any errors that may occur.

12.4. Raw Data Input

Raw data files exist on the PDS independent of Cube Generator. A user may input raw data downloaded from the PDS in two ways, either as a single data file from or as a list of files that will be combined to form a single output cube (as in the case of an observation that has been split into multiple raw data files). For any data files obtained from the PDS, the accompanying label file must be downloaded and placed in the same directory as the data file. To create an image cube from a single data file, simply click on the 'Input Single File' button. A file selection dialog will open allowing the user to navigate to where the file is saved on their computer and select it for input.

In the case of an observation that consists of more than one raw file, the user will select the 'Input Batch File' button. The program is asking for a text file that lists the names of all the data files to be combined into a single cube *in the order they are listed in the file*. Cube Generator does not sort files should they be listed out of temporal order, though such an instance would not impact the validity of the associated geometric data.

Currently, the only option for entering a series of data files for batch mode is in the form of a text file.

12.5. Output Formats

Selecting the 'Output Formats' button will change the menu options on the left half of the Cube Generator widget as follows (see Figure 12.2).
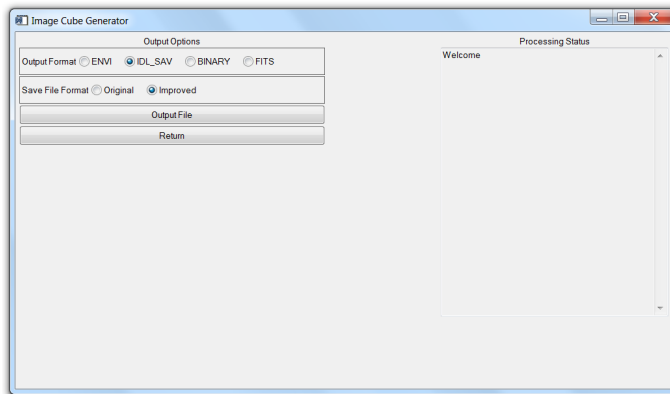

Figure 12.2: File Output options menu

Users have the option of outputting the image cube in four basic formats; 'Envi', 'IDL_SAV', 'Binary', and FITS. The default setting an IDL save file (IDL_SAV) which will save the cube as an IDL structure that can be restored at a later time for further use. If the IDL_SAV output format is selected, there is a further option of the 'Original' or 'Improved' file format. The 'Original' format is included for those users who have already written code that accepts image cubes. The 'Improved' format was designed by Josh Colwell to eliminate the need to reset an IDL session after the creation of each cube due to changing structure dimensions. **It is strongly suggested that users create cubes in the 'Improved' format.** For further details on the structure of both the 'Original' and 'Improved' save file formats, see Appendix 1 at the end of the document.

The 'ENVI' output format creates an image cube and associated header that can be read by the *ENVI* image processing package. *ENVI* is an IDL extension that must be purchased separately from ITT.

Finally, the 'Binary' output format is simply a binary array of double float values. Note that there is no information in the Binary format to inform a user as to the dimensions of the included data.

The 'Output File' button will open a selection dialog that allows the user to select the name and location where the image cube will be written.

When the user has selected the output format and file names, press return to change the menu back to the base screen (Figure 12.1).

12.6. Main Menu Options

Back at the base level menu, the user has a few options that relate to the calculation of the geometric parameters or the processing of the raw data. These options are generally left at their default state, though some special cases may require their modification.

First, the boxed sub-menu labeled 'Aberation'. This option affects how Geometer will calculate the geometric parameters. The default setting of 'LT' commands geometer to calculate the state variables as corrected for light-time. 'None' does not correct for light-time and 'LT+S' corrects for light-time and stellar aberrations. For many observations, the difference between aberration states would likely be negligible. However, given the possible non-negligible effect on some calculations, the 'LT' correction is set as default.

To the right of the aberration box is the time segment box. Users may select any combination of three discrete times within an integration period to retrieve geometry. "Beginning" is at the start of the integration period, "Middle" is at half of an integration period, and "End" is at the end of the integration period. By default the "Middle" button is preselected. For each time period, a separate structure will be returned, denoted by "datastruct2_initial, datastruct2, and datastruct2_final, for the three time periods, with geometry within each for the selected time periods. If a time period is not selected, then that particular structure contains a zero.

Below the aberration selection menu is a box used to select the pointing reference, which may be Solar, c kernel (the default setting), or Star. In the case of Solar or Star the pointing of the instrument is referenced to the vector between the instrument and either the Sun or a star. If "Star" is selected an input box appears requiring that the name of the star be entered.

Below the pointing box is a check-box that allows the user to select between two types of background subtraction, RTG or spectral average. If RTG is selected, the text box will become

active and, if the user chooses, a new RTG noise value may be entered. Cube Generator will subtract from each pixel an RTG noise level based on this value and the integration length of each observation record. **If a new RTG correction value is entered, the user MUST press return for IDL to record the new value.** If "Spectral Average" is selected the user must enter upper and lower spectral bounds, which results in the average of the raw counts over that spectral interval to be subtracted from the raw counts.

Below the "Background Subtraction" box lies another check-box labeled 'Override Kernel Check?'. If selected, this will force CG to continue and make an image cube despite errors from the called SPICE routines that indicate insufficient kernel data to calculate geometric information. Generally, it is in the users interest to allow C-kernel errors to interrupt CG, however there are some cases in which an error may be ignored.

Below the "Override Kernel Check" is a pull down 'Target Name' menu, as shown in Figure 12.3. The user is required to manually select the *Target* relative to which Geometer will calculate the relevant parameters. If no target is selected (or the Ra/Dec target is selected without changing the values to the right), CG will declare an error and interrupt the image cube creation process. If the user wants to calculate parameters relative to a fixed Ra/Dec value, select Ra/Dec as the target and modify the values to the right of the pull down menu (remembering to hit return in each field to register the changes with IDL).
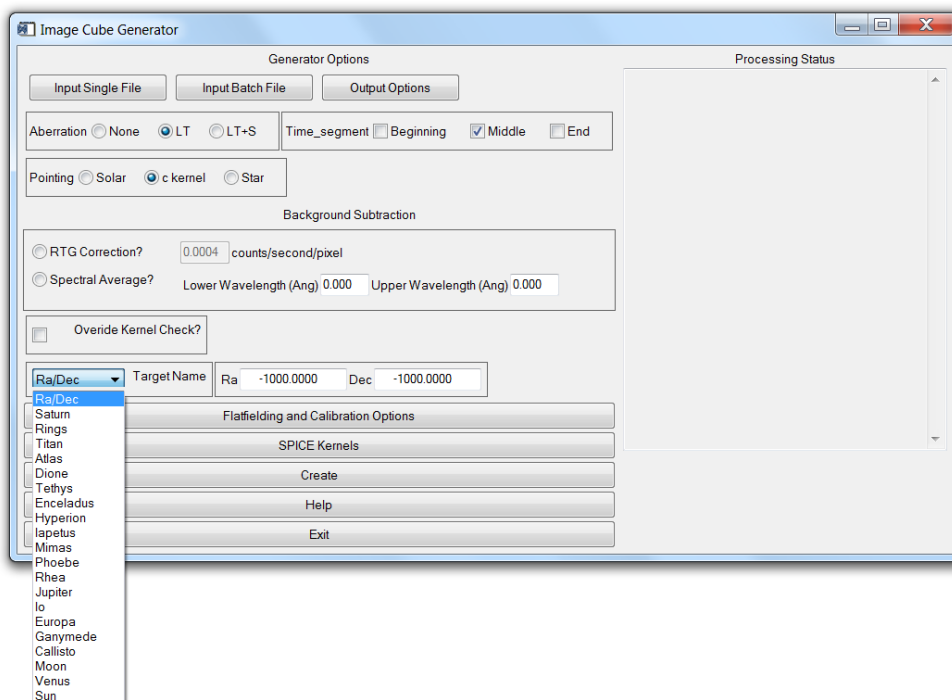
Figure 12.3: Target Name pull-down menu.

Page 111 (7/31/18 - 9:26 AM)

12.7. Flatfielding Options

For general use, this menu (Figure 12.4) will not need to be accessed. The default setting will process the raw data according to the team-sponsored procedure. The default processing scheme corrects the raw data by the following steps.

1. Calibration using calibration factor temporally interpolated to time of observation.
2. Apply Red Patch (for FUV data only).
3. Apply Andrew Steffl (AJS) Not-a-Number (NaN) flatfield with 1.05 multiplicative modifier.
4. Interpolate across NaN pixel gaps.
5. Export corrected data.

Should a user want to eliminate of modify any of the steps above, the *Ala Carte* menu exists to allow flexibility and is accessed by deselecting the 'Full Flatfielding Routine', Figure12. 4.
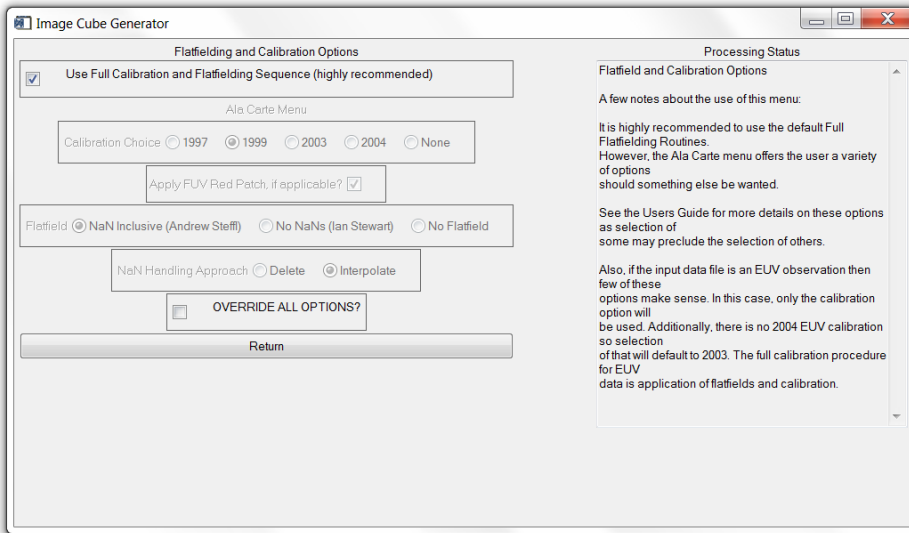
Figure 12.4: Flatfielding Processing Menu

The *Ala Carte* flatfielding menu allows the user to select which ground calibration to apply, 1997, 1999, 2003, or 2004, whether to apply the Red Patch, how to handle NaN's, and

which flatfield to use. The calibration and flatfields both have the multiplicative modifiers applied to them.

Some options within the *Ala Carte* menu preclude other selections. For instance, selection of the "No NaNs (Ian Stewart)" flatfield will override the user's selection of a 'NaN Handling Approach' as those selections no longer have any meaning. Similarly, choosing to apply no calibration will automatically disable the FUV Red Patch, regardless of whether the patch was selected to be applied by the user from the Flatfielding menu.

Each of the choices under the 'Calibration Choice' refer to the year of a lab calibration. If the 1999 lab calibration (the default setting) is selected, and the inputted data set is an FUV observation, the derived correction factor of 0.91 is applied automatically. Selection of any of the other calibrations WILL NOT have a correction factor applied.

If the user checks the box next to the 'Override all Options?' label, NO calibrations or flatfields will be applied to the data. The output in this case would be simply raw data and the geometric information.

12.8. SPICE Kernels

The SPICE Kernel Options menu (Figure 12.5) provides a series of tools to manage the SPICE kernels accessed by Geometer to calculate the geometric parameters included in the image cube. SPICE kernels loaded into memory via the ICY routines stay resident in memory until IDL is shut down. Resetting the IDL session **DOES NOT** clear SPICE kernels from memory. Thus, when processing a large number of files, it is possible to have many, and possibly conflicting, kernels loaded.

The first option in this menu will list all the SPICE kernels currently in memory in the right hand text box. This is useful for when CG aborts due to a C-kernel error. Examining the loaded kernels may identify the missing kernel.

To load a single kernel into memory, user the 'Load a Kernel' button. A file selection dialog will open and, if successful, the Processing Status box will confirm loading of the kernel. The user may also load a series of kernels simultaneously via the 'Load Kernel Batch' button. Similar to the batch loading function for raw data files, this batch load asks for a text file that contains the paths and names of the desired kernels. And, as with the single kernel file loading option, a successful operation will be indicated in the status box. Alternatively the user may choose to load spice kernels independently of Cube Generator as long as the kernels are loaded into the numerical processing software (e.g., IDL) before running Cube Generator.

Finally, the 'Unload All Kernels' button will force IDL to clear all SPICE kernels from memory. If you are concerned that the wrong kernel might be used to calculate the geometry, use this to clear memory and then re-load the specific kernels you want to use.
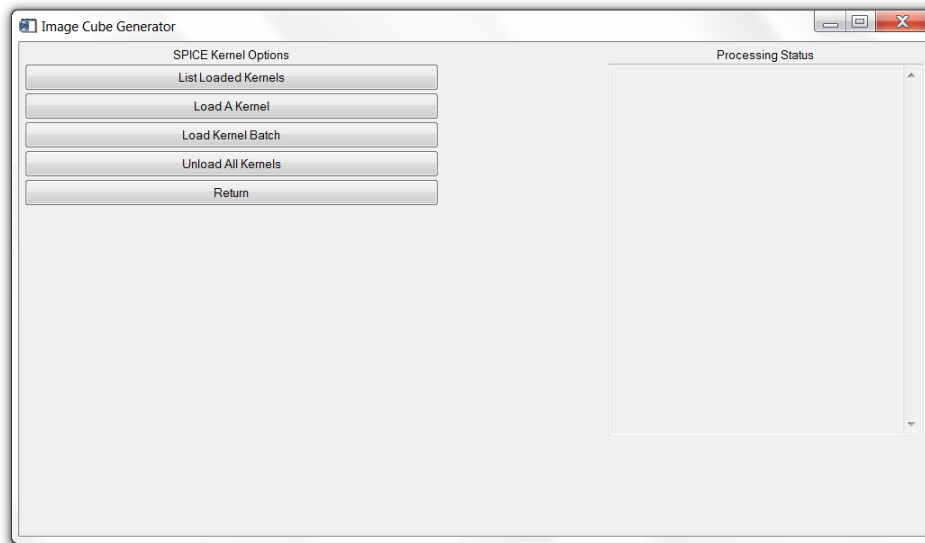
Figure 12.5: SPICE Kernel Options menu.

A quick note about the loading of SPICE kernels. The ICY interface **requires** that the first kernel in memory be the leap second correction kernel (LSK). Thus, when loading, make sure that is either the first loaded or the first entry in the text batch file. In addition, the latest loaded SPICE kernels take precedence. Thus, if two kernels are loaded that cover overlapping times, the latter will be used to calculate state variables. The user should use the 'List Loaded Kernel' and 'Unload All Kernels' functions to ensure kernels are loaded in the right order for the appropriate data file.

12.9. Cube Creation

Finally, once all the variables and options have been set as above, pressing the 'Create' button creates the image cube. As the code runs, the 'Processing Status' box will update. If there are any errors during processing, an appropriate message will be displayed and instruct the user in how to correct the problem. On success, the output file location and dimensions will be displayed.

12.10. Final Menu Options

At the base level menu, there are two final buttons that haven't been described. Both are so self-explanatory that they shouldn't require any mention, but to be insanely complete, a few words.

'Help' opens an abridged version of this document within the widget framework for quick reference as needed.

'Exit' exits.

12.11. Examples of Restoring the Contents of Variables

Suppose that one needs to look at the calibrated data, denoted by the variable name "UVIS" and compare this to the pixel center longitude determined at the middle of the integration period. In IDL the code would be written as follows:

```
Restore,filename
UVIS = datastruct2.UVIS
Pixel_center_longitude = datastruct2.pixel_center_longitude
```

Alternatively suppose one needs to look at the raw counts and compare this to the pixel center phase angle for geometry determined at the beginning of the integration period. In IDL the code would be as follows:

```
Restore,filename
Rawcounts = datastruct2_initial.rawcounts
Pixel_center_phase_angle =
datastruct2_initial.pixel_center_phase_angle
```

By default, the number of spatial pixels is 64 and the number of spectral pixels is 1024. However observations do not always make use of all of the spatial or spectral pixels depending on data volume restrictions. Therefore although the size of the UVIS or raw counts array are 64 X 1024 X number of data records, only pixels that were used in data acquisition will contain non-zero values. This may be determined by the variables XMIN, XMAX, YMIN, and YMAX. Furthermore pixels may be binned on board the spacecraft before and will also affect the number of non-zero pixels. This may be determined by the variables XBIN and YBIN. Some variables are independent of the pixels on the detector, e.g. "SPACECRAFT_LONGITUDE". Thus the size of this array will be 1 X the number of data records.

References

Ajello, J.M., Stewart, A.I., Thomas, G.E., and Graps, A. 1987. A. Solar Cycle Study of Interplanetary Lyman-alpha variations: Pioneer Venus Orbiter Sky Background Results, *Astrophys. J.* 317, 964-986.

Ajello, J.M., et al., 1994. Observations of interplanetary Lyman-alpha with the Galileo Ultraviolet Spectrometer: multiple scattering effects at solar maximum, Astron. *Astrophys*. 289, 283-303.

Ajello, J.M., Pryor, W.R., Esposito, L.W., Stewart, A.I.F., McClintock, W.E., Gustin, J., Grodent, D., Gérard, J.-C., Clarke, J.T. 2005. The Cassini Campaign observations of the Jupiter Aurora by the Ultraviolet Imaging Spectrograph and the Space Telescope Imaging Spectrograph. *Icarus*. 78, 327–345.

Ajello, J.M., West, R.A., Gustin, J., Larsen, K., Stewart, A.I.F., Esposito, L.W., McClintock, W.E., Holsclaw, G.M., Bradley, E.T. 2012. Cassini UVIS Observations of Titan Nightglow Spectra. *J. Geophys. Res. 117*, A12315, doi:10.1029/2012JA017888.

Baker, D.J., Romick, G.J. 1976. The rayleigh: interpretation of the unit in terms of column emission rate or apparent radiance expressed in SI units. *Appl. Opt. 15*, 1966–1968.

Bradley, E.T., Colwell, J.E., Esposito, L.W., Cuzzi, J.N., Tollerud, H., Chambers, L. 2010. Far Ultraviolet Spectral Properties of Saturn's Rings from Cassini UVIS. *Icarus*. 206, Issue 2, 458-466.

Chambers, L.S., Cuzzi, J. N., Asphaug, E., Colwell, J. E., Sugita, S. 2008. Hydrodynamical and Radiative Transfer Modeling of Meteoroid Impacts into Saturn's Rings. *Icarus*. 194, 623-635, doi:10.1016/j.icarus.2007.11.017.

Clarke, J.T., Gérard, J.-C., Grodent, D., Wannawichian, S., Gustin, J., Connerney, J., Crary, F., Dougherty, M., Kurth, W., Cowley, S.W.H., Bunce, E.J., Hill, T., Kim, J. 2005. Morphological differences between Saturn's ultraviolet aurorae and those of Earth and Saturn. *Nature*. 433, 717–719.

Code, A.D., Houk, T. E., McNall, J. F., Bless, R. C., Lillie, C. F., Ultraviolet photometry from the orbiting astronomical observatory. I. Instrumentation and operation 1970, *Ap. J.* , *161*, 377.

Code, A.D., and Meade, M.R., Ultraviolet photometry from the orbiting astronomical observatory. XXXII. An atlas of ultraviolet stellar spectra 1979, *Ap. J. Supp.*, *39*, 195.

Colombo, G., Goldreich, P., and Harris, A.W., 1976. Spiral structure as an explanation for the asymmetric brightness of Saturn's A ring. Nature 264, 344-345.

Colwell, J.E., Esposito, L. W., Sremcevic, M. 2006. Gravitational wakes in Saturn's A ring measured by stellar occultations from Cassini. *Geophys. Res. Lett*. 33, L07201, doi:10.1029/2005GL025163.

Colwell, J.E., Esposito, L. W., Sremcevic, M., Stewart, G. R., McClintock, W. E. 2007. Self-gravity wakes and radial structure of Saturn's B ring. *Icarus*. 190, 127-144, doi:10.1016/j.icarus.2007.03.018.

Colwell, J.E., Nicholson, P. D., Tiscareno, M. S., Murray, C. D., French, R. G., Marouf, E. A. 2009. The Structure of Saturn's Rings. In *Saturn from Cassini-Huygens* (Dougherty, M. K., Esposito, L. W., Krimigis, S. M., Eds.), Springer, 375-412.

Colwell, J. E., Esposito, L.W., Pettis, D., Sremčević, M., Jerousek, R.G., Bradley, E.T. 2010. Cassini UVIS Stellar Occultation Observations of Saturn's Rings. *Astron. J.* **140**, 1569-1578, doi:10.1088/0004-6256/140/6/1569.

Dols, V., Gérard, J.-C., Clarke, J.T., Gustin, J., Grodent, D. 2000. Diagnostics of the jovian aurora deduced from ultraviolet spectroscopy: Model and HST/GHRS observation. *Icarus*. 147, 251–266.

Esposito, L. W., Colwell, J.E., and McClintock, W.E. 1998. Cassini UVIS Observations of Saturn's Rings. *Planet. Space Sci.* **46**, 1221-1235.

Esposito, L.W., Barth, C. A., Colwell, J. E., Lawrence, G. M., McClintock, W. E., Stewart, A. I. F., Keller, H. U., , Korth, A., Lauche, H., Festou, M., Lane, A. L., Hansen, C. J., Maki, J. N., West, R. A., Jahn, H., Reulke, R., Warlich, K., Shemansky, D. E., and Yung, Y. L. 2004. The Cassini Ultraviolet Imaging Spectrograph Investigation. *Space Sci. Rev*. 115, 299-361.

Esposito, L.W., Meinke, B. K., Colwell, J. E., Nicholson, P. D., Hedman, M. M. 2008. Moonlets and clumps in Saturn's F ring. *Icarus*. 194, 278-289.

Flasar, F. M., et al. 2005. Temperatures winds and composition in the Saturnian system. *Science*. 1247—1251. Sci., doi: 10.1126/science.1105806.

French, R.G., Nicholson, P. D., Cooke, M. L., Elliot, J. L., Matthews, K., Perkovic, O., Tollestrup, E., Harvey, P., Chanover, N. J., Clark, M. A., Dunham, E. W., Forrest, W., Harrington, J., Pipher, J., Brahic, A., Grenier, I., Roques, F., Arndt, M. 1993. Geometry of the Saturn system from the 3 July 1989 occultation of 28 Sgr and Voyager observations. *Icarus*. 103, 163-214.

Gangopadhyay, P., Izmodenov, V. V., Gruntman, M., & Judge, D. L. 2006. Voyager 1, Voyager 2, and Pioneer 10 Lyman alpha data and their interpretation. *Astrophys. J*. 637, 786-790.

Grodent, D., Waite Jr., J.H., Gérard, J.C. 2001. A self-consistent model of the jovian auroral thermal structure. *J. Geophys. Res*. 106. 12933–12952.

Grodent, D., Clarke, J.T., Waite Jr., J.H., Cowley, S.W.H., Gerard, J.C., Kim, J. 2003. Jupiter's polar auroral emissions, *J. Geophys. Res*., 108(A10), 1366, doi:10.1029/2003JA010017.

Guerlet ,S., Fouchet, T., Bezarda, B., Simon-Miller, A.A., Flasar, F. M. 2008. Ethane, ascetylene and propane distribution in Saturn's stratosphere from Cassini/CIRS limb observations, *Societe Francaise d'Astronomie et d'Astrophysique (SF2A)*.

Guerlet ,S., Fouchet, T., Bezarda, B., Simon-Miller, A.A., Flasar, F. M. 2009. Vertical and meridional distribution of ethane, acetylene and propane in Saturn's stratosphere from CIRS/Cassini limb observations. *Icarus*, 214–232, doi: 10.1016/j.icarus.2009.04.002.

Gustin, J., Feldman, P.D., Gerard, J.-C., Grodent, D., Vidal-Madjar, A., Ben Jaffel, L., Desert, J.-M., Moos, H.W., Sahnow, D.J., Weaver, H.A., Wolven, B.C., Ajello, J.M., Waite, J.H., Roueff, E., Abgrall, H. 2004. Jovian auroral spectroscopy with FUSE: Analysis of self-absorption and implications for electron precipitation. *Icarus,* 171, 336‑355.

Gustin, J., Gérard, J.-C., Grodent, D., Cowley, S.W.H., Clarke, J.T., Grard, A. 2004. Energy–flux relationship in the FUV jovian aurora deduced from HST-STIS spectral observations. *J. Geophys. Res*. 109, doi:10.1029/2033JA010365.

Gustin, J., Gérard, J.-C., Pryor, W., Feldman, P.D., Grodent, D., Holsclaw, G. 2009. Characteristics of Saturn's polar atmosphere and auroral electrons derived from HST/STIS, FUSE and Cassini/UVIS spectra. *Icarus*. 200, 176–187. doi:10.1016/j.icarus.2008.11.013.

Hansen, C.J., et al. 2006. Cassini Ultra-Voilet Imaging Spectrograph (UVIS) investigation of Enceladus' water vapor plume. *Science*. 311, 1422.

Hansen, C.J., Esposito, Stewart, A.I.F., L.W., Meinke, B., Wallis, B., Colwell, J.E., Hendrix, A. R., Larsen, K., Pryor, W., Tian, F. 2008. Water Vapor Jets inside the Plume of Gas Leaving Enceladus. *Nature* **456**, 477-479, doi:10.1038/nature07542.

Hall, D.T. 1992. In *Ultraviolet Resonance Scattering and the Structure of the Heliosphere*, Ph. D. Thesis, Physics Dept., University of Arizona, Tucson.

Hallett, J.T., Shemansky, D. E., and Liu, X. 2005a, A Rotational-Level Hydrogen Physical Chemistry Model for General Astrophysical Application, *Astrophys. J.*, *624*, 448--461.

Hallett, J.T., Shemansky, D. E., and Liu, X. 2005b, Fine-structure physical chemistry modeling of Uranus H_2 X quadrupole emission, *Geophys. Res. Lett.*, *32*, L02204, doi:10.1029/2004GL021327.

Heath, D.F. and Sacher, P. A. 1966. Effects of a simulated high-energy space environment on the ultraviolet transmittance of optical materials between 1050Å and 3000 Å. *Applied optics*. 5, 937–943.

Hedelt, P., Ito, Y., Keller, H. U., Reulke, R., Wurz, P., Lammer, H., Rauer, H., and Esposito, L. W. 2010. Titan's atomic hydrogen corona. *Icarus*. 210, 424–435.

Herbison-Evans, D., Hanbury Brown, R., Davis, F., Allen, L. R. 1971. A study of α Virginis with an intensity interferometer. *Mon. Not. Roy. Astr. Soc.*, *151*, 161.

Howett, C.J.A., Irwin, P.G.J., Teanby, N.A., Simon-Miller, A., Calcutt, S.B., Fletcher, L.N., deKok, R. 2007, Meridional variations in stratospheric acetylene and ethane in the southern hemisphere of the Saturnian atmosphere as determined from Cassini/CIRS measurements. *Icarus*, *190*, 556 – 572.

Liang, M-C., Yung, Y.L., Shemansky, D. E. 2007. Photolytically generated aerosols in the mesosphere and thermosphere of Titan, *Astrophys. J.*, *661*, L199-L202.

Maki, J.N. 1993. *The Hydrogen Deuterium Absorption Cell in the Cassini Spacecraft: A Remote Sensing Instrument for Atomic D/H Measurements on Saturn and Titan.* PhD thesis, University of Colorado.

McClintock, W.E., Rottman, G.J., Woods, T.N. 2000. Solar Stellar Irradiance Comparison Experiment II (SOLSTICE II) for the NASA Earth Observing System's Solar Radiation and Climate Experiment (SORCE) mission. *Proc. SPIE Earth Observ. Syst*. V 4135, 225–234.

McClintock, W.E., Lawrence, G.M, Kohnert R.A., Esposito, L.W. 1993. Optical design of the Ultraviolet Imaging Spectrograph for the Cassini mission to Saturn. *Optical Engineering,* 32, 3038.

McClintock, W. 2002. Cassini UVIS Calibration Report. *LASP Draft*, 03-15-2002.

Meade, M.R. and Code, A.D. 1980. Ultraviolet photometry from the orbiting astronomical observatory. XXXVIII. A second atlas of ultraviolet stellar spectra. *Ap. J. Supp.*, *42*, 283.

Melin, H., Shemansky, D.E., Liu, X. 2009. The distribution of atomic hydrogen and oxygen in the magnetosphere of Saturn. *Planetary and Space Sci*. 57, 1743-1753.

Moses, J.I., Fouchet, T., Bezard, B., Gladstone, G.R., Lellouch, E., Feuchtgruber, H. 2005, Photochemistry and diffusion in Jupiter's stratosphere: Constraints from ISO observations and comparisons with other giant planets. *J. Gephys. Res.*, 110, E08001, doi: 10.1029/2005JE002411.

Moses, J.I. and Greathouse, T.K. 2005. Latitudinal and seasonal models of stratospheric photochemistry on Saturn: Comparison with infrared data from IRTF/TEXES, *J. Gephys. Res.*, 110, E09007, doi:10.1029/2005JE002450.

Nicholson, P. D., Cooke, M. L., Pelton, E. 1990. An absolute radius scale for Saturn's rings. *Astron. J.* 100, 1339-1362.

Pankratz, C.K., Knapp, B. G., Reukauf, R. A., Fontenla, J., Dorey, M. A., Connelly, L. M., Windnagel, A. K. 2005. The SORCE Science Data System. *Solar Physics*, 230:389–413. doi: 10.1007/s11207-005-5008-4.

Porco, C.C., Weiss, J.W., Richard, D.C., Dones, L., Quinn, T., Throop, H. 2008. Simulations of the dynamical and light-scattering behavior of Saturn's rings and the derivation of ring particle and disk properties. *Astron. J.* **136**, 2172-2200.

Pryor, W.R., et al. 1992. The Galileo and Pioneer Venus Ultraviolet Spectrometer Experiments: Solar Lyman-alpha latitude variation at solar maximum from interplanetary Lyman-alpha observations, *Astrophys. J.* 394, 363-377.

Pryor, W.R., Ajello, J.M., McComas, D.J., Witte, M., Tobiska, W.K. 2003. Hydrogen atom lifetimes in the three-dimensional heliosphere over the solar cycle, *J. Geophys. Res.*, 108(A10), 8034, doi:10.1029/2003JA009878.

Pryor, W.R., et al. 2008. Radiation transport of heliospheric Lyman-alpha from combined Cassini and Voyager data sets, *A&A.* 491, 21-28.

Quemerais, E., Sandel, B.R. and de Toma, G. 1996. 26-day modulation of the sky background LY alpha brightness: Estimating the interplanetary hydrogen density, *Astrophys. J.*, 463, 349.

Regehly, M. 2003. *Characterization and Verification of the Hydrogen Deuterium Absorption Cell*. Master's thesis, Humboldt University, Berlin,

Rogerson, J.B., Spitzer, L., Drake, J.F., Dressler, K., Jenkins, E.B., Morton, D.C., York, D.G. 1973. Spectrophotometric results from the Copernicus satellite. I. Instrumentation and performance. *Ap. J.*, *181*, L97.

Shemansky, D.E., Judge, D. L., Jessen, J. M. 1984. Pioneer 10 and Voyager observations of the interstellar medium in scattered emission of the He 584 and H Lya 1216 Å Lines. In *IAU Coll. Number 81, The Local Interstellar Medium, NASA CP 2345*.

Shemansky, D.E., Stewart, A.I.F., West, R.A., Esposito, L.W., Hallett, J.T., Liu, X.M. 2005. The Cassini UVIS Stellar Probe of the Titan Atmosphere, *Science*, *308*, 978.

Shemansky, D.E. and Liu, X. 2012a. Saturn upper atmospheric structure from Cassini EUV/FUV occultations. *Can. J. Phys.*, Hunten special issue (Accepted 2012).

Shemansky, D.E. and Liu, X. 2012b, H2O in the Saturn atmosphere and ionosphere, *Astrophys. J.*, (unpublished manuscript).

Smith, G.R., Shemansky, D.E., Holberg, J.B., Broadfoot, A.L., Sandal, B.R., McConnell, J. C. 1983. Saturns upper atmosphere from the Voyager 2 solar and stellar occultations, *J. Geophys. Res.*, *88*, 8667 – 8678

Wu, C. Y. R., F. Z. Chen, D. L. Judge 2001, Measurement of temperature-dependent absorption cross sections of C_2H_2 in the VUV-UV region, *J. Geophys. Res* , *106*, 7629-7636.

Steffl, A. J. 2005. *The Io Plasma Torus During the Cassini Encounter with Jupiter: Temporal, Radial and Azimuthal Variations*. PhD thesis, University of Colorado.

Thomas, G. E. 1978. The interstellar wind and its influence on the interplanetary environment, *Ann. Rev. Earth. Planet.* Sci. 6, 173-204.

Warlich, K. 1997. *Simulation and Optimization of the Hydrogen-Deuterium-Absorption-Cell Experiment on Cassini.* PhD thesis, Technical University Berlin

Westlake, J.H., Bell, J.M., Waite Jr., J.H., Johnson, R.E., Luhmann, J.G., ƒMandt, K.E., Magee,, B.A., Rymer, A.M. 2011. Titan's thermospheric response to various plasma environments. *J. Geophys. Res*. 116, A03318, doi:10.1029/2010JA016251.

Wu, C.Y.R., Chen, F.Z., Judge, D.L. 2001. Measurement of temperature-dependent absorption cross sections of C2H2 in the VUV-UV region*, J. Geophys. Res* , 106, 7629.

Appendix 1: Image Cube Format and Descriptions for Cube Generator

The Cube format structures are named "Datastruct2_initial, "Datastruct2" and "Datastruct2_final" for the three possible time periods as previously discussed. Each structure contains the following named fields, where for all undefined values, the variable is set to -1000. Also, spacecraft is abbreviated as s/c.

Variable	Description
UVIS:	calibrated data
PIXEL_CENTER_RA:	ra of the center of each pixel
PIXEL_LOWER_LEFT_RA:	ra of the lower left corner of each pixel
PIXEL_UPPER_LEFT_RA:	ra of the upper left corner of each pixel
PIXEL_UPPER_RIGHT_RA:	ra of the upper right corner of each pixel
PIXEL_LOWER_RIGHT_RA:	ra of the lower right corner of each pixel
PIXEL_CENTER_DECLINATION:	declination of the center of each pixel
PIXEL_LOWER_LEFT_DECLINATION:	declination of the lower left corner of each pixel
PIXEL_UPPER_LEFT_DECLINATION:	declination of the lower left corner of each pixel
PIXEL_UPPER_RIGHT_DECLINATION:	declination of the lower left corner of each pixel f
PIXEL_LOWER_RIGHT_DECLINATION:	declination of the lower left corner of each pixel
PIXEL_CENTER_LATITUDE:	latitude on target body of center of each pixel
PIXEL_LOWER_LEFT_LATITUDE	latitude on target body of lower left corner of each pixel
PIXEL_UPPER_LEFT_LATITUDE	latitude on target body of upper left corner of each pixel
PIXEL_UPPER_RIGHT_LATITUDE	latitude on target body of upper right corner of each pixel
PIXEL_LOWER_RIGHT_LATITUDE	latitude on target body of lower right corner of each pixel
PIXEL_CENTER_LONGITUDE	longitude on target body of center of each pixel
PIXEL_LOWER_LEFT_LONGITUDE	longitude on target body of lower left corner of each pixel
PIXEL_UPPER_LEFT_LONGITUDE	longitude on target body of upper left corner of each pixel
PIXEL_UPPER_RIGHT_LONGITUDE	longitude on target body of upper right corner of each pixel
PIXEL_LOWER_RIGHT_LONGITUDE	longitude on target body of lower right corner of each pixel
PIXEL_CENTER_INCIDENCE_ANGLE	angle between Sun and local surface normal of target body at location of pixel center
PIXEL_CENTER_EMISSION_ANGLE	angle between line of sight and local surface normal of target body at location of pixel center
PIXEL_CENTER_PHASE_ANGLE	Sun-line of sight angle
PIXEL_CENTER_RAYHEIGHT	minimum separation between the look vector and the surface in km
PIXEL_CENTER_OCCULTATION_LATITUDE	sub tangent latitude if field of view is off limb of a moon
PIXEL_CENTER_OCCULTATION_LONGITUDE	sub tangent longitude if field of view is off limb of a moon
PIXEL_CENTER_LINE_OF_SIGHT_DISTANCE	distance from s/c to target body
SUB_SPACECRAFT_LONGITUDE	sub-spacecraft longitude in the Saturn fixed frame
SUB_SPACECRAFT_LATITUDE	sub-spacecraft latitude in the Saturn fixed frame
SUB_SOLAR_LONGITUDE	sub-solar longitude in the Saturn fixed frame
SUB_SOLAR_LATITUDE	sub-solar latitude in the Saturn fixed frame
SPACECRAFT_ALTITUDE	distance between s/c and center of target body
TARGET_RA	right ascension of target body relative to s/c
TARGET_DECLINATION	declination of target body relative to s/c
TARGET_PHASE_ANGLE	phase angle at the sub-S/C point
TARGET_INCIDENCE_ANGLE	solar incidence angle at the sub-S/C point
TARGET_EMISSION_ANGLE	emission angle at the sub-S/C point
SPACECRAFT_LOCATION_X	x location of s/c with respect to planet
SPACECRAFT_LOCATION_Y	y location of s/c with respect to planet
SPACECRAFT_LOCATION_Z	z location of s/c with respect to planet

SPACECRAFT_VELOCITY_X	x velocity of s/c with respect to planet
SPACECRAFT_VELOCITY_Y	y velocity of s/c with respect to planet
SPACECRAFT_VELOCITY_Z	z velocity of s/c with respect to planet
ET	elapsed mission time
CENTER_RING_PLANE_RADII	distance from Saturn center to a pixel projected in the ring plane
LOWER_LEFT_RING_PLANE_RADII	distance from Saturn center to lower left corner of each pixel
UPPER_LEFT_RING_PLANE_RADII	distance from Saturn center to upper left corner of each pixel
UPPER_RIGHT_RING_PLANE_RADII	distance from Saturn center to upper right corner of each pixel
LOWER_RIGHT_RING_PLANE_RADII	distance from Saturn center to lower right corner of each pixel
UTC	date and time of observation in coordinated universal time.
KERNELS	list of all SPICE kernels loaded in IDL memory during cube creation
XBIN	spectral binning of data
YBIN	spatial binning of data
XMIN	lower row of spectral pixels
XMAX	upper row of spectral pixels
YMIN	lower column of spatial pixels
YMAX	upper column of spatial pixels
SOLAR_HOUR_ANGLE	angle of the field of view intercept with respect to the sub solar point. 0° is at midnight and increased CCW when looking down on the north pole.
RAM_LATITUDE	latitude of leading edge point of target body
RAM_LONGITUDE	longitude of leading edge point of target body
PHI	azimuth angle
PIXEL_CENTER_SOLAR_HOUR_ANGLE	solar hour angle of center of pixel on target body
PIXEL_LOWER_LEFT_SOLAR_HOUR_ANGLE	solar hour angle of lower left corner of pixel on target body
PIXEL_UPPER_LEFT_SOLAR_HOUR_ANGLE	solar hour angle of upper left corner of pixel on target body
PIXEL_UPPER_RIGHT_SOLAR_HOUR_ANGLE	solar hour angle of upper right corner of pixel on target body
PIXEL_LOWER_RIGHT_SOLAR_HOUR_ANGLE	solar hour angle of lower right corner of pixel on target body
RAWCOUNTS	un-calibrated data

Also included in each data cube are variables called "calibration_matrix" and "calibration_error_matrix," which provides the N X M matrices of the calibration factor that was applied to the data and the error in that calibration factor. N and M are the number of spectral and spatial elements in the data, respectively. Also in the data cube is a variable called "note" that provides information such as the type of background that was applied to the data, the type of flat-fielding used, etc.

Appendix 2 Definitions and technique terms

Aberration-corrected toroidal grating -A kind of diffraction grating (see Diffraction Grating)

Absorption cell - A cell that is filled with a particular gas that absorbs light of particular wavelengths.

Angstrom - A unit of measurement, equaling 10 -10 meter or 10 -8 centimeters, usually used to express short wavelengths.

Aperture -An adjustable opening in an instrument (like a camera) that controls the amount of light that can enter.

Attitude control - The act of controlling the position of a spacecraft relative to the direction in which it's moving.

Baffle - A device that regulates the flow of light so that it all comes from a particular direction.

Channel - A specific frequency band for transmitting or receiving signals, (i.e. different signal frequencies give you different television channels). For UVIS, a part of the instrument sensitive to a particular frequency band.

Channel electron multiplier (CEM) - A light-sensitive device that amplifies dim signals.

CODACON (Coded Anode Converter) - A devise, at the output of the detector, that converts the data from the spectrometer into an image format.

Command and Data Subsystem (CDS) - Cassini's main computer that commands and collects data from the various instruments and packages it to be sent back to NASA?

Concave grating spectrometer - A spectrometer whose diffraction grating has a concave shape.

Detector - A light-sensitive device that produces electrical signals when illuminated.

Diffraction Grating - A grooved optical element that has been deformed to reflect light of many colors. It acts like a prism to produce a spectrum.

Electromagnetic Spectrum - See "Spectra". Also see graphic of spectrum.

Filament current controllers - Controls the amount of current sent to the HDAC filaments, and thus, their temperature.

Focal plane - The location where the rays from a distant object merge: This is where we place the detector.

Grating ruling density - The number of grooves per mm on the diffraction grating.

GSE (UVIS Ground Support Equipment) - Equipment used for testing and operating UVIS before launch.

Imaging microchannel plate detector - A light detector formed from glass full of many small channels that creates an image of the light shining on it.

Imaging, pulse-counting detector -   Each bit of light that falls on the detector creates a pulse of electricity. See "imaging microchannel plate detector".

Imaging spectroscopy -   *Imaging* spectroscopy is what UVIS does--it takes spectrographic measurements and turns them into a graph, but it can also turn the points on the graph into digital data that can then be made into pictures (images). Because humans can't see UV wavelengths of light, we assign different "false colors" to the different wavelengths that allows us to produce a picture out of the data that our eyes can appreciate.

Ion pump - A small vacuum pump that works by ionizing air molecules.

JPL - NASA's Jet Propulsion Laboratory in Pasadena.

LASP - Laboratory for Atmospheric Research in Boulder, Colorado - A research facility of the University of Colorado and the builders of the UVIS instrument.

Logic - Computer circuitry

Lyman-alpha emission - Light emitted by hydrogen atoms at a wavelength of 1216Å.

Magnetosphere - A magnetic environment surrounding an object, like a planet, in a fashion similar to an atmosphere.

MDT - Mountain Daylight Time -- The time in Boulder, Colorado, where LASP is. (Except in winter when it's MST -- Mountain Standard Time).

MgF$_2$ windows - Windows made from crystals of magnesium fluoride.

Microchannel plate detector - (see above under "Imaging...")

Nanometer - A unit of measurement that is one billionth (10 -9) of a meter.

NASA - National Aeronautics and Space Administration, headquartered in Washington, DC with field centers across the country.

Neutrals - Particles, objects or systems that have no electrical charge.

Objective lens - A lens that focuses light on the detector.

Optical coatings - Coatings specifically made for the lenses of light-sensitive devices.

Orbiter - A spacecraft whose purpose is to orbit around an object like a planet or a satellite (moon).

Payload - The instruments, crew or equipment carried by a spacecraft.

Photochemistry - The chemistry of the effects of light on chemical systems.

Photometer - An instrument for measuring the intensity of light.

Photomultiplier tube detector - A vacuum tube that amplifies and detects weak light signals.

Photons - Packets of radiant energy: quanta of light.

Pulse- amplifier-discriminator - The part of UVIS that counts responses (pulses) to light falling on the detector. It discriminates between light and background noise.

Reflecting telescope - A telescope where mirrors are the optical elements, not lenses.

Remote sensing - Gathering information from far away; like the UVIS instrument will gather data on ultraviolet light in the saturnian system and send it back to Earth.

Remote Sensing Palette (on Orbiter) - The area on Cassini to which experiments (like the UVIS instrument) are secured into place.

Resonance absorption cells - Cells filled with gas that absorbs at its atoms' resonant frequencies (same as "absorption cell")

Satellite - A body that revolves around another body like a Saturn's moon Titan revolving around Saturn; or a man-made object revolving around a body, like Explorer 1 orbiting Earth. We call the moons of planets satellites instead of moons so as not to confuse them with the Earth's Moon.

Signal-to-noise-ratio (SNR) - A ratio to measures the clarity of a data source or transmission, usually a ratio of the signal amplitude and the noise amplitude. The higher the SNR, the less the interference with reception.

Slew - To turn something on an axis or to turn sharply or veer. Cassini slews to point its cameras at targets of interest.

Slit changer (entrance slit) - There are three slits each on UVIS EUV and FUV telescopes and that allow light into the instrument to be measured. The slit changer switches between them to measure with different spectral resolutions.

Solar blind CsI photocathode - The active element that is insensitive to reflected sunlight only seeing light with shorter wavelength.

Solar flux - The amount of light from the Sun.

Solar or stellar occultation - Watching the Sun (or a star) pass behind an object of interest, like a planet or Saturn's rings. Observing solar occultations help us discover things like the vertical structure of clouds, gases in atmospheres and active processes that move the particles in Saturn's rings.

SOPC (UVIS Science Operations and Planning Computer) - The computer we use to plan observations and send them to JPL.

Spectra, Spectrum - Spectra is the plural of spectrum, which is a series of energies (like light) arranged according to wavelength, or frequency. The electromagnetic spectrum is an array of radiation that is divided into a number of sub-portions, where the boundaries are only vaguely defined. They extend from the shortest cosmic rays, through gamma rays, X-rays, ultraviolet light, visible light, infrared radiation, microwave and all other wavelengths of radio energy.

Spectral resolution - The ability to distinguish two spectral features close to one another; the smallest difference in wavelength between two such distinguished features.

Spectrograph - A spectroscope that measures wavelengths of light (spectra) and then displays the data as a graph. UVIS is an *imaging* spectrograph, which means it can also display the points of the graph as a picture (see Imaging Sepctrosopy).

Spectroscope - A machine (instrument) for producing and observing spectra.

Spectroscopic measurements - The measurements taken by a spectrograph.

Spectrometer - A spectroscope equipped with the ability to measure wavelengths.

Telemetry Data Server (TDS) - Telemetry data are the spacecraft observations. They are stored temporarily on the TDS.

Ultraviolet (UV)- a portion of the complete electromagnetic spectrum Ultraviolet is a portion of the spectrum that is a shorter wavelength than visible light; roughly, with a wavelength interval from 100 to 4000 angstroms. Ultraviolet radiation from the Sun is responsible for many complex photochemical reactions like the formation of the ozone layer. Extreme ultraviolet (EUV) and far ultraviolet (FUV) wavelengths are different portions of the ultraviolet portion of the spectrum. For Cassini UVIS, EUV is between 55.8-118 nanometers and FUV is between 110-190 nanometers.

Undispersed (zero-order) light - A specular reflection off the diffraction grating which acts like a mirror.

Uplink Product Generation System (UPGS) - A process consisting of manpower, software and hardware that generates the sequencing of the UVIS instrument according to the plan of the science team.

UTC - Coordinated Universal Time, also known as Greenwich Mean Time (GMT), Greenwich Mean Time is based upon the time at the zero degree meridian that crossed through Greenwich, England and is used as a world time and date standard.

Weight-relieved (aluminum cases) - UVIS is built out of aluminum that has been carved out to the dimensions necessary in order to be as light as possible.